

國立臺灣大學電機資訊學院電信工程學研究所



碩士論文

Graduate Institute of Communication Engineering
College of Electrical Engineering and Computer Science

National Taiwan University

Master Thesis

單一影像除霧、去雨/雪及水下強化之數位影像技術

Single Image Dehazing, Rain/Snow Removal and Underwater
Enhancement Using Digital Image Processing

蔡雨泰

Yu-Tai Tsai

指導教授：貝蘇章 博士

Advisor: Soo-Chang Pei, Ph.D.

中華民國 103 年 6 月

June, 2014



國立臺灣大學（碩）博士學位論文
口試委員會審定書

單一影像除霧、去雨/雪及水下強化之數位影像技術
Single Image Dehazing, Rain/Snow Removal and
Underwater Enhancement Using Digital Image Processing

本論文係蔡雨泰君（R01942057）在國立臺灣大學電信工程學研究所完成之碩（博）士學位論文，於民國 103 年 5 月 24 日承下列考試委員審查通過及口試及格，特此證明

口試委員：

貝 蘇 亭

（簽名）

（指導教授）

徐忠枝

馮世邁

李枝宏

常文河

吳宗霖

（簽名）

所 長



誌謝



在台灣大學電信工程研究所的這兩年裡，要感謝的人實在是不勝枚舉，首先要感謝的是我的指導教授貝蘇章老師！從貝老師身上，讓我看到為人師表的最佳典範，老師不但以身作則每天陪我們一起在實驗室奮鬥努力，臉上總是不忘帶著親切又溫暖的笑容。透過循循善誘的指導，耐心的聆聽我們每一次的報告，使我們總能從中獲益良多且伴隨著愉快的心情和新的想法！能夠成為老師的學生跟老師一起作研究，真的覺得自己又幸運又幸福，真的很謝謝老師。

再來是要感謝所有教導過我和幫助過我的老師們，因為有您們認真的教學和熱心的幫助，讓我在求學的過程中多采多姿，豐富又充實，謝謝您們～

還有要謝謝實驗室的學妹、同學和學長姐們，因為有你們的陪伴，讓我的研究所生活充滿了快樂的回憶！

最後要感謝我的家人，因為有你們義無反顧的支持我，讓我可以毫無後顧之憂的當個全職又快樂的學生，並且鼓勵我作自己想做的事、勇敢追尋自己的夢想！每當我遇到困難或挫折時，你們總是會陪伴著我，給我最溫暖的依靠，讓我覺得我是全世界最幸福的孩子，我會好好珍惜這所有的一切，並且繼續努力追尋自己的目標與理想，讓自己成為一位可以幫助很多人，一位有能力的人！

在此對所有幫助過我的人、愛我的人，獻上最真誠的感謝～



中文摘要



在惡劣環境下所造成的低能見度，是許多電腦視覺應用的主要問題，如監視，智能車輛，室外物體識別等。這是由於大氣微粒大量存在於參與介質(participating medium)中並且有顯著的分佈和大小時，所造成的現象。基於這一現象，可以將氣候狀況分為靜態和動態兩類。靜態的惡劣氣候是由很多微小的粒子所造成的，其通常在時間和空間上是一致的，如霧和霾；相反地，動態的惡劣氣候是由較大的粒子所造成的，如雨滴和雪花，其在分析上較靜態惡劣氣候困難，主要是因為被雨和雪影響的鄰近區域，在時間和空間上是不同的。然而在水下攝影所造成的低能見度，最主要的原因是由於色偏及色散現象所造成的。色偏現象為光線於水中傳播時，因不同波長具相異之能量衰減程度，而令水下環境呈現偏藍色調；色散現象則為物體反射光線經水中粒子吸收與多次漫射所造成的，色散現象會對影像產生能見度與對比降低的影像。這些狀況不僅會困擾和混淆人類的觀察者，還會降低那些依賴微小特徵的電腦視覺演算法之有效性，因此模擬在各種環境下所造成的視覺影響和發展出一套良好的演算法來移除與消除這些由懸浮微粒及光線衰減所造成的影響，變得不可或缺與重要的！

在本篇論文中，我們首先介紹目前最具代表性的三種單一影像除霧的方法：contrast-based, independent component analysis, 和 dark channel prior-based，並且基於 dark channel prior-based 的方法，我們更進一步的提出了一個有效且健全的方法來改善除霧的品質。相較於目前存在的方法，我們的方法除了可以對白天霧影像給予滿意的除霧品質，甚至對於夜晚霧影像，仍然可以提供良好的除霧結果。接著，我們介紹目前具代表性的四種去雨及除雪的方法：guidance image based, image decomposition analysis, adaptive nonlocal means filter, 和 frequency-based analysis。接著，我們另外提出了一個簡單但有效的去雨及除雪的方法，其主要的設計概念為將去雨及除雪的架構分成兩個部分，第一個部分為偵測及第二個部分為修補。除此之外，我們還介紹目前最具代表性的三種水下影像強化的方法：histogram-based equalization, wavelength-based compensation, 和 fusion based。接著，我們提出了一個簡單但有效的水像影像強化方法，其主要的設計概念為結合

色彩校正、對比度擴展及直方圖均化的方法，相較於目前存在的方法，是一個可以用較少的運算時間且可有效提高影像能見度與色彩保真度的方法，相信在優化的情況下，能在硬體上達到即時影像增強。



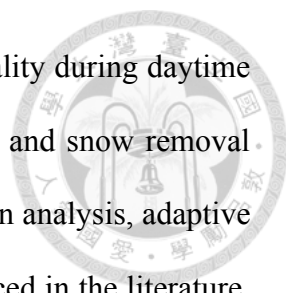
關鍵字：除霧、除霾、除雨、除雪、水下影像、影像復原、視頻復原、影像增強

ABSTRACT



Poor visibility in bad environment is a major problem for many applications of computer vision such as surveillance, intelligent vehicles, and outdoor object recognition, etc.... The reason is that the substantial presence of atmospheric particles has significant size and distribution in the participating medium. Based on this, weather conditions can be characterized as steady and dynamic cases. Specifically, steady bad weather such as fog and haze caused by microscopic particles is usually spatially and temporally consistent. Oppositely, dynamic bad weather such as rain and snow is made up of large particles. Because spatially and temporally neighboring areas are affected by rain and snow differently, the analysis is more difficult. However, the poor visibility in underwater photography is caused by light scattering and color shift. Color shift corresponds to the varying degrees of attenuation encountered by light traveling in the water with different wavelengths, rendering ambient underwater environments dominated by bluish tone. Light scattering is caused by light incident on objects reflected and deflected multiple times by particles present in the water before reaching the camera. This in turn lowers the visibility and contrast of the image captured. Under these conditions, the human viewer would be annoyed. They also degrade the effectiveness of any computer vision algorithm based on small features and varying degrees of attenuation. Therefore, it is necessary to model the visual effects for the various cases and then remove them.

In this thesis, we introduce three existing typical single image dehazing methods: contrast-based, independent component analysis, and dark channel prior-based. To improve the dehazing quality, we propose a robust and effective dehazing method.



Unlike other existing methods, there is the satisfactory dehazing quality during daytime and nighttime by our methods. And then, four existing typical rain and snow removal methods in single image: guidance image based image decomposition analysis, adaptive nonlocal means filter, and frequency-based analysis are also introduced in the literature. In this follows, we design a simple but effective method divide the rain or snow removal scheme into two parts, the first part is detection of rain or snow and the second part is inpainting. Besides, three existing typical underwater enhanced methods: histogram-based equalization, wavelength-based compensation, and fusion based are also introduced in the literature. In this follows, we design a simple but effective underwater enhanced method, and its main idea is combining the color correction, contrast stretching, and histogram equalization. Unlike other existing methods, we'll get a better result which takes less processing time and highly enhances visibility and superior color fidelity by our method. We believe that we'll run real-time on hardware in optimized circumstances.

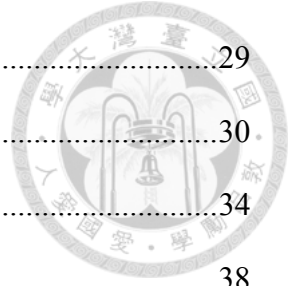
Keywords: Dehazing, Fog removal, Rain removal, Snow removal, Underwater Image, Image Restoration, Video Restoration, Image Enhancement.

CONTENTS



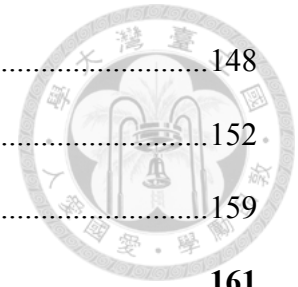
口試委員會審定書	#
誌謝	i
中文摘要	iii
ABSTRACT	v
CONTENTS	vii
LIST OF FIGURES	xi
LIST OF TABLES	xxiii
Chapter 1 Introduction	1
Chapter 2 Related Work of Single Image Dehazing	7
2.1 Introduction	7
2.2 Contrasted-Based	9
2.2.1 Basic Concept of Contrasted-Based Method	10
2.2.2 Advantage and Disadvantage	13
2.3 Independent Component Analysis	13
2.3.1 Basic Concept of Independent Component Analysis Method	13
2.3.2 Advantage and Disadvantage	19
2.4 Dark Channel Prior-Based	20
2.4.1 Basic Concept of Dark Channel Prior-Based Method	20
2.4.2 Advantage and Disadvantage	25
Chapter 3 Proposed Method of Single Image Dehazing	27
3.1 Introduction	27
3.2 Proposed Method for Daytime Haze	28

3.2.1	White Balance Correction	29
3.2.2	Color Space Conversion.....	30
3.2.3	Refined Transmission Coefficient Map.....	34
3.2.4	Post-Processing	38
3.3	Extended Proposed Method for Night Fog.....	40
3.3.1	Night Image Enhancement.....	41
3.3.2	Post-Processing	45
3.4	Experimental Results	46
3.5	Conclusions	58
Chapter 4	Related Work of Rain/Snow Removal in Single Image	59
4.1	Introduction	59
4.2	Guidance Image Based Method.....	63
4.2.1	Basic Concept of Guidance Image	63
4.2.2	Advantage and Disadvantage	67
4.3	Image decomposition.....	68
4.3.1	Basic Concept of image decomposition	68
4.3.2	Advantage and Disadvantage	71
4.4	Adaptive nonlocal means filter	71
4.4.1	Basic Concept of adaptive nonlocal means filter	71
4.4.2	Advantage and Disadvantage	74
4.5	Frequency-Based Analysis	75
4.5.1	Basic Concept of Frequency-Based Analysis Method	75
4.5.2	Advantage and Disadvantage.....	83
Chapter 5	Proposed Method of Rain/Snow Removal in Single Image.....	85
5.1	Introduction	85



5.2	Proposed Method.....	86
5.2.1	Fog Removal Pre-Processing.....	86
5.2.2	Rain/Snow Detection and Selection Process.....	87
5.2.3	Rain/Snow Removal Process	98
5.2.4	Impulse Noise Removal Process.....	100
5.2.5	Color Transfer Post-processing.....	103
5.3	Experimental Results.....	106
5.4	Conclusions	122
Chapter 6	Related Work of Underwater Image Enhancement.....	125
6.1	Introduction	125
6.2	Histogram-Based Equalization Based	128
6.2.1	Basic Concept of Histogram-Based Equalization.....	128
6.2.2	Advantage and Disadvantage.....	130
6.3	Wavelength-Based Compensation.....	131
6.3.1	Basic Concept of Wavelength Compensation.....	131
6.3.2	Advantage and Disadvantage.....	137
6.4	Fusion-Based	138
6.4.1	Basic Concept of Fusion-based.....	138
6.4.2	Advantage and Disadvantage.....	141
Chapter 7	Proposed method of Underwater Image Enhancement.....	143
7.1	Introduction	143
7.2	Proposed Method.....	144
7.2.1	Contrast Stretching and Color Correction.....	144
7.2.2	Variation on Histogram Stretching.....	146
7.2.3	Multiscale Mixing Process.....	148

7.2.4	Post-Processing	148
7.3	Experimental Results	152
7.4	Conclusions	159
Chapter 8	Conclusion and Future Work.....	161
REFERENCE	163



LIST OF FIGURES



Fig. 1.1	Pictorial description of the direct attenuation $D_a(x)$ and the airlight $A_r(x)$	2
Fig. 1.2	Haze image formation model. The color vector I is a linear combination of J and A in the RGB space.	3
Fig. 1.3	Relation between the functions and its corresponding images in (1.1).	3
Fig. 1.4	Comparison of the differences between the steady and dynamic weather.	5
Fig. 1.5	Raindrops fall on a car windshield. (a) Focused raindrop. (b) Unfocused raindrop.	5
Fig. 2.1	Some results of the polarization based method. (a) Perpendicular polarization components of the image. (b) Parallel polarization components of the image. (c) Dehazed image.	8
Fig. 2.2	Result of the normalization. (a) Input image. (b) Result of normalizing the environmental light.	11
Fig. 2.3	Results of enhancing visibility for an outdoor scene. (a) Input hazy image. (b) Direct attenuation. (c) The airlight of the input hazy image.	12
Fig. 2.4	Constant albedo model used in Fattal's work [2].	16
Fig. 2.5	Synthetic examples. (a)(e) Input image. (b) Recovered transmission t . (c) Recovered shading l . (d) Recovered J . The last three images (f-g) show the results obtained by using a wrong η , where the correlation between t and l is apparent.	16
Fig. 2.6	Dehazing based on a single input image and the corresponding estimation. (a) Input image. (b) Output image. (c) Depth estimation. (d) Shading	

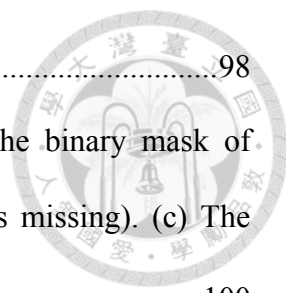
	component $I(x)$. (e) Transmission $t(x)$. (f) Extrapolated transmission. ...	19
Fig. 2.7	Relationship between haze-free outdoor images and their corresponding dark channel. (a) Haze-free outdoor images. (b) Dark channel corresponding to (a).....	21
Fig. 2.8	Haze removal process. (a) Input haze image. (b) Estimated transmission map. (c) Refined transmission map after soft matting. (d) Final haze-free image.	24
Fig. 2.9	Haze removal results. (a) Input haze images. (b) Final haze-free image.	24
Fig. 2.10	Flow chart of the dark channel prior [3].....	25
Fig. 3.1	Flow chart of the proposed dehazing technique in daytime.	28
Fig. 3.2	Illustration of the white balance correction. (a) Input image. (b) White balance corrected image. (c) Dehazed without the white balance correction. (d) Dehazed after the white balance correction.	30
Fig. 3.3	<i>HSI</i> color model.....	32
Fig. 3.4	Comparison of the dehazing result under two different cases of transmission map t . (a) Input haze image. (b) Results for the block-based transmission map. (c) Results for the pixels-based transmission map.....	34
Fig. 3.5	(a) <i>RGB</i> image. (b) Hue image. (c) Saturation image. (c) Intensity image. ...	36
Fig. 3.6	Insufficient brightness and non-uniform distributed haze images. (a) Input hazy image. (b) Estimated transmission. (c) Refined transmission. (d) Final dehazing image.	38
Fig. 3.7	Comparisons of results by the proposed method in the images. (a) Input haze image. (b) Final dehazing image (improved scene radiance). (c) Final dehazing image by post-processing (adjusted image).	40
Fig. 3.8	Flow chart of the proposed method for night fog.....	41

Fig. 3.9	Flow chart of the proposed nighttime enhancement method.....	44
Fig. 3.10	Insufficient brightness images. (a) Input image. (b) Final enhanced image.	44
Fig. 3.11	Insufficient brightness and non-uniform distributed haze compare with BFLCC post-processing. (a) The input nighttime hazy image. (b) Final dehazing image. (c) Final dehazing image with BFLCC post-processing. ..	46
Fig. 3.12	Comparative results of the proposed method and the conventional methods on the “house” image. (a) The input hazy image. The dehazed images obtained by (b) He et al.’s method [3], (c) Pei et al.’s method [39] , (d) Nishino et al.’s method [45], (e) Kim al.’s method [44], and (f) the proposed method.	50
Fig. 3.13	Comparative results of the proposed method and the conventional methods on the “train” image. (a) The input hazy image. The dehazed images obtained by (b) He et al.’s method [3], (c) Pei et al.’s method [39], (d) He et al.’s method with multiple scattering model [40], (e) C. O. Ancuti al.’s method [41], and (f) the proposed method.	51
Fig. 3.14	Comparative results of the proposed method and the conventional methods on the “sweden” image. (a) The input hazy image. The dehazed images obtained by (b) Tan et al.’s method [3], (c) Zhang al.’s method [46], (d) Nishino al.’s method [45], (e) C. O. Ancuti al.’s method [41], and (f) the proposed method.....	51
Fig. 3.15	Comparative results of the proposed method and the conventional methods on the “ny12”, “ny17”, and “y01” images. (a) The input hazy image. The dehazed images obtained by (b) Tan et al.’s method [1] (2008), (c) Fattal et al.’s method [2] (2008), (d) He et al.’s method [3] (2009), (e) Nishino et al.’s method [45] (2012), (f) Kim al.’s method [44] (2013), (f) C. O. Ancuti al.’s	

	method [41] (2013), and (f) the proposed method.....	53
Fig. 3.16	Comparative results of the proposed method and the conventional methods on the nighttime haze images. (a) The input nighttime hazy images. The dehazed images obtained by (b) He et al.'s method [3], (c) Pei et al.'s method [32], and (d) the proposed method.....	54
Fig. 3.17	Comparison of nighttime dehazed results: (a) Image quality metric. (b) He et al.'s results extracted from Fig 3.15 when applied IQM metric. (c) Pei et al.'s results extracted from Fig 3.15 when applied IQM metric. (d) Our results.....	55
Fig. 3.18	Comparative results of the proposed method and the conventional methods on the nighttime haze images. (a) The input nighttime hazy images. The dehazed images obtained by (b) Pei et al.'s method [32], and (c) the proposed method.....	56
Fig. 3.19	Comparative results of the proposed method on the underwater image (up: PICT0403 and bottom: PICT0422). (a) Input underwater image. (b) Final enhancing image by proposed dehazing method. (c) Final enhancing image by proposed underwater enhancement method (i.e., mentioned in chapter 7).....	57
Fig. 4.1	Behavior of each drop.....	60
Fig. 4.2	Field view of a raindrop.....	60
Fig. 4.3	Brightness levels produced by raindrops.....	60
Fig. 4.4	Comparison of visual effects in two images at different exposure times. (a) Image with rain captured in high shutter speed (exposure time = 1/1000 s). (b) Image with rain captured in normal shutter speed (exposure time = 1/30 s).	61
Fig. 4.5	Distribution of a typical rainfall and the shapes of raindrops with various	

	sizes. (a) Drop size distribution. (b) Shapes of raindrops.....	62
Fig. 4.6	Flow chart of the algorithm proposed by Xu. et al. [4].	66
Fig. 4.7	The results of the rain and snow removal: (a) Input rain/snow image. (b) The removal results by using guidance image. (c) The removal results by using refined guidance image.....	67
Fig. 4.8	Flow chart of the algorithm proposed by Kang. et al. [5].	70
Fig. 4.9	The proposed by Kang. et al. based on two learned local dictionaries [5]...	70
Fig. 4.10	An example of the rain streak map [6]. (a) Input image. (b) The angel map of rotation angle θ_p . (c) The ratio map λ_p/μ_p of eigenvalues. (d) The extracted rain streak map.	74
Fig. 4.11	Fourier transform of the streaks.....	76
Fig. 4.12	Raindrops and snowflakes create streaks of different appearances, depending on factors such as the environmental illumination, their depth from the camera, and how much they are in focus. (a) A streak from a real raindrop. (b) A streak from a real snowflake. (v) A blurred Gaussian.....	77
Fig. 4.13	Physical meaning of the streak approximation model in (4.6).	77
Fig. 4.14	Streak orientation.	78
Fig. 4.15	Results from the iterative removal method on two sequences with moving cameras and scenes. (a) Sequence in the original video. (b) Derain and desnow results, respectively. (c) Improved estimation of rain and snow image with temporal information.	81
Fig. 4.16	Flow chart of the paper proposed by Barnum et al. [7].	82
Fig. 5.1	Flow chart of the proposed method.	86
Fig. 5.2	Result of the fog removal pre-processing. (a) Input snow image. (b) Results	

	after applying fog removal pre-processing	86
Fig. 5.3	Segmentation of dark versus clear region. (a) Original image. (a) The sky region. (b) The dark region (raindrops are visible in this region).....	87
Fig. 5.4	Power spectral distributions of rain and snow images in frequency domain. (a) The original images. (b) Its two dimensional Fourier transform.	88
Fig. 5.5	The passible rain candidates with different threshold (initial binary field). (a) Input rain image. (b) The passible rain candidates (TH_1 is set to A). (c) The passible rain candidates (TH_1 is set to smaller than A). (d) The passible rain candidates (TH_1 is set to larger than A).	90
Fig. 5.6	Flow chart of the rain or snow detection process with first property.	90
Fig. 5.7	The histogram distribution of the RGB components. (a) The original snow image. (b) Its histogram distribution of RGB components.....	91
Fig. 5.8	Flow chart of the rain or snow detection process with second property.....	93
Fig. 5.9	(a) The regions selected for investigation. (b) The mean R , G , and B values of the pixels in the selected regions. (c) The corresponding means the standard deviation of ΔR , ΔG , and ΔB	94
Fig. 5.10	Flow chart of the rain or snow detection process with third property.	96
Fig. 5.11	Result of the identification of snow streaks by our proposed method. (a) All potential snow streaks (initial snow binary map). (a) All potential snow streaks (initial snow jet colormap). (b) Initial snow mask refined by area restrict.....	97
Fig. 5.12	Schematic diagram of rain or snow extending.	97
Fig. 5.13	The result of combination process. (a) The original snow image. (b) The first binary field. (c) The second binary field. (d) The combined binary	



field.....98

Fig. 5.14 Image inpainting. (a) The original input image. (b) The binary mask of missing area ($M_i = 1$ defines the pixel indexed by i is missing). (c) The image after inpainting.....100

Fig. 5.15 The membership function μ_{large} 102

Fig. 5.16 Impulse noise detection result. (a) The image after rain removal. (b) Zoom-in patch of (a). (c) The detected result of impulse noise.....103

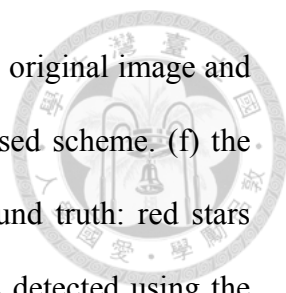
Fig. 5.17 Transfer process of snow images by using the proposed method. (a) The original snow image. (b) The result of snow removal. (c) The result of snow removal is further used to haze remove by our proposed method. (d) The result after the color transfer mapping.....106

Fig. 5.18 Comparison of rain removal results: (a) the original rain image; the rain-removed version via: (b) Kang et al.'s method with the single-frame-based image decomposition [5], (c) Kim et al.'s method with the adaptive nonlocal mean filter [6]; and (d) the proposed rain removal scheme.110

Fig. 5.19 Comparison of rain removal results: (a) the original rain image; the rain-removed version via: (b) Xu et al.'s method with the guided filter [4]; (c) Kang et al.'s method with the single-frame-based image decomposition [5]; and (d) the proposed rain removal scheme.113

Fig. 5.20 Comparison of snow "streak" removal results: (a) the original snow image; the snow-removed version via: (b) Xu et al.'s method with the guided filter [4]; (c) Kang et al.'s method with the single-frame-based image decomposition [5]; and (d) the proposed snow removal scheme.115

Fig. 5.21	Comparison of snow “streak” removal results: (a) the original snow image; the snow-removed version via: (b) Xu et al.’s method with the guided filter [4]; (c) Xu et al.’s method with the refined guidance image [4]; and (d) the proposed snow removal scheme.	116
Fig. 5.22	Snowflakes removal results: (a) Input snow images. (b) Our results.	116
Fig. 5.23	Comparison of rain streaks removal results: (a) the sitting man sequence. (b) rain removal by the frequency-based analysis [7]. (c) the proposed rain removal scheme.	117
Fig. 5.24	Comparison of rain streaks removal results: (a) the window building sequence. (b) rain removal by the frequency-based analysis [7]. (c) the proposed rain removal scheme.	117
Fig. 5.25	Comparison of snow removal results: (a) the mailbox sequence. (b) snow removal by the frequency-based analysis [7]. (c) the proposed snow removal scheme.	118
Fig. 5.26	Comparison of snow removal results: (a) the walker in the snow sequence. (b) snow removal by the frequency-based analysis [7]. (c) the proposed snow removal scheme.	118
Fig. 5.27	Comparison of rain drops removal results: (a) smartphone shot through a rainy window on a train. (b) rain removal by [61]. (c) the proposed rain removal scheme.	119
Fig. 5.28	Comparison of focused raindrops detection results: (a) original image acquired by camera. (b) the dark region. (c) raindrops detected by our proposed scheme. (d) the result after the proposed rain removal scheme. .	120
Fig. 5.29	Comparison of unfocused raindrops detection results: (a) original image acquired by camera. (b) the dark region (raindrops are visible in this region).	



(c) the background image. (d) the difference between the original image and background image. (e) raindrops detected by our proposed scheme. (f) the result after the proposed rain removal scheme. (g) ground truth: red stars correspond to the mark made by operator. (h) raindrops detected using the background subtraction method [63]. Green: correctly detected raindrops. Blue: missed raindrops. Red: false detection.....121

Fig. 5.30 Comparison of unfocused raindrops detection results: (a) original image acquired by camera. (b) the dark region (raindrops are visible in this region). (c) raindrops detected by our proposed scheme. (d) the result after the proposed rain removal scheme.122

Fig. 6.1 Absorption of light by water.126

Fig. 6.2 Results of the polarization based method. (a) the white balanced raw frame. (b) the final restored raw frame.127

Fig. 6.3 Result of histogram equalization for an underwater image. (a) Original underwater image, (b) HE image, and (c) CDF of original underwater image and HE image in gray level.129

Fig. 6.4 Comparison with the equalization method for an underwater image. (a) Original underwater image, (b) HE image, and (c) CLAHE on *RGB* color model image.130

Fig. 6.5 Underwater optical imaging model (Y. Schechner et al.).132

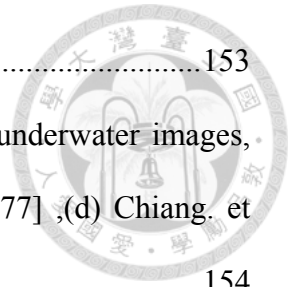
Fig. 6.6 Flow chart of the paper proposed by Chiang et al. [9].132

Fig. 6.7 Comparison the luminance contributed by an artificial light source. (a) Illuminated by an artificial light source, the intensity of the foreground appears brighter136

Fig. 6.8 Flow chart of the algorithm proposed by C. Ancuto. et al. [10].140

Fig. 6.9	The corresponding normalized weight maps: (a) Laplacian contrast. (b) Local contrast. (c) Saliency. (d) Exposedness.	140
Fig. 7.1	Flow chart of the proposed enhancing technique in underwater.	144
Fig. 7.2	The histogram of contrast stretching. (a) Original underwater image, (b) Result after saturation and intensity stretching on <i>HSI</i> colour model, (c) Histogram of original underwater image in gray level and Stretched one in gray level.	145
Fig. 7.3	Result of traditional enhancing technologies for underwater images and the color correction process of underwater images by using the proposed method. (a) Original underwater image, (b) White balance image, (c) CLAHE image, (d) Result after contrast stretching (only step 1), (e) Result after modifying the mean value (only step 2), and (f) Our method with color correction (process step1 and step2).	146
Fig. 7.4	Compare the histogram stretching within a $L^*a^*b^*$ color space and in an RGB color space. (a) Original image. (b) Stretching within a $L^*a^*b^*$ color space. (c) stretching in <i>RGB</i> color space.	147
Fig. 7.5	The results of multiscale mixing process. (a) Input underwater image. (b) The enhanced result after contrast stretching. (c) The enhanced result after CLAHE. (d) The final restored image.	148
Fig. 7.6	Insufficient brightness and non-uniform distributed haze. (a) Input underwater image. (b) Fusion-based [10]. (c) Final enhancing image. (d) Final enhancing image by post-processing.	151
Fig. 7.7	Comparison of underwater enhanced results: (a) Image quality metric. (b) Chiang. et al.'s results [9] (top row) and C. Ancuto. et al.'s results [10] extracted from Fig 7.8 and Fig 7.9 when applied IQM metric [76]. (c) Our	

	results.....	153
Fig. 7.8	Comparison of underwater enhanced results: (a) Input underwater images, (b) Histogram equalization, (c) Chao. et al.'s method [77] ,(d) Chiang. et al.'s method [9], and (e) Our proposed method.....	154
Fig. 7.9	Comparison of underwater enhanced results: (a) Input underwater images. (b) C. Ancuto. et al.'s results [10]. (c) Our results.....	156
Fig. 7.10	Underwater enhanced results: (a) Input underwater images. (b) Our final enhanced results.....	158





LIST OF TABLES



Table 1.1	Weather condition and associated particle types.	2
Table 3.1	75% <i>HSI</i> Color Bars. For consistency with the <i>HSV</i> model, we have changed from the Tektronix convention of blue at 0°.	33
Table 3.2	Qualitative Comparison of the two images (PICT0403 and PICT0422) show in Fig. 3.17. Based on the indicators of Hautiere et al. [13].	57
Table 7.1	Qualitative Comparison of the two images (PICT0403 and PICT0422) show in Fig. 7.6. Based on the indicators of Hautiere et al. [13].	150



Chapter 1 Introduction



In order to develop vision systems that present under all weather conditions, it is essential to model the visual effects of the various weather conditions and develop algorithm to remove them. Weather conditions vary widely in their physical properties and produce visual effects in images. Based on the types and size of the particles and their concentration in space [11] as illustrated in Table 1.1, weather conditions can be typed as steady and dynamic. In the case of the steady weather, individual droplets are too small (1-10 μm) to be visible to a camera, and the intensity at a pixel is caused by the aggregate effect of large number of droplets within the pixel's solid angle such as fog, mist, and haze. The haze image model proposed in [1], [2], [11], [12] and [13] is widely applied in computer vision and can be adequately described the effects of steady weather, as

$$I(x) = J \cdot t(x) + A \cdot (1 - t(x)) \quad (1.1)$$

or

$$I(x) = L_{\infty} \rho(x) e^{-\beta d(x)} + L_{\infty} (1 - e^{-\beta d(x)}) \quad (1.2)$$

where (1.1) is equal to (1.2), I is the observed intensity of the haze image, x is the pixel's index, J (i.e., $J = L_{\infty} \rho(x)$ with ρ being the reflectance of an object in the image) is the scene radiance of the haze-free image which is desired to be obtained by dehazing techniques, t (i.e., $t = e^{-\beta d(x)}$ with β being the atmospheric attenuation coefficient) is the medium transmission expressed part of light that is not scattered and reaches the observer, and A (i.e., $A = L_{\infty}$) is the global atmospheric light. The first term is the direct attenuation $D_a(x)$ ($D_a(x) = L_{\infty} \rho(x) e^{-\beta d(x)} = J \cdot t(x)$), and the second term is

the airlight $A_r(x)$ ($A_r(x) = L_\infty(1 - e^{-\beta d(x)}) = A \cdot (1 - t(x))$). Note that the haze removal technique is to estimate the global atmospheric light (A) and the medium transmission (t) from the haze image model (I), and the scene radiance (J) can be estimated by these estimated components. Fig. 1.1 shows the pictorial description of the direct attenuation $D_a(x)$ and the airlight $A_r(x)$. In (1.1), it geometrically means that in RGB color space, the vector I is a linear combination of the two vectors J and A . (see Fig. 1.2). In Fig. 1.3, it depicts the relation between $I(x)$, $J(x)$, and $t(x)$ in (1.1) to corresponding images.

Condition	Particle Type	Radius (μm)	Concentration (cm^{-3})
Air	Molecule	10^{-4}	10^{19}
Haze	Aerosol	$10^{-2} - 1$	$10^3 - 10$
Fog	Water droplet	$1 - 10$	$100 - 10$
Cloud	Water droplet	$1 - 10$	$300 - 10$
Rain	Water drop	$10^2 - 10^4$	$10^{-2} - 10^{-5}$

Table 1.1 Weather condition and associated particle types.

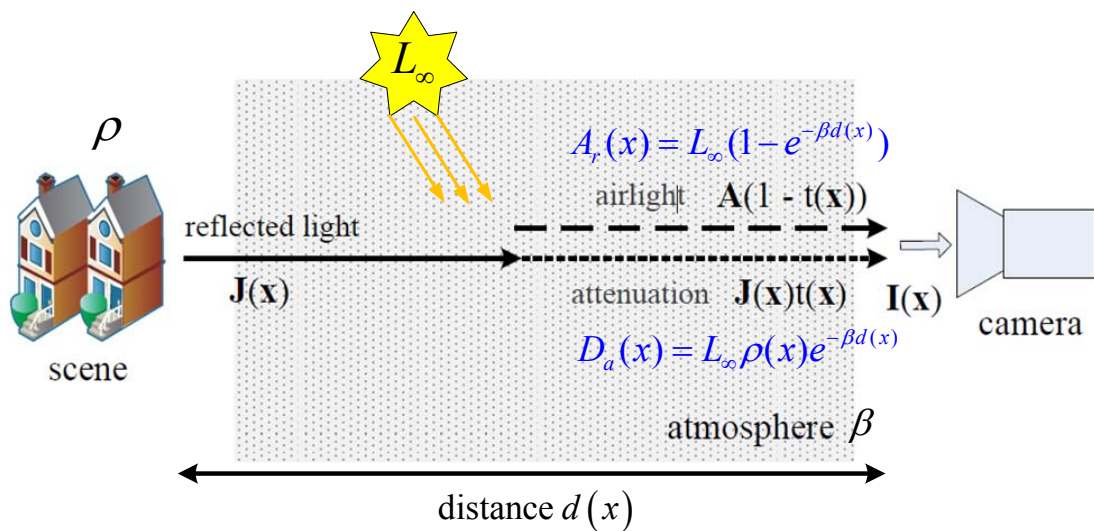


Fig. 1.1 Pictorial description of the direct attenuation $D_a(x)$ and the airlight $A_r(x)$.

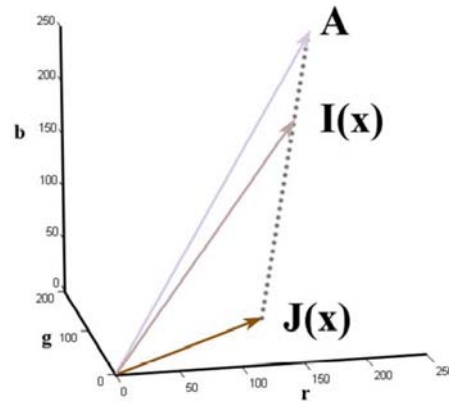


Fig. 1.2 Haze image formation model. The color vector I is a linear combination of J and A in the RGB space.

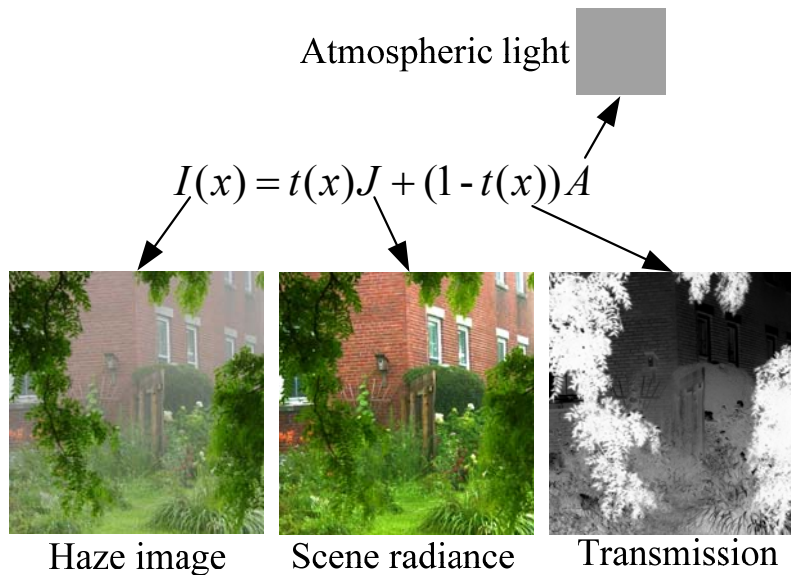
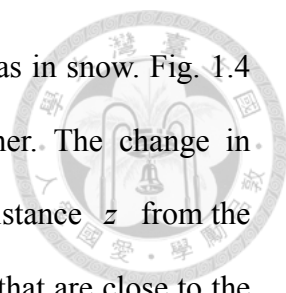


Fig. 1.3 Relation between the functions and its corresponding images in (1.1).

In the other case of the dynamic weather, individual particles are visible in the image ($0.1\text{--}10\text{mm}$) and the aggregate scattering models used for steady conditions are not applicable in here such as rain, snow, and hail. But, when raindrops and snow are very far from the camera, their visual effects are very weak and appear as fog. Therefore, what we focus on are rain and snow that are close to the camera and fall on a car windshield. The analysis of dynamic weather conditions requires the development of stochastic models that capture the spatial and temporal effects of a large number of



particles moving at high speeds as in rain and complex trajectories as in snow. Fig. 1.4 compares the differences between the steady and dynamic weather. The change in intensity produced by a falling raindrop as a function of the drop's distance z from the camera. The change in intensity ΔI does not depend on z for drops that are close to the camera ($z < z_m$). While for raindrops far from the camera ($z > z_m$), ΔI decreases as $1/z$ and for distances greater than Rz_m (where R is a constant), ΔI is too small to be detected by the camera, only produce aggregate scattering effects. Therefore, the visual effects of rain are only due to raindrops that lie close to the camera ($z < Rz_m$) which we refer to as the rain visible region. The value R depends on the brightness of the scene and camera sensitivity. However, raindrop is considered to be a water droplet on a car windshield which can distort the view especially during driving. Depending on the speed, raindrop flies upward as the speed increasing and flows downward as the speed is slowing down. Nevertheless, water droplet on dirty windshield is not in a spherical form is why the view becomes blurred, and the circumstance is known as unfocused raindrops. Focused raindrops can be seen in a spherical form on windshield as shown in Fig 1.5(a) and unfocused raindrops which cause blurring view as shown in Fig 1.5(b) are vice versa. Both types of raindrop lead to challenging tasks in terms of detecting and removing the raindrop.



Steady Weather (Fog, Mist)

Dynamic Weather (Rain, Snow)

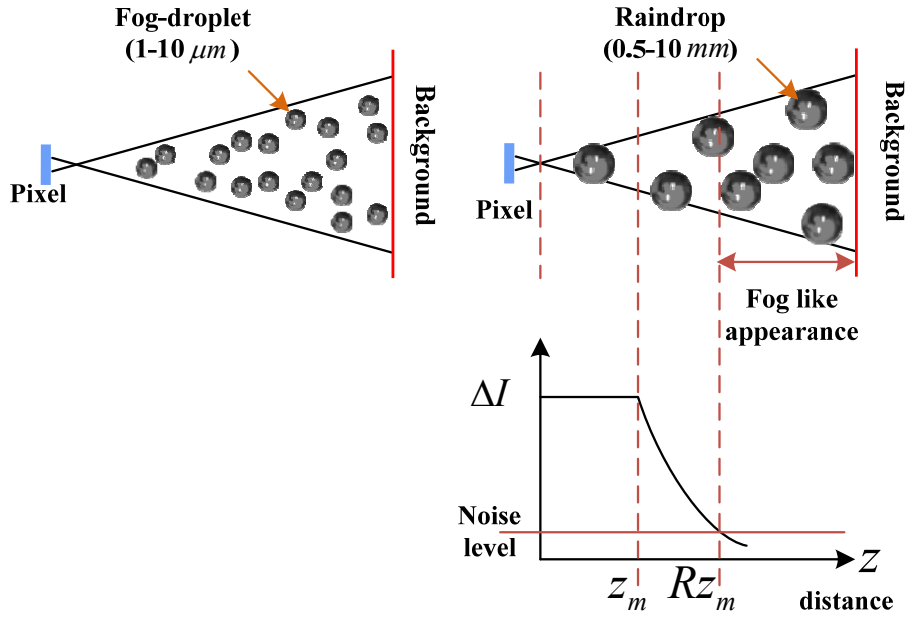


Fig. 1.4 Comparison of the differences between the steady and dynamic weather.

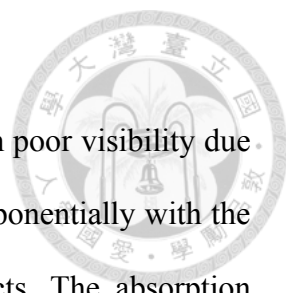


(a)



(b)

Fig. 1.5 Raindrops fall on a car windshield. (a) Focused raindrop. (b) Unfocused raindrop.



Different from common images, underwater images suffer from poor visibility due to the attenuation of the propagated light. The light is attenuated exponentially with the distance and depth mainly due to absorption and scattering effects. The absorption substantially reduces the light energy while the scattering causes changes in the light direction. The random attenuation of the light is the main cause of the foggy appearance while the fraction of the light scattered back from the medium along the sight considerably degrades the scene contrast. By the way, dehazing techniques [14] have been related with the underwater restoration problem.

The remaining of this thesis is organized as follows. In Chapter 2, we introduce three existing typical single image dehazing methods. In Chapter 3, we propose a robust and effective dehazing method based on human vision to improve the dehazing quality during daytime and nighttime. Four existing typical rain and snow removal methods are also introduced in Chapter 4. For rain and snow removal investigations, we design a simple but effective rain or snow removal method by divide the rain or snow removal scheme into two parts, the first part is detection of rain or snow and the second part is inpainting in Chapter 5. In Chapter 6, we introduce three existing typical underwater enhancement methods. In Chapter 7, we propose an effective enhancing method to improve the underwater image quality. Chapter 8 concludes this thesis and discusses the future work.

Chapter 2 Related Work of Single Image Dehazing



Haze removal is a challenging problem because of the unknown transmission, depth information and ill-posed conditions. The key characteristics of light such as intensity and color are changed by its interactions with the atmosphere. These interactions can be classified into three categories: scattering, absorption, and emission. As a result, haze is occurred due to atmospheric absorption and scattering by a complex medium (e.g. dust, mist, or fumes.), at which the irradiance received by the camera from the scene point is attenuated along the line of sight. Furthermore, the incoming light reflected from the scenes, and further blends it with some additive light are produced by the ambient light reflecting into the line of sight by atmospheric particles. The degraded images lose the contrast and color reality. Thus, remove haze form images becomes an important and desired in many applied field especially in computer vision and computer graphics areas.

2.1 Introduction

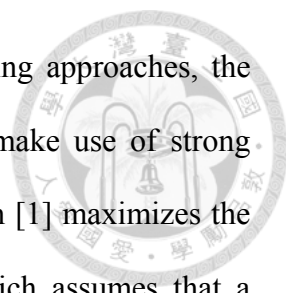
Dehazing is the well-known procedure of removing haze effects from capturing images while recovering the original details and the colors of natural scenes. Because the number of known variables is less than the number of unknown variables and the depth information is unknown, it needs multiple images or extra information for estimating. Therefore many methods have been proposed by using multiple images or extra information. The first method is the polarization based method (e.g. [15], [16]) used by polarizing filters. The main idea of this approach is to exploit two or more images of the same scene that have different degrees of polarization (DOP), which are

obtained by rotating a polarizing filter attached to the camera. However, the common drawback of the methods in this approach is that they cannot be used to existing image dataset and applied to dynamic scenes for which the changes are more rapid than the filter rotation in finding the maximum and minimum DOP. Fig. 2.1 shows some results by applying the polarization based method, including the perpendicular and the parallel polarization components of the scene ((a) and (b)), and the final resulting dehazed image (c).



Fig. 2.1 Some results of the polarization based method. (a) Perpendicular polarization components of the image. (b) Parallel polarization components of the image. (c) Dehazed image.

The second method by using multiple images is taken in different weather condition (e.g. [17], [18], [19], [20]). The basic idea of this method is to manipulate on the differences of two or more images of the same scene that have different properties of the participating medium. Although the methods in this approach can significantly enhance visibility, their requirements make them unable to deliver the results immediately because they have to wait until the properties of the medium change. The third is depth based method, which demands the rough depth information from approximated 3D geometrical model of the input scene (e.g. [21], [22], [23]).

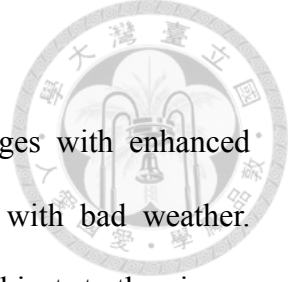


In order to overcome the limitation of multiple image dehazing approaches, the single image algorithms have been developed. These algorithms make use of strong assumptions or constraints to remove haze from a single image. Tan [1] maximizes the local contrast of the restored image from single input image which assumes that a dehazed image should have high contrast. Fattael [2] estimates the albedo and the depth of the scene, and then infers the medium transmission under the assumption that the transmission, object depth and surface shading were locally uncorrelated. Kartz and Nishion [12] estimates the objects depth and the albedo jointly by modeling a hazy image as a factorial Markov random field (FMRF). Tarel and Hautiere [13] estimates the atmospheric veil, which is the map of blended atmospheric light, and refined the veil using the median filter. He et al. [3] estimates the transmission map in a hazy image based on the dark channel prior and applies an alpha matting technology to refine it. Ancuti et al. [24] reduces the complexity of He et al. [3] algorithm by modifying the block-based approach to a layer-based one. Furthermore, there are many algorithms adapt and improve on He et al. [3] algorithm (e.g. [25], [26], [27], [28]).

In the following sections, we will specifically introduce these three typical single image dehazing methods (e.g. [1], [2], [3]), respectively.

2.2 Contrasted-Based

The contrast-based method had been proposed by Tan [1] in 2008. He observed that the dehazed image should have high contrast and a smooth layer of airlight than the inprocessed version of the hazy image. Based on this observation, he maximizes the local contrast of the restored image from single input image to remove the hazy component.



2.2.1 Basic Concept of Contrast-Based Method

This method is based on two basic observations. First, images with enhanced visibility (or clear-day images) have more contrast than images with bad weather. Second, airlight whose variation mainly depends on the distance of objects to the viewer tends to be smooth. Tan [1] intends to use chromaticity to describe (1.2), and thus define image chromaticity as follows

$$\sigma_c = \frac{I_c}{I_r + I_g + I_b} \quad (2.1)$$

where c is the color channel. Then, the atmospheric light L_∞ is estimated by finding a small spot that has the highest intensity in image I , from which the light chromaticity α derived from (2.1) can be obtained, when the object distant is assumed infinitely ($d = 0$, since $e^{-\beta d} = 0$) in (1.2), as

$$\alpha_c = \frac{L_{\infty c}}{L_{\infty r} + L_{\infty g} + L_{\infty b}} \quad (2.2)$$

Accordingly if we assume that there is no effect of scattering particle ($e^{-\beta d} = 1$), implying the absence of the airlight, then the image chromaticity will depend solely on the direct attenuation. This chromaticity is also called “object chromaticity” and expressed as

$$\gamma_c = \frac{L_{\infty c} \rho_c}{L_{\infty c} \rho_r + L_{\infty g} \rho_g + L_{\infty b} \rho_b} \quad (2.3)$$

Therefore, by using (2.2) and (2.3), the haze image model (1.1) in terms of chromaticity is rewritten as

$$I(x) = D(x)e^{-\beta d(x)}\gamma(x) + A(x)\alpha \quad (2.4)$$

where

$$D(x) = L_{\infty r} \rho_r(x) + L_{\infty g} \rho_g(x) + L_{\infty b} \rho_b(x) \quad (2.5)$$

, and

$$A(x) = (L_{\infty c} \rho_r + L_{\infty g} \rho_g + L_{\infty b} \rho_b)(1 - e^{-\beta d(x)}) \quad (2.6)$$

After obtaining the light chromaticity, the illumination color of the I is removed by employing (2.7) to produce I' , as

$$I'_c(x) = \frac{I_c(c)}{\alpha_c} \quad (2.7)$$

Fig. 2.2 shows the result of the normalization.

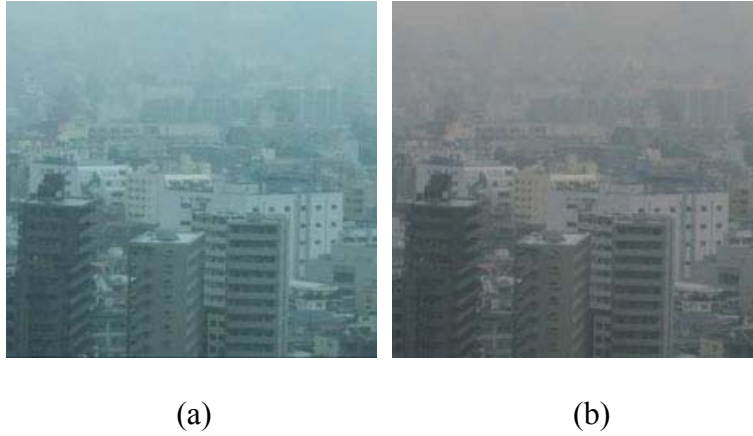
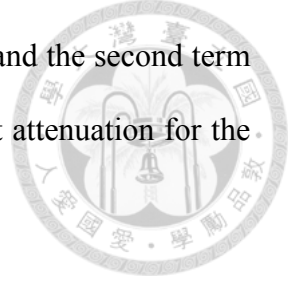


Fig. 2.2 Result of the normalization. (a) Input image. (b) Result of normalizing the environmental light.

Further, he computes the data and smoothness cost for every pixel. The data cost is computed from the contrast of a small patch cropped from the image, and the smoothness cost is computed from the difference or distance of the labels of two neighboring pixels, where the labels are identical to the airlight values. These data and smoothness costs build up complete MRFs in (2.8) that can be optimized by using the existing inference methods, producing the estimated values of the airlight A as

$$E(\{A_x\} | p_x) = \sum_x \phi(p_x | A_x) + \eta \sum_{x,y \in N_x} \psi(A_x | A_y) \quad (2.8)$$

where p_x is a small patch centered at location x , which is assumed to have a constant value of A_x . η is the strength of the smoothness term, and N_x represents the



neighboring pixels of x . They defined the first term is the data term and the second term is the smoothness term. Based on the estimated airlight A , the direct attenuation for the whole image finally can be computed as

$$D(x)r'(x) = (I'(x) - A(x) \begin{bmatrix} 1 \\ 1 \\ 1 \end{bmatrix}) e^{\beta d(x)} \quad (2.9)$$

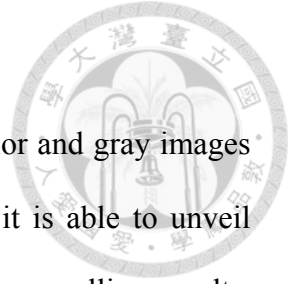
where $I'(x)$ is the normalized input image that the airlight color is white in (2.7) and $r'(x)$ is the normalized object chromaticity expressed as

$$r'_c(x) = \frac{r_c(x)}{\alpha_c} \quad (2.10)$$

For gray images, the algorithm is exactly the same, except skip the step to estimate light chromaticity and remove the illumination color. Note that, Tan [1] does not intend to fully recover the scene's original colors or albedo. His goal is to solely enhance the contrast of an input image so that the image visibility is improved. Fig. 2.3 shows an outdoor scene partially covered by haze, the direct attenuation image, and the airlight of the scene.



Fig. 2.3 Results of enhancing visibility for an outdoor scene. (a) Input hazy image. (b) Direct attenuation. (c) The airlight of the input hazy image.



2.2.2 Advantage and Disadvantage

The main advantage of this approach is that can apply both color and gray images without any geometrical information of the input image. Besides, it is able to unveil details and structures from the haze image, and then acquired the compelling results. However, in this method, some constraints may be limited the image quality. The first constraint is the halos at depth discontinuities caused by patch-based operation. The second constraint is that the output images have larger saturation values than those in the actual clear-day images and may not be physically valid. It is because the optimal data cost function and the actual values of A are unknown in the process.

2.3 Independent Component Analysis

Fattal [2] proposed an independent component analysis (*ICA*) approach in 2008. He estimates the albedo of the scene, and then infers the medium transmission under the assumption that the transmission and surface shading were locally uncorrelated.

2.3.1 Basic Concept of Independent Component Analysis Method

The main idea in this approach is that Fattal [2] formulates a refined image formation model that interprets the image through the surface shading(l) as well as the transmission function(t) from standard image formation model (1.1). Based on this model, the image is separated into two regions: constant-albedo and airlight-albedo ambiguity. Specifically, the two regions can be systematically resolved by searching a particular solution. The particular solution satisfies the local uncorrelated statistic for the resulting shading and transmission functions. A refined model is modeled the unknown image J as a pixel-wise product of surface albedo coefficients and a shading

factor expressed as

$$J(x) = l(x)R(x) \quad (2.11)$$

where l is a scalar describing the light reflected from the surface and R is a three-channel *RGB* vector of surface reflectance coefficients. He assumes $R(x)$ is piecewise constant and airlight (A) is known when the region with uniform albedo. Thus, the standard image formation model in (1.1) become

$$I(x) = t(x)l(x)R + (1-t(x))A \quad (2.12)$$

Then, they break R into a sum of two components, one is parallel to the airlight A and the other is orthogonal to the airlight $R' \in A^\perp$. In terms of these normalized components, (2.12) can be written as

$$I(x) = t(x)l'(x)(R'/\|R'\| + \eta A/\|A\|) + (1-t(x))A \quad (2.13)$$

where $l' = l/\|R'\|$ and $\eta = \langle R, A \rangle / (\|R'\|\|A\|)$ measuring the component that is mutual to the surface albedo and the airlight. Note that $\langle \cdot, \cdot \rangle$, they defined the standard three-dimensional dot-product in the *RGB* space. In order to obtain independent equations, the input image is projected onto these two directions as

$$I_A = \langle I(x), A \rangle = t(x)l'(x)\eta + (1-t(x))\|A\| \quad (2.14)$$

and

$$I_{R'} = \langle I(x), R' \rangle = \sqrt{\|I(x)\|^2 - I_A(x)^2} = t(x)l'(x) \quad (2.15)$$

where I_A is the projected image along the airlight vector and $I_{R'}$ is the projected image along R' . The transmission t can be written in terms of these two quantities as

$$t(x) = 1 - (I_A(x) - \eta I_{R'}(x)) / \|A\| \quad (2.16)$$

Thus, I_A , $I_{R'}$, and η are used to compute $t(x)$ and $l'(x)$. The airlight-albedo

ambiguity is explicit in (2.16) and can be resolved by finding η . The condition for finding η is that the transmission t and shading l are statistically uncorrelated over Ω (i.e., $C_\Omega(l, t) = 0$). The sample covariance C_Ω is estimated in the following

$$C_\Omega(f, g) = |\Omega|^{-1} \sum_{x \in \Omega} (f(x) - E_\Omega(f))(g(x) - E_\Omega(g)) \quad (2.17)$$

where $E_\Omega(f) = |\Omega|^{-1} \sum_{x \in \Omega} f(x)$. The parameter η is exactly obtained as follow

$$\eta = \frac{C_\Omega(I_A, h)}{C_\Omega(I_{R'}, h)} \quad (2.18)$$

where $h(x) = (\|A\| - I_A) / I_{R'}$. After given η , $t(x)$ can be computed by (2.17) and recover the haze-free image by

$$J(x) = \frac{I(x) - (1 - t(x))A}{t(x)} \quad (2.19)$$

where all $J(x)$ in the patch have the same direction of R , as shown in Fig. 2.4. In Fig. 2.5, it displays a synthetic example where the shading l consists of vertical ripples and the transmission t is made of radial ones. When estimating η from (2.18), these functions are accurately recovered, whereas the ones computed based on a false η appear to be mixed together (i.e., correlated).

Unfortunately, every measurement comes with noise, thus this is done by modeling the error present in I as additive white Gaussian noise by

$$I(x) = \tilde{I}(x) + \xi(x), \quad (2.20)$$

where ξ is a three dimensional vector of random Gaussian variables and is derived by the following progress $\xi \rightarrow \xi_A, \xi_{R'}, \xi_h \rightarrow \xi_\eta \rightarrow \xi_t$.

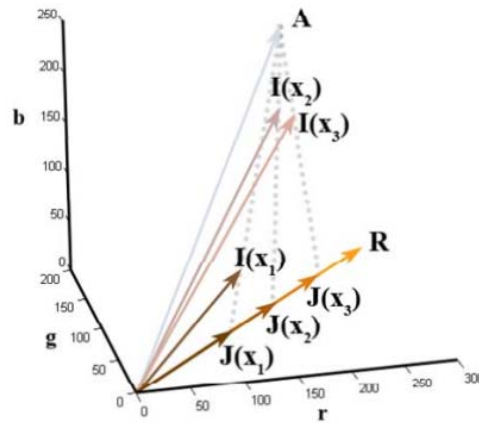


Fig. 2.4 Constant albedo model used in Fattal's work [2].

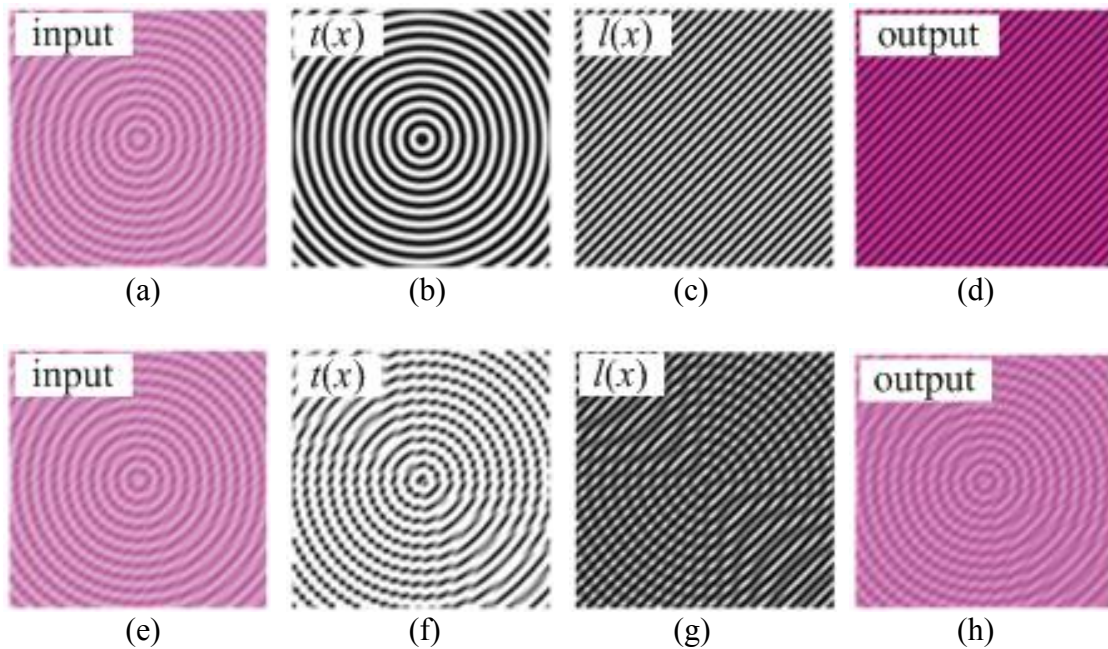


Fig. 2.5 Synthetic examples. (a)(e) Input image. (b) Recovered transmission t . (c) Recovered shading l . (d) Recovered J . The last three images (f-g) show the results obtained by using a wrong η , where the correlation between t and l is apparent.

The restricted case that all pixels correspond to the same surface (a constant albedo value $R(x) = R$) is introduced so far. In order to handle general images, Fattal [2] also considers the multi-albedo image case. The procedure is almost as same as the constant albedo image which is mentioned before. The differences between them are that he uses additional robust estimators and projects a naive haze-free image onto chroma channels

U and V of the YUV color space (not brightness or airlight in multi-albedo image). Then, a naïve haze-free image is computed by

$$I' = I - \frac{AI_A}{\|A\|} \quad (2.21)$$

, and a single chroma channel based on the ratio of these projections is extracted by

$$\theta(x) = \tan^{-1}\left(\frac{\langle I'(x), U \rangle}{\langle I'(x), V \rangle}\right) \quad (2.22)$$

This maps pixel color into angles where the distances can be measured by the length of the shortest arc that is

$$d(C_1, C_2) = \min\{|\theta_1 - \theta_2|, 2\pi - |\theta_1 - \theta_2|\} \quad (2.23)$$

This similarity measure defines the weight of the w -estimators in the following correlation

$$C_x(f, g) = \frac{1}{W_x} \sum_{y \in \Omega_x} (f(y) - E_x(f))(g(y) - E_x(g))w(x, y) \quad (2.24)$$

, and

$$E_x(f) = \frac{1}{W_x} \sum_{y \in \Omega_x} f(y)w(x, y) \quad (2.25)$$

where the weighting function $w(x, y)$ is given by

$$w(x, y) = \exp(-d(\theta(x), \theta(y))^2 / \sigma_\theta^2) \quad (2.26)$$

, the normalizing weight $W_x = \sum_{y \in \Omega_x} w(x, y)$, and $\Omega(x)$ is the window of pixels centered around x excluding pixels from discarded pixels (β). Finally, the Gauss-Markov model is defined as

$$P(t) \propto \prod_{x \notin \beta} e^{-t(x) - \hat{t}(x)^2 / \sigma^2 t(x)} \prod_{\forall x, y \in N} e^{-t(x) - t(y) / (I_A(x) - I_A(y))^2 / \sigma_s^2} \quad (2.27)$$

where $\hat{t}(x) = 1 - (I_A(x) - \eta I_{R'}(x)) / \|A\|$. $P(t)$ can be maximized by solving the linear

system resulting from $d \log P / dt = 0$, and the corresponding t is then taken from this optimum calculating result. The most probable t is used to compute J in (2.19).

In previous, Fattal [2] assumes that the airlight (A) is known. In the follows, he illustrates how to estimate the airlight color vector A . First, he backs to regions with uniform albedo in (2.12), which all pixels within a two-dimensional linear sub-space spanned by the vector A and R . Although the vector A and R can not be identified using a principal component analysis, the space can do it. This is applied in each of the given regions, indexed by i , and the two highest components are denoted by v_1^i and v_2^i . Finally, the airlight color vector A is found by searching for a vector with highest projection onto these sub-spaces as

$$\max_A \sum_i \langle A, v_1^i \rangle^2 + \langle A, v_2^i \rangle^2 \quad \text{such that } \|A\|^2 = 1 \quad (2.28)$$

By the way, every value of $\|A\|$ results in different pair l and t in (2.27). In Fig. 2.6, it shows the result for “wheat cones” with surfaces of distinct albedos, shading component and the transmission.

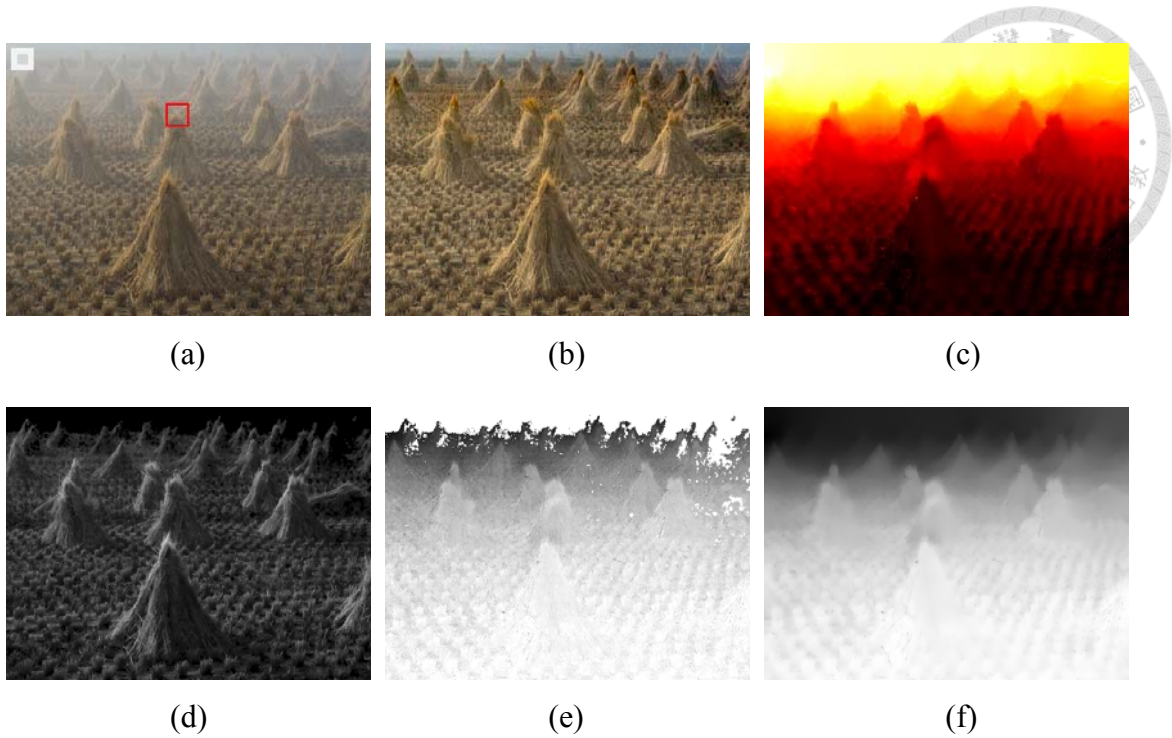


Fig. 2.6 Dehazing based on a single input image and the corresponding estimation. (a) Input image. (b) Output image. (c) Depth estimation. (d) Shading component $I(x)$. (e) Transmission $t(x)$. (f) Extrapolated transmission.

2.3.2 Advantage and Disadvantage

This approach is physics-based and can produce a natural haze-free image together with a good depth map by solving a non-linear inverse problem and deriving the estimation for the noise present in the input. Moreover, large errors are eliminated by using the statistical extrapolation. However, this approach may fail in the case of insufficient signal-to-noise ratio or the absence of multiplicative variation in significant portions of the image. Because the statistics depend on color information, in the images with colorless (i.e., gray scale images) and prone to noise (i.e., dense haze images), the approach is invalid and difficult to handle, respectively.



2.4 Dark Channel Prior-Based

The most representative dark channel based method is named “Single Image Haze Removal Using Dark Channel Prior” which had been proposed by He et al. [3] in 2009. It is based on the statistics of haze-free outdoor images and the concept of dark channel prior. By using these dark pixels, an accurate estimation for the transmission can be obtained. Then, a high quality haze-free image and a good depth map can be obtained by combining a haze imaging model with a soft matting interpolation method [3].

2.4.1 Basic Concept of Dark Channel Prior-Based Method

The method in [3] is based on the model (1.1) and dark channel prior. They find that, in most of the non-sky local patches, some pixels (called “dark pixels”) have very low intensity in at least one color channel (RGB). For an image J , it is defined as follows

$$J^{dark}(x) = \min_{c \in \{r, g, b\}} \left(\min_{y \in \Omega(x)} (J^c(y)) \right) \quad (2.29)$$

where J^c is a color channel of J , and $\Omega(x)$ is a local patch centered at x . The observation say that if the haze-free outdoor image J except for sky region, the intensity of J^{dark} is low and tends to zero shown in Fig. 2.7. They regard J^{dark} as the dark channel of J , the above statistical observation or knowledge as the dark channel prior.



(a)

(b)



(a)

(b)

Fig. 2.7 Relationship between haze-free outdoor images and their corresponding dark channel. (a) Haze-free outdoor images. (b) Dark channel corresponding to (a).

The intensity of the dark channel is a rough approximation of the thickness of the haze. This property can be used to estimate the transmission and the atmospheric light. Therefore, they pick the top 0.1% brightest pixels in the dark channel as the atmospheric light A rather than the pixel with highest intensity, which may be a white car or a white building in images. After that, they assume that the transmission in a local patch $\Omega(x)$ is constant. Owing to the known atmospheric light A and the assumption of the transmission in a local patch, they take the min operation in the local patch among three color channels on (1.1) to obtain

$$\min_c \left(\min_{y \in \Omega(x)} \left(\frac{I^c(y)}{A^c} \right) \right) = \tilde{t}(x) \min_c \left(\min_{y \in \Omega(x)} \left(\frac{J^c(y)}{A^c} \right) \right) + (1 - \tilde{t}(x)) \quad (2.30)$$

Based on the dark channel prior, the dark channel J^{dark} of the haze-free radiance J tends to be zero and A^c is always positive, this lead to

$$\min_c \left(\min_{y \in \Omega(x)} \left(\frac{J^c(y)}{A^c} \right) \right) = 0 \quad (2.31)$$

According to (2.31), the transmission \tilde{t} can be estimated from (2.30) as

$$\tilde{t}(x) = 1 - \min_c \left(\min_{y \in \Omega(x)} \left(\frac{I^c(y)}{A^c} \right) \right) \quad (2.32)$$

Because the sky is the image with infinite-distance and usually has similar color to the atmospheric light, the transmission of the sky is almost equal to zero. For these sakes, (2.32) is useful for both sky and non-sky regions. But in realistic situation, some particles still exist within the atmosphere in clear days and these particles are important and necessary for perceiving depth. In order to make the object images in high-distance look more natural, a very few haze (particles) are reserved randomly by introducing a constant value $\omega(0 < \omega \leq 1)$ to (2.32) as

$$\tilde{t}(x) = 1 - \omega \min_c \left(\min_{y \in \Omega(x)} \left(\frac{I^c(y)}{A^c} \right) \right) \quad (2.33)$$

It is reasonably good but contains some block effects because the transmission is not always constant in a patch. Fig. 2.8(b) shows the estimated transmission map and the block effects from an input haze image (Fig. 2.8(a)). In order to reduce this problem, they apply a soft matting algorithm [29] to refine the transmission $t(x)$. Then, the coarse $\tilde{t}(x)$ and the refined transmission $t(x)$ are rewritten in their vector form as \tilde{t} and t .

They minimized the following cost function

$$E(t) = t^T L t + \lambda (t - \tilde{t})^T (t - \tilde{t}) \quad (2.34)$$

where L is the Matting Laplacian matrix proposed by Levin [29], and λ is regularization parameter. The first term is the smooth term and the second term is the data term. Then, the optimal can be obtained by solving the following sparse linear system

$$(L + \lambda U)t = \lambda \tilde{t} \quad (2.35)$$

where U is an identity matrix of the same size as L , and λ is set by a small value. In Fig. 2.8(c), the refined transmission maps manage to capture the sharp edge discontinuities and outline the profile of the objects. Besides, the transmission map is smooth in where no depth edge exists. After acquiring all the parameters in (1.1), the scene radiance J can be acquired. However, the direct attenuation term $J(x)t(x)$ is very close to zero when the transmission $t(x)$ is close to zero. Consequently, they restrict the transmission $t(x)$ to a lower bound t_0 , which means that a small amount of the haze is preserved in very dense haze regions. The final scene radiance $J(x)$ is recovered by

$$J(x) = \frac{I(x) - A}{\max(t(x), t_0)} + A \quad (2.36)$$

Fig. 2.8(d) and Fig. 2.9(b) display the haze removal results applied from He et al.'s algorithm [3]. The flow chart of the dark channel prior [3] is given in Fig. 2.10.

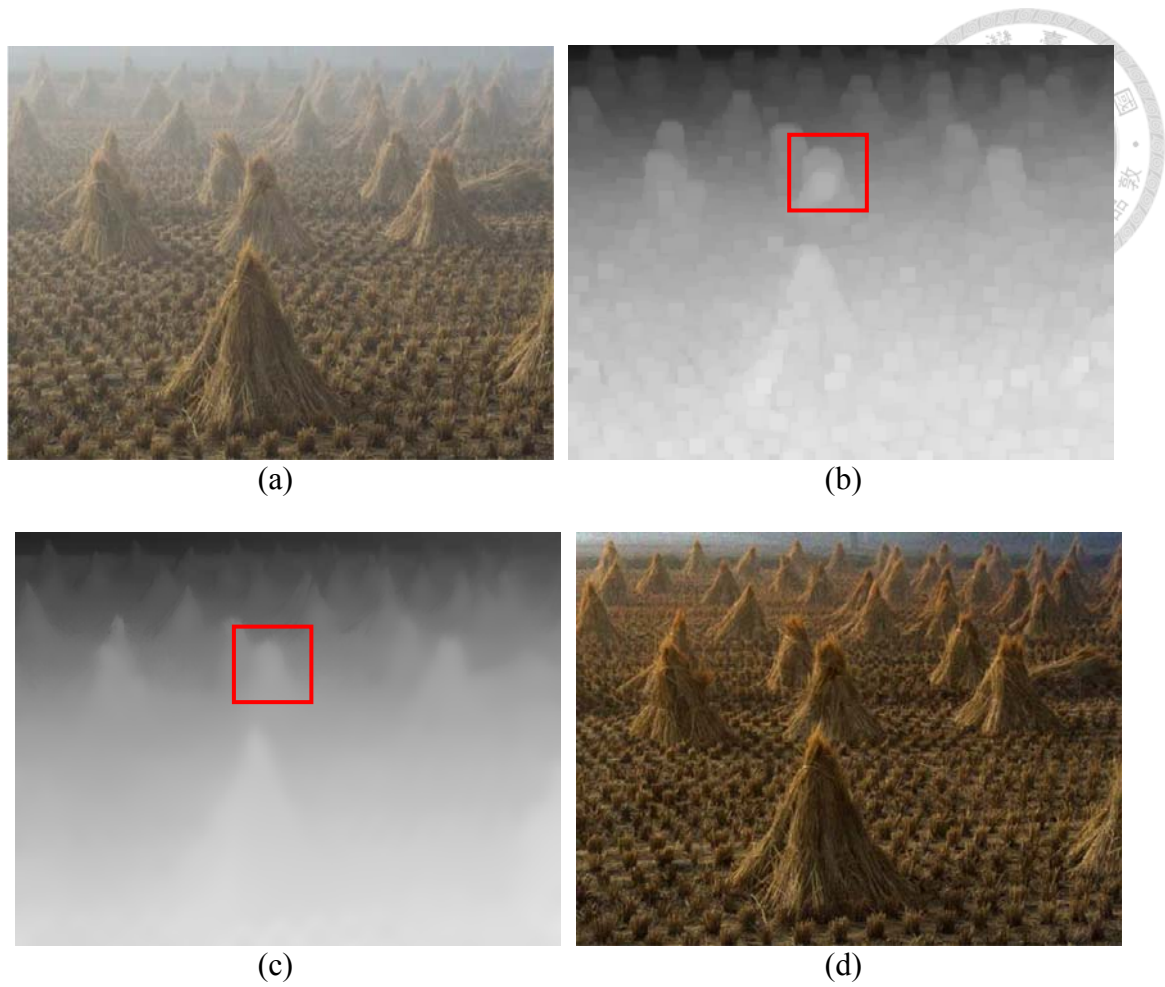


Fig. 2.8 Haze removal process. (a) Input haze image. (b) Estimated transmission map. (c) Refined transmission map after soft matting. (d) Final haze-free image.

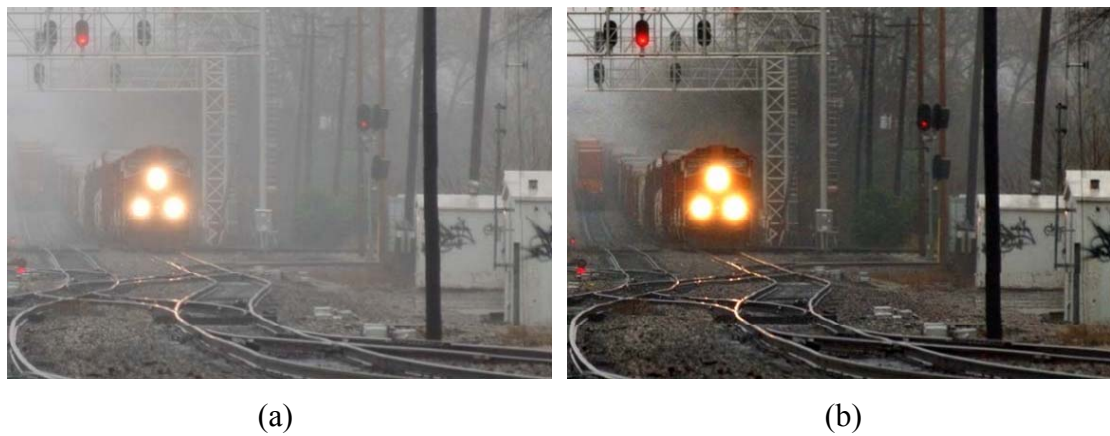


Fig. 2.9 Haze removal results. (a) Input haze images. (b) Final haze-free image.

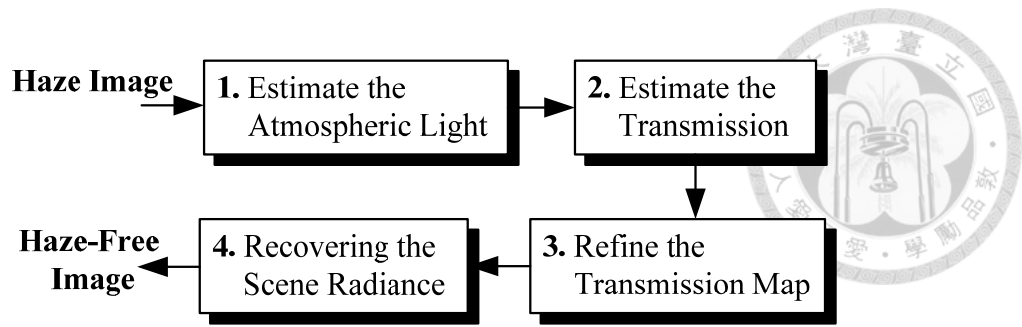


Fig. 2.10 Flow chart of the dark channel prior [3].

2.4.2 Advantage and Disadvantage

This approach is physically valid and is able to handle objects with long distance even in the heavy haze image. Besides, it is independent of significant variance for transmission and surface shading in the input image. It also produces an appealing result from a single image without any geometric information. However, the dark channel prior may be invalid when the image object has similar color to the airlight over a large local region without any shadow. This method may also fail in some extreme cases such as nighttime haze. The result contains few halo artifacts because of the inaccurate estimation of airlight and the patch operation. Moreover, the approach is time-consuming because of a soft matting complex computation for refining the transmission map.



Chapter 3 Proposed Method of Single Image Dehazing



3.1 Introduction

The conventional approaches work well for most conditions of daytime haze images, but they are limited for nighttime case because of their poor image quality. Thus, we are motivated to investigate a robust haze image removal algorithm, especially in the nighttime case.

There are several properties and important effects associated with viewing real nighttime scenes [30], [31]. Generally, there are the following properties in nighttime scene: low overall contrast, low overall brightness, loss of acuity, loss-of-detail, visible noise, and "blue shift" airlight color. Particularly, there are three critical issues considered for nighttime dehazing. First, the color of the airlight dominates the performance of dehazing results and the color naturalness. Second, light sources in the nighttime scenes have an influence on the degree of exposure. Last, the insufficient brightness and poor quality cause the loss of image information for dehazing. It implies that the nighttime image dehazing techniques are hard to realize.

In [31], the computation of Dark Channel Prior (DCP) [3] is based on the assumption of the "grayish" airlight color. The method in [32] based on color transfer [33] used to transform the airlight color from a "blue shift" to a "grayish". After the initial nighttime haze images are color-transformed, the final haze-free images are output by applying the refined dark channel prior method and bilateral filter in local contrast correction (BFLCC) [34]. This method can be used to get the nighttime

haze-free images, but it bring the block and contouring effects.

We use the night enhancement on the nighttime haze for the input image I . The output image I' is produced from the initial nighttime haze images I by the enhanced-processing, and will be operated by the proposed daytime dehaze method. Unlike the conventional methods, the proposed method can be avoid by the block and contouring effects. Moreover, the proposed method can be used to reduce the complexity that increases from refining the transmission in [3], and can be operated over different dense of haze images captured in the daytime, even one of the extreme cases: nighttime haze with the light sources. Experimental results also show that the high quality dehazed images can be produced by the proposed method, even in the nighttime.

3.2 Proposed Method for Daytime Haze

The flow chart of the proposed dehazing technique in daytime is shown in Fig. 3.1. The post-processing is added for increasing the robustness of the proposed method.

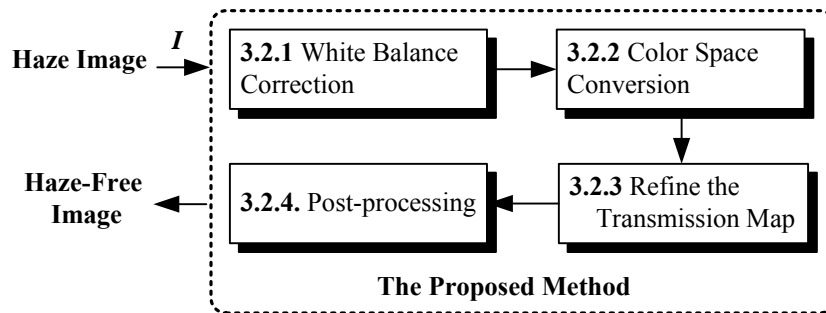
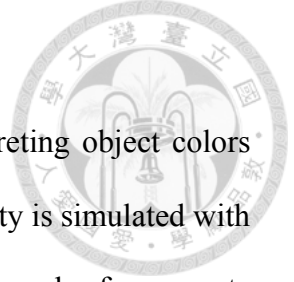


Fig. 3.1 Flow chart of the proposed dehazing technique in daytime.



3.2.1 White Balance Correction

The human visual system (HVS) is capable of reliably interpreting object colors with surrounding illumination. In the photographic process, this ability is simulated with the white balance function which helps identify the reference of white color for accurate color production. Without a proper white balance, photos taken by cameras may show undesirable color cast. In order to ensure the natural color reproduction of scenes, auto white balance of cameras generally relies on the estimation of color temperature. Color temperature refers to the color appearance of the light that comes from a light source. For example, higher color temperature implies a colder (more blue) light while lower color temperature implies a warmer (more red) light [35]. When objects are in a hazy scene, there is higher color temperature which may cause unrealistic color casts. In order to correct the color, we apply white balance correction prior to dehazing by calibrating the fog color to pure white.

When we assume that the input image $I(x)$ is normalized between 0 and 1, the procedure of white balance implies that the intensity of the atmospheric light A can be set to pure white, and the rest part of image can be normalized as follow:

$$\tilde{I}^c(x) = W \cdot I^c(x) \quad (3.1)$$

where $\tilde{I}^c(x)$ and $I^c(x)$ represent the white balance corrected image and the input hazy image, respectively, $c \in \{R, G, B\}$ is color channel index.

$W^c = \text{diag}(W^r, W^g, W^b)$ is the scale matrix, and each channel of W is defined as:

$$W^c = \frac{A^c}{\text{mean}(A^c)} \quad (3.2)$$

where the atmospheric light A that we choose from the top 0.05% brightest and the top 25% height pixels in the dark channel, is defined as (2.29). As shown in Fig. 3.2, the

input hazy image looks bluish, apparently, the image after white balance correction looks more natural and the atmospheric light is corrected to white. The visibility of the dehazed image obtained by the white balance correction is also enhanced significantly.

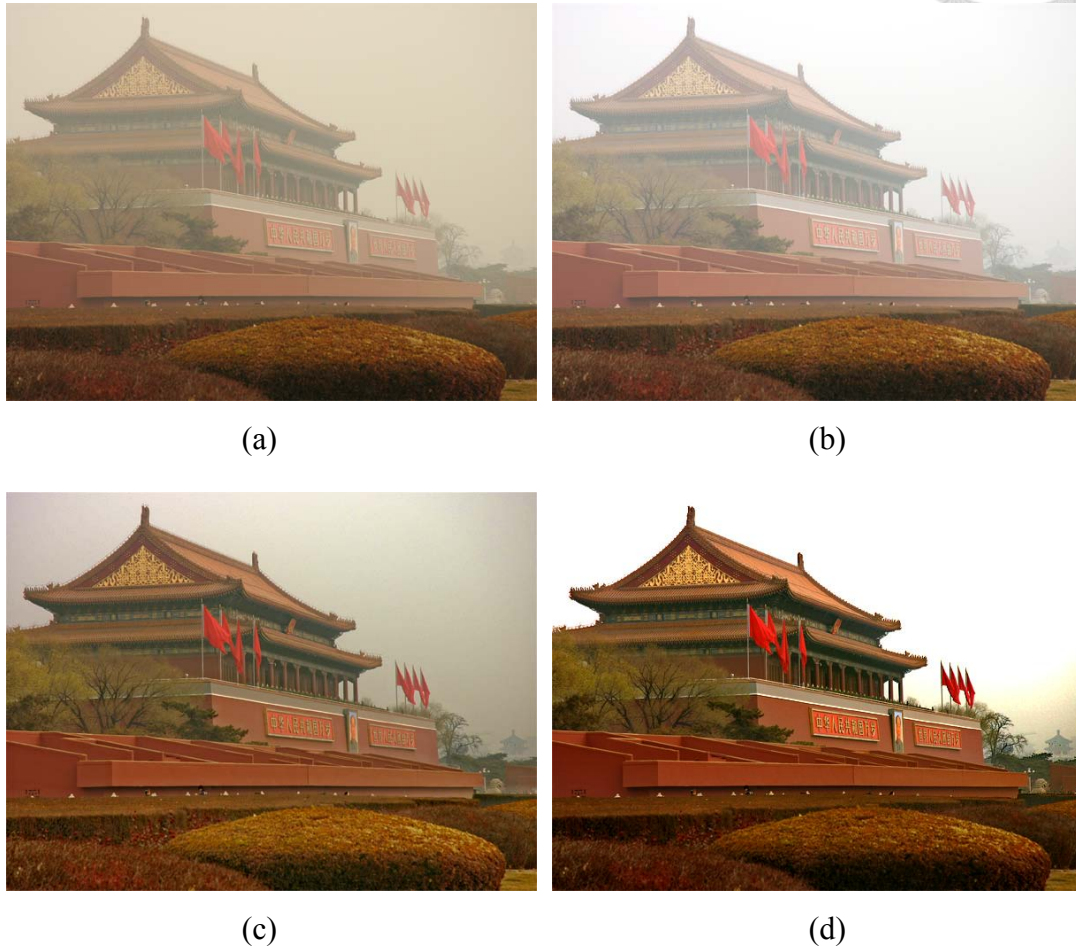


Fig. 3.2 Illustration of the white balance correction. (a) Input image. (b) White balance corrected image. (c) Dehazed without the white balance correction. (d) Dehazed after the white balance correction.

3.2.2 Color Space Conversion

The *HSI* (hue, saturation, intensity) and *HSV* (hue, saturation, value) color spaces were developed to be more “intuitive” in manipulating color and were designed to approximate the way that humans perceive and interpret color. When the *HSI* and *HSV*

color spaces were developed, they had to be manually specified. However, they are rarely used nowadays; we rarely used now that users can select colors visually or specify Pantone colors. These color spaces are discussed for “historic” interest. *HLS* (hue, lightness, saturation) is similar to *HSI*, and the term lightness is used rather than intensity. The *HSI* color space is based on the cylindrical coordinate system, and the conversion form *RGB* color space to *HSI* color space is defined as:

$$\left\{ \begin{array}{l} H = \begin{cases} \theta & \text{if } B \leq G \\ 360 - \theta & \text{if } B > G \end{cases} \\ \text{with } \theta = \cos^{-1} \left\{ \frac{\frac{1}{2}[(R-G) + (R-B)]}{[(R-G)^2 + (R-B)(G-B)]^{1/2}} \right\} \\ S = 1 - \frac{3}{(R+G+B)} [\min(R, G, B)] \\ I = \frac{1}{3}(R+G+B) \end{array} \right. \quad (3.3)$$

where I and S are in the range of $[0, 1]$ and H is the range of $[0, 360]$.

In order to convert color from the *HSI* color space to *RGB* color space, three cases of the H range must be considered *RG* section: $0^\circ \leq H < 120^\circ$

$$\left\{ \begin{array}{l} B = I(1-S) \\ R = I \left[1 + \frac{S \cos H}{\cos(60^\circ - H)} \right] \\ G = 3I - (R+B) \end{array} \right. \quad (3.4)$$

GB section: $120^\circ \leq H < 240^\circ$

$$\begin{array}{l} H = H - 120^\circ \\ \left\{ \begin{array}{l} R = I(1-S) \\ G = I \left[1 + \frac{S \cos H}{\cos(60^\circ - H)} \right] \\ B = 3I - (R+G) \end{array} \right. \end{array} \quad (3.5)$$

BR section: $240^\circ \leq H < 360^\circ$



$$\begin{cases}
 H = H - 240^\circ \\
 G = I(1 - S) \\
 B = I \left[1 + \frac{S \cos H}{\cos(60^\circ - H)} \right] \\
 R = 3I - (G + B)
 \end{cases} \quad (3.6)$$

Fig. 3.3 illustrates the double conic *HSI* color model. The top of the conic corresponds to $I = 1$, or white. The point at the base of the conic is black and here $I = 0$. Complementary colors are 180° opposite one another as measured by H , the angle around the vertical axis (I), with red at 0° (for consistency with the *HSV* model, we have changed from the Tektronix convention of blue at 0°). The value of S ranges from 0 on the vertical axis (I) to 1 on the surfaces of the conic. The grays all have $S = 0$, but maximum saturation of hues is at $S = 1$, $I = 0.5$. Table 3.1 lists the 75% amplitude, 100% saturated *HSI* color bars.

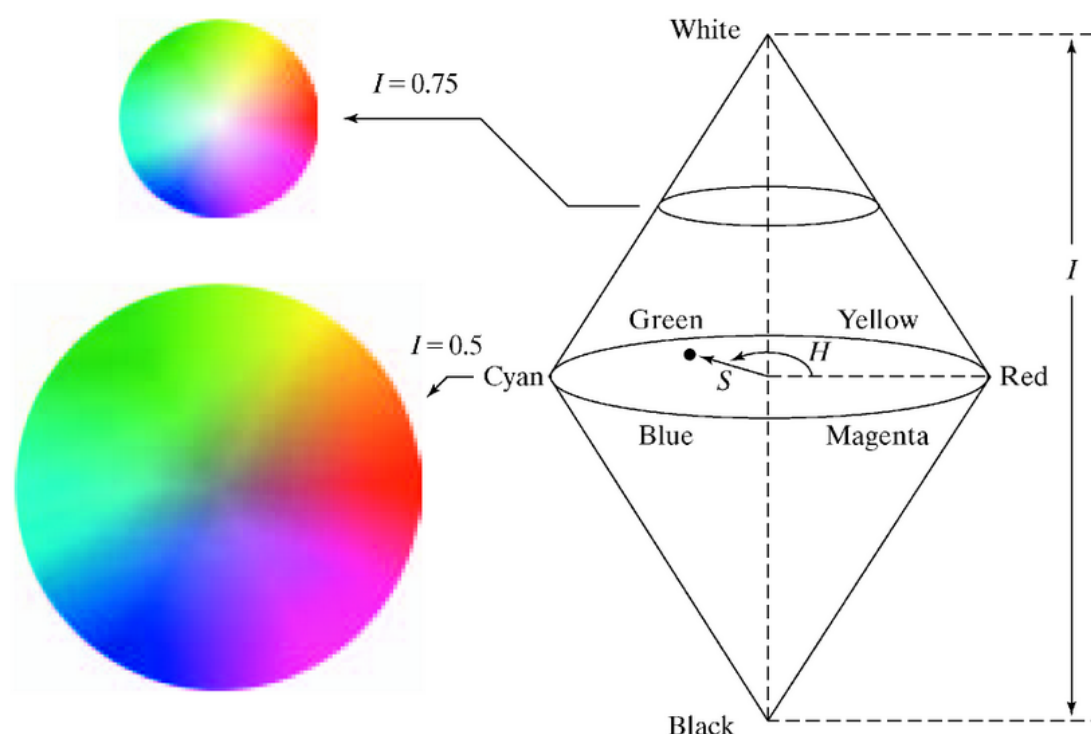


Fig. 3.3 *HSI* color model.

	Nominal Range	White	Yellow	Cyan	Green	Magenta	Red	Blue	Black
H	0° to 360°	–	60°	180°	120°	300°	0°	240°	–
S	0 to 1	0	1	1	1	1	1	1	0
I	0 to 1	0.75	0.375	0.375	0.375	0.375	0.375	0.375	0

Table 3.1 75% *HSI* Color Bars. For consistency with the *HSV* model, we have changed from the Tektronix convention of blue at 0°.

In order to remove the singular points in the *HSI* color space, we set $H \stackrel{\triangle}{=} 0$ and $S \stackrel{\triangle}{=} 1$ on the $R=G=B$ plane.

The haze image model in (1.1) is in the *RGB* color space. We map it onto the

HSI color space. Let H_I, S_I, I_I denote that the observed pixel values of the hazy image

which have been white balance corrected, and H_J, S_J, I_J denote that the scene

radiance of the haze-free image value in the *HSI* color space.

Using the haze image model (1.1) and the conversion (3.4) between *RGB* and *HSI* color space. We get the following equivalent equation:

$$\begin{cases} H_I(x) = H_J(x) \\ S_I(x) = t(x) \frac{I_J(x)}{I_I(x)} S_J(x) \\ I_I(x) = t(x) I_J(x) + (1-t(x)) A \end{cases} \quad (3.7)$$

When the global atmospheric light A is achromatic, i.e. the values of airlight A in the

three *RGB* colour channel are the same, the hue layer remains the same value after the

haze degradation. To restore a foggy image, saturation and intensity layer are needed to

be processed. Unlike *RGB* colour space, computation is reduced by (1/3) in *HSI* colour

space. For the saturation layer

$$\frac{t(x) I_J}{I_I} = \frac{t(x) I_J}{t(x) I_J + (1-t(x)) A} \leq 1 \quad (3.8)$$

So that $S_I \leq S_J$. Although, haze does not influence the hue of the image, it degrades the saturation and intensity layers of the original hazy image, and results in low saturation and contrast. The fact that haze artifact reduces the saturation level coincides with our intuitive understanding. When pure colors (full-saturated) are mixed with achromatic ones, the saturation decreases. For the intensity layer I_I , it follows the standard haze model.

3.2.3 Refined Transmission Coefficient Map

For acquiring higher quality haze-free images, the 1st to 3rd steps of the dark channel prior method [3], which is showed in Fig. 2.10, are modified in this sub-section. In order to mitigate some drawbacks of the block effect, contouring effect and the inaccurate estimation in the sky-region in (2.29), we replace the patch operation into the pixel-wise operation. Fig 3.4 shows the dehazing result under the block-based transmission maps and the pixel-based refined maps. We observe that the pixels-based maps effectively reduce blocking artifacts and preserve image details more accurately.



Fig. 3.4 Comparison of the dehazing result under two different cases of transmission map t . (a) Input hazy image. (b) Results for the block-based transmission map. (c) Results for the pixels-based transmission map.



The dark channel prior assumes that the minimum intensity in such pixel has a very low value, i.e. for these pixels, $\min(R, G, B) \leq \varepsilon$. We formalize this case for the dark channel J as

$$J^{dark}(x) = \min_{c \in \{r, g, b\}} \left(\min_{y \in pixel} (J^c(y)) \right) \quad (3.9)$$

where J^c is a color channel of J and J^{dark} is the dark channel of J . From (3.3), when the full-saturation assumption holds, the saturation value of one pixel is close to 1

$$S_J^{max}(x) \rightarrow 1 \quad (3.10)$$

In addition, all pixels from the dark channel are sorted initially in ascending order as J^{dark_order} by intensity values by our proposed method. Based on J^{dark_order} , choosing appropriate atmospheric light A is further investigated under two different cases. In the former case, when the input haze image is captured in the daytime, we choose 95% intensity of the pixel values (i.e., 95% value in J^{dark_order}) as the atmospheric light value to prevent choosing some wrong high-light objects such as white cars and buildings.

When we talk about the visual pleasure of color images, it is often with reference to vivid colors. [36] discussed the necessity of producing vivid colors for higher visual pleasure. Images with vivid colors are assumed to be pleasant because vivid colors are salient for the human visual system. Thus in our proposed method, the haze-free image is assumed to be of vivid color. Considering the role of saturation from a perceptual point of view, it influences the level of purity and vividness of a color [37]. Thus, in the *HSI* color space, the saturation of vivid colors is close to 1. Fig. 3.5 shows an example of natural vivid image and three channels of it.

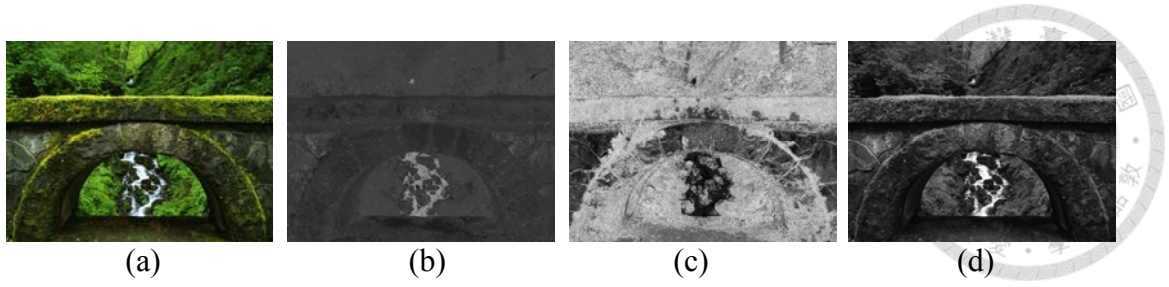


Fig. 3.5 (a) *RGB* image. (b) Hue image. (c) Saturation image. (d) Intensity image.

To restate our assumption in a more formal way

$$\max_{x \in \text{pixel}} S_J(x) \in \{0, 1 - \varepsilon\} \quad (3.11)$$

In the haze-free image, most chromatic pixels are fully saturated. Here, we set ε to 0.001~0.01 for system numerical stability. We solve the transmission coefficient map t (i.e., 2nd step in Fig. 2.10) from (3.5)

$$t(x) = 1 - \left(I_I(x) - \frac{S_I(x)}{S_J(x)} I_I(x) \right) / A \quad (3.12)$$

Based on (3.10), we can assume the colors of haze-free images are vivid. For each pixels

$$\max_{x \in \text{pixel}} S_J(x) = 1 - \varepsilon \quad (3.13)$$

where ε is a small number to avoid over-saturation of the recovered colors. From equation (3.13), we can further modify the transmission coefficient map by

$$t(x) = 1 - \left(I_I(x) - \frac{S_I(x)}{1 - \varepsilon} I_I(x) \right) / A \quad (3.14)$$

For decreasing the complexity of the soft matting in the 3rd step of Fig. 2.10 and prevent the block artifact, the guided filter [55] can be employed to smooth the transmission while capturing the sharp edge discontinuities and outline the profile of objects (e.g. [38], [55]). Specifically, guided filter is an efficient linear-time algorithm while providing the exact solutions with the size-dependent complexity. Based on this, the refined transmission $t'(x)$ can be identified.

$$t'(x) = \frac{1}{|W|} \sum_{k: x \in W_k} (a_k t(x) + b_k) \quad (3.15)$$

where $|W|$ is the number of the pixels in W_k , W_k is a window centered at the pixel k , and (a_k, b_k) are some linear coefficients. Particularly, (a_k, b_k) are the constant in W_k as

$$a_k = \frac{\frac{1}{|W|} \sum_{x \in W_k} t(x) p(x) - \mu_k \left(\frac{1}{|W|} \sum_{x \in W_k} p(x) \right)}{\sigma_k^2 + \varepsilon} \quad (3.16)$$

and

$$b_k = \left(\frac{1}{|W|} \sum_{x \in W_k} p(x) \right) - a_k \mu_k \quad (3.17)$$

where μ_k and σ_k^2 are the mean and the variance of the transmission t , ε is a regularization parameter while preventing a_k from being too large, and $p(x)$ is the filtering transmission map by bilateral filter [38]. By using the guided joint bilateral filter, the refined transmission $t'(x)$ can be identified. Finally, the estimated and improved scene radiance $J'(x)$ can be acquired as

$$J'(x) = \frac{I(x) - A}{\max(t'(x), t_0)} + A \quad (3.18)$$

We perform the proposed dehazing scheme on several hazy images. Experimental results are shown in Fig. 3.6 The vivid colors have been successfully recovered in the output images.

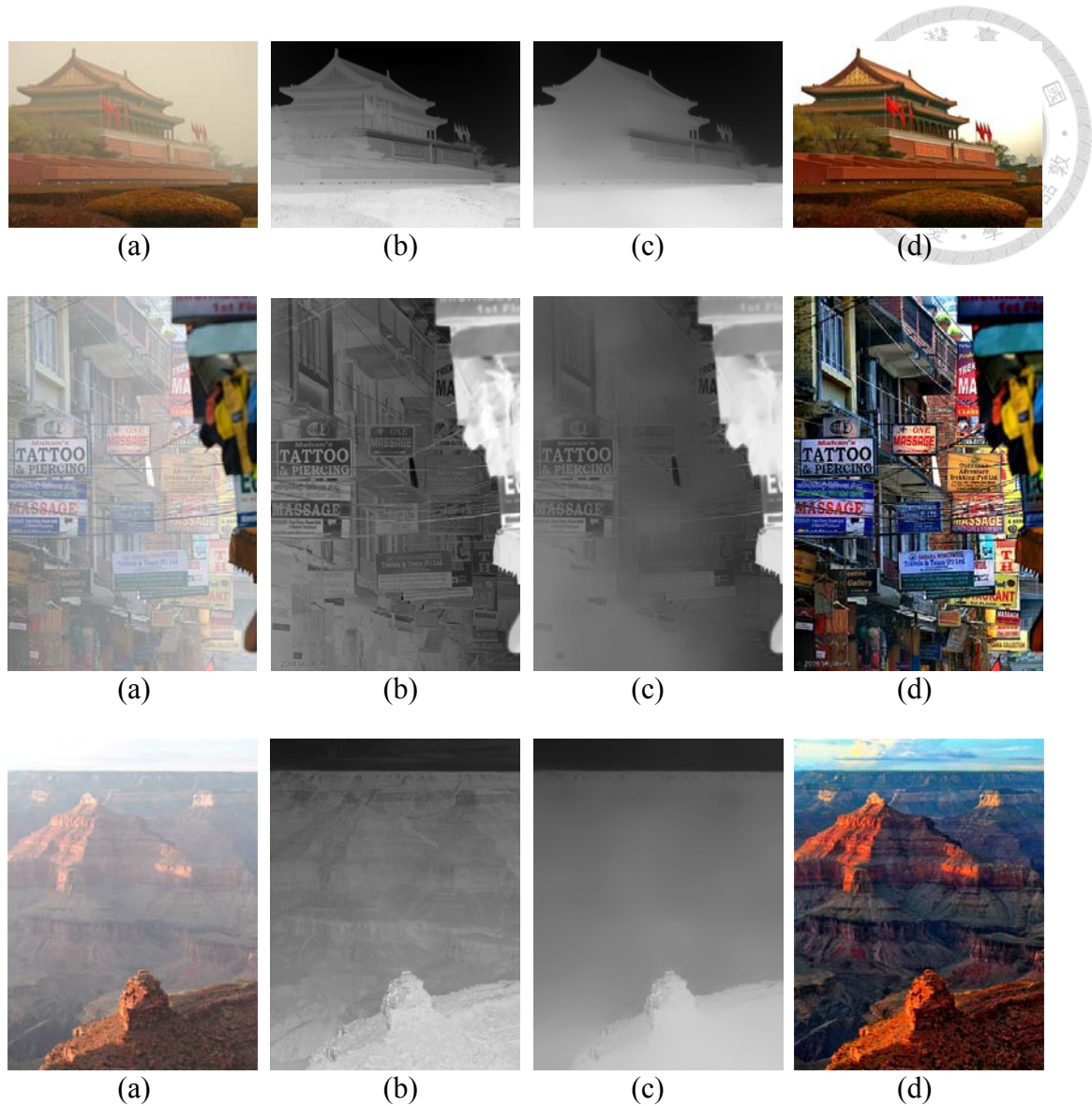


Fig. 3.6 Insufficient brightness and non-uniform distributed haze images. (a) Input hazy image. (b) Estimated transmission. (c) Refined transmission. (d) Final dehazing image.

3.2.4 Post-Processing

To further enhance the result for the proposed method, we integrate the post-processing mechanism in our system for some haze images with exposure adjustment. Due to the under-exposure for foggy senses in the imaging process, dehazed images generally appear to be dim. Here, we propose a method to enhance the dehazed

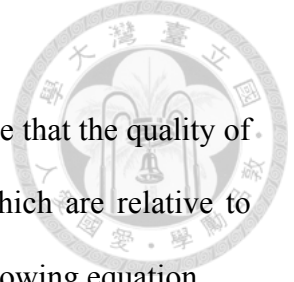


image by utilizing the ambience illumination image.

In order to obtain the accurate luminance of the light, we assume that the quality of an image is determined by two factors, details and naturalness, which are relative to reflex lightness image and ambience illumination image with the following equation

$$I^c(x) = RL^c(x) + AL^c(x) \quad (3.19)$$

$$RL^c(x) = (1 - \alpha) \cdot I^c(x) \quad (3.20)$$

$$AL^c(x) = \alpha \cdot I^c(x) \quad (3.21)$$

where $I^c(x)$ is the color channel c of the hazy image, $AL^c(x)$ is the associated ambience illumination image, $RL^c(x)$ is the reflex lightness image, and α is a weighting factor. In general cases, weighting factor α satisfies the following formulas: A bright area in the ambience illumination image remains brighter than a dark area, and after the ambience illumination is removed, the left part keeps the original sequence of the brightness. Hence, α is defined as:

$$\alpha = \frac{1}{2} \cdot \frac{I(x)}{I_{\max}} \quad (3.22)$$

where $I(x)$ is the observed hazy image brightness and I_{\max} is the maximum pixel value of the hazy image $I(x)$.

As ambience illumination image is always brighter than reflex lightness image, we modify the brightness of scene radiance to the level of ambience illumination image which is shown as follows,

$$J''(x) = J'(x)^{\frac{\log(\overline{AL})}{\log(\overline{RL})}} \quad (3.23)$$

where $J''(x)$ denotes the adjusted image and $J'(x)$ is the improved scene radiance

obtained in section 3.2.3, \overline{AL} and \overline{RL} denote the mean of the associated ambience illumination and the associated reflex lightness, respectively [42]. Fig 3.7 shows the results of our proposed method and the results after the exposure adjustment.

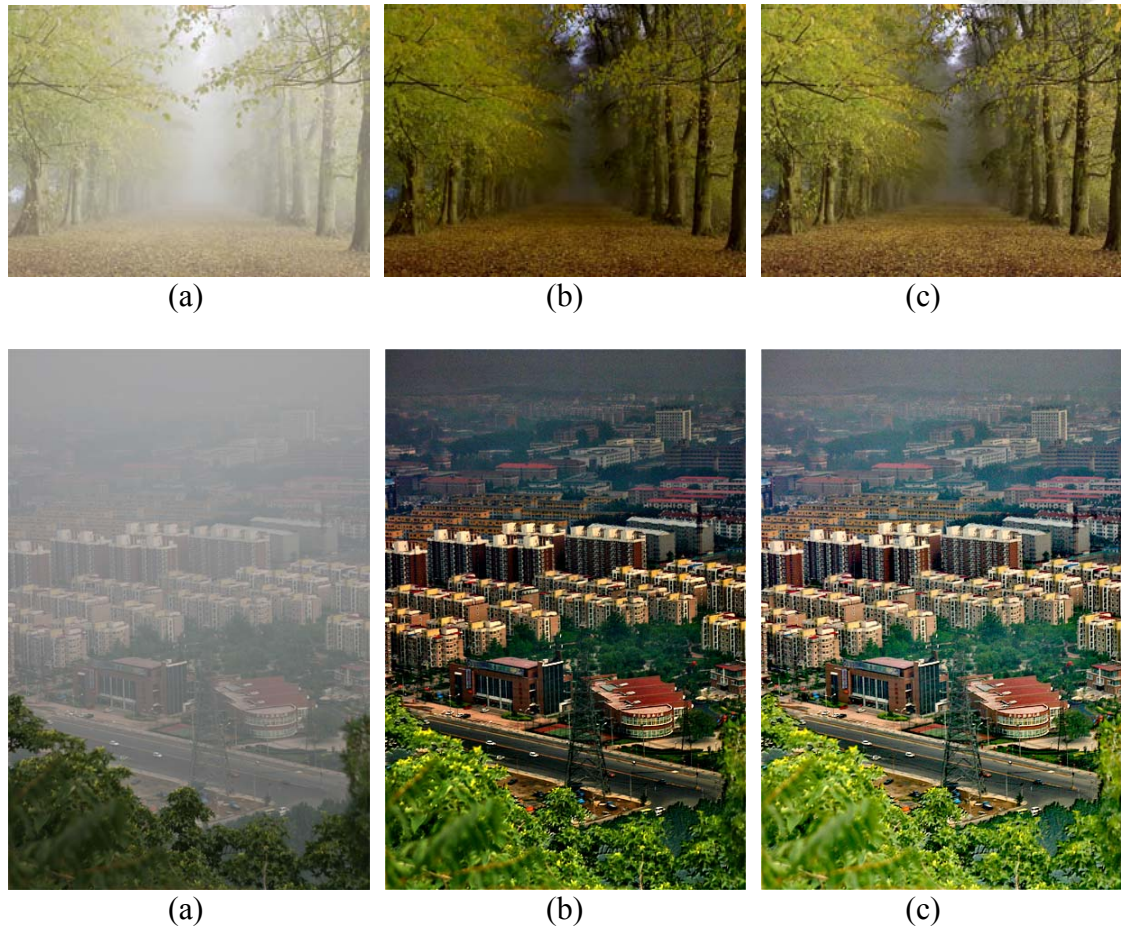


Fig. 3.7 Comparisons of results by the proposed method in the images. (a) Input haze image. (b) Final dehazing image (improved scene radiance). (c) Final dehazing image by post-processing (adjusted image).

3.3 Extended Proposed Method for Night Fog

In [31], it is assumed that the computation of DCP is based on the "grayish" airlight color. Thus, the color and the distribution of airlight are dominated the quality of dehazing results. However, there are the following inherent properties in the nighttime

haze scene: low overall contrast, low overall brightness and “color shift” of the airlight, etc.... Consequently, we use the night enhancement on the nighttime haze for the input image I , which enhance the nighttime image. After the enhancement processing on the initial nighttime haze images (I), the output image (I') is progressively operated the proposed method (i.e., mentioned in sub-section 3.2). After those procedures, the result image is processed by the proposed method to obtain the final appealing nighttime haze free image. The flow chart of the proposed method is showed in Fig. 3.8.

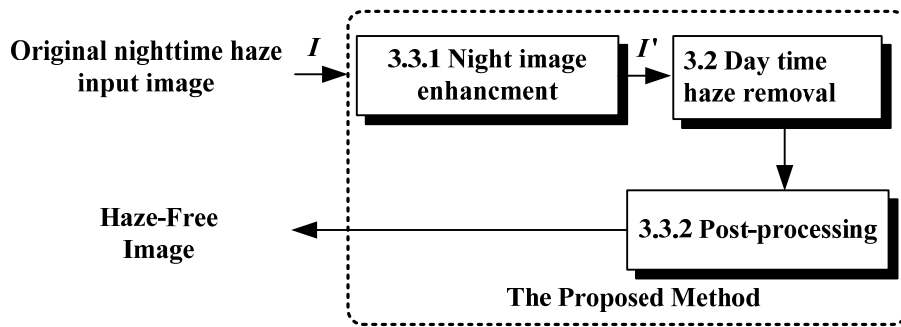
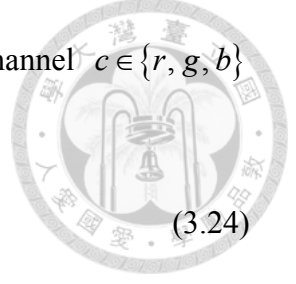


Fig. 3.8 Flow chart of the proposed method for night fog.

3.3.1 Night Image Enhancement

In order to enhance the nighttime image, a fast and effective technique for enhancement of low lighting video has been proposed by Dong at al. [43]. Dong at al. observed that a pixel-wise inversion of a night video has quite similar appearance with the video acquired at foggy days. Dong at al. [43] proposed the statistical similarity between the pixel-wise inversion of the night video and the foggy video, and claimed that it is conceivable to use haze removal algorithm to enhance the night video. The basic concept of our proposed method is for enhancing the nighttime image, and then processing the daytime image (i.e., mentioned in sub-section 3.2). The flow chart of the proposed nighttime enhancement method is showed in Fig. 3.9.



For a color input image $I(x)$, the pixel-wise inversion of its channel $c \in \{r, g, b\}$ can be calculated as

$$I_{inv}^c(x) = 255 - I^c(x) \quad (3.24)$$

Based on the above observation, we can reformulated the haze image model as

$$I_{inv}(x) = J_{inv} \cdot t(x) + A \cdot (1 - t(x)) \quad (3.25)$$

where J_{inv} is the scene radiance, t is the medium transmission, and A is the global atmospheric light. We choose the minimum intensity of the pixel values (i.e., minimum value in $I_{inv}^c(x)$) as the atmospheric light value to avoid it from over-exposure under the light sources of the night fog. When we know A and t , we can obtain the J_{inv} from I_{inv} as follows

$$J_{inv}(x) = \frac{I_{inv}(x) - A}{t(x)} + A \quad (3.26)$$

Once obtaining J_{inv} , we perform the inversion operation on it to get the final enhancement image

$$J = 255 - J_{inv} \quad (3.27)$$

From (3.28), we only need to estimate the transmission coefficient map. In general case, we assume that the pixels on the same subject should have similar depths. If local detail of the transmission map $t(x)$ is close to the input image, it will cause the restored image loss details more easily. Hence, we refine the dark channel prior (DCP). We estimate the coarse dark channel map (CDCM) as

$$\tilde{I}_{dark}(x) = \min_{c \in \{r, g, b\}} \frac{I_{inv}^c(x)}{A^c} \quad (3.28)$$

According to the DCP [3], we can get a constraint $0 \leq I_{dark}(x) \leq \tilde{I}_{dark}(x)$, where

$I_{dark}(x)$ is the fined DCM (FDCM). For the aim of the smoothing the CDCM, we process it by using the median filter

$$I_{med}(x) = Med_S(\tilde{I}_{dark}(x)) \quad (3.29)$$

where S is the scale of the median filter. To make $t(x)$ locally smooth while maintaining the edges, we need wipe off the details in $I_{med}(x)$. We use local standard deviation to estimate the local details. Moreover, the median filter can enhance the local details. It can be expressed as

$$I_{detail}(x) = Med_S(|I_{med}(x) - \tilde{I}_{dark}(x)|) \quad (3.30)$$

Then, we can removal local details from $I_{med}(x)$ by using $I_{smooth}(x) = I_{med}(x) - I_{detail}(x)$. Finally, we can get the FDCM as follows

$$I_{dark}(x) = \begin{cases} \mu \tilde{I}_{dark}(x) & \text{if } \mu \tilde{I}_{dark}(x) < I_{smooth}(x) \\ I_{smooth}(x) & \text{otherwise} \end{cases} \quad (3.31)$$

where μ is a constant parameter that controls the strength of the constraints. And then, we can calculate the transmission with the FDCM as DCP using

$$t(x) = 1 - \omega \cdot I_{dark}(x) \quad (3.32)$$

where ω is a parameter to adjust the value of $t(x)$. Fig 3.10 shows the result of the proposed method for night image enhancement.

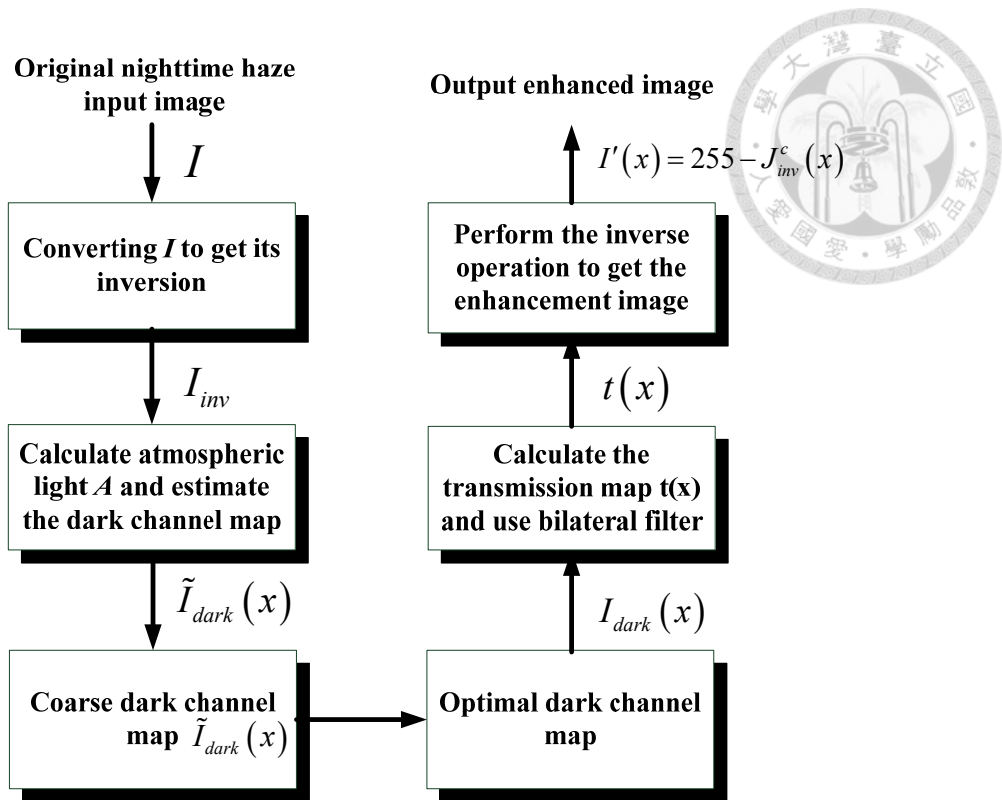


Fig. 3.9 Flow chart of the proposed nighttime enhancement method.

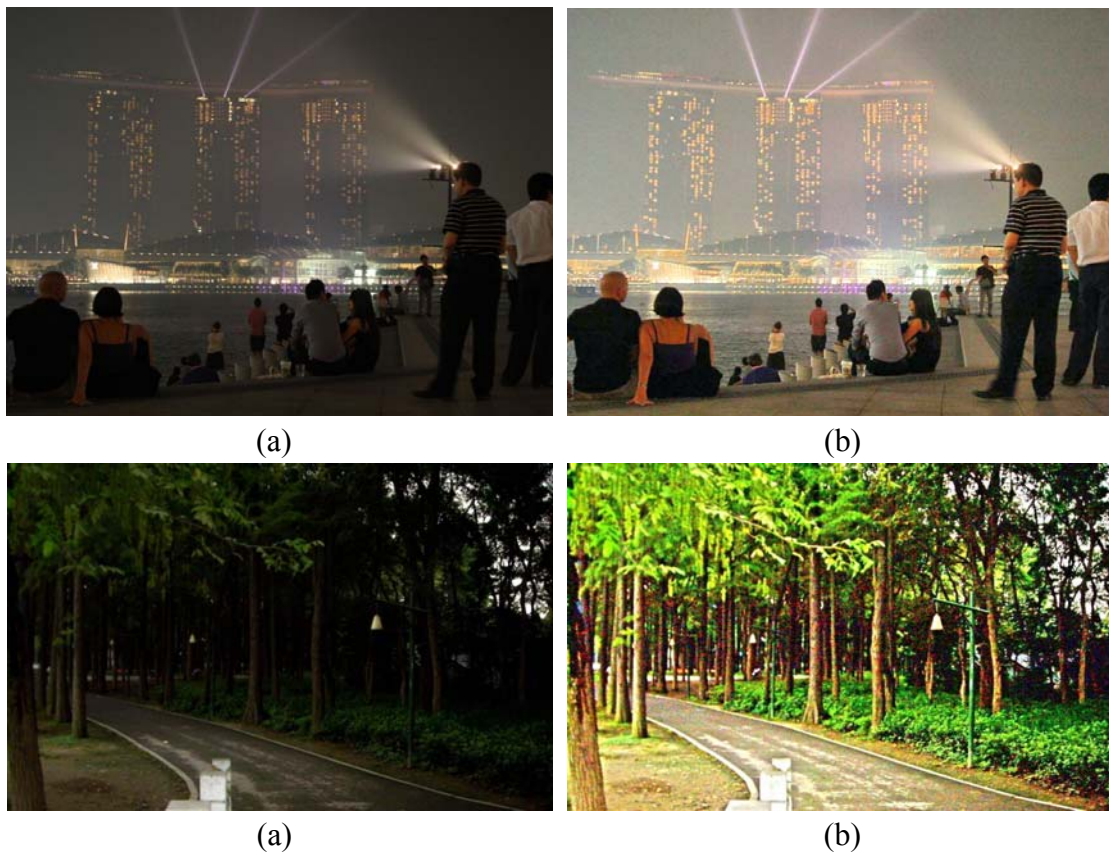


Fig. 3.10 Insufficient brightness images. (a) Input image. (b) Final enhanced image.

3.3.2 Post-Processing

To further enhance the robustness for the proposed nighttime haze-removal method, we integrate the post-processing mechanism in our system for some haze images with non-uniform distribution and insufficient brightness. Thus, the bilateral filter in local contrast correction (BFLCC) [34] is applied to perform the post-processing. The BFLCC method suits for handling the case that the sky is not the main component of the haze image. Note that the post processing approaches can remove the haze clearly.

The BFLCC method [34] is the technique to improve gamma correction. This method replaces an inverted Gaussian low-pass filtered into an inverted low-pass version of the intensity, filtered with a bilateral filter. The algorithm is a local exponential correction, applied to the intensity, as follows

$$O(x, y) = 255 \left[\frac{J'(x, y)}{255} \right]^{\alpha \left(128 - \frac{BF_{mask}(x, y)}{128} \right)}. \quad (3.33)$$

Here, x and y respectively denote the pixel's with vertical and horizontal indices, O is the output image, α is a parameter depending on the image properties and BF_{mask} . BF_{mask} is defined as $(2K + 1) \times (2K + 1)$ window size. The window size is given by the bifiltered image of the inverse version of the input

$$J'_{inv}(x, y) = 255 - J'(x, y). \quad (3.34)$$

Thus, BF_{mask} can be expressed as [34]

$$\begin{aligned} BF_{mask}(x, y) = & \frac{1}{k(x, y)} \sum_{p=x-K}^{x+K} \sum_{q=y-K}^{y+K} J'_{inv}(p, q) \\ & \times \exp \left\{ -\frac{1}{2\sigma_1^2} [(x-p)^2 + (y-q)^2] \right\} \\ & \times \exp \left\{ -\frac{1}{2\sigma_2^2} [(J'_{inv}(x, y) - J'_{inv}(p, q))]^2 \right\} \end{aligned} \quad (3.35)$$

where σ_1 and σ_2 are the standard deviations of the Gaussian function in the space and

intensity domains, and $k(x,y)$ is the normalization factor given by

$$k(x,y) = \sum_{p=x-K}^{x+K} \sum_{q=y-K}^{y+K} \exp\left\{-\frac{1}{2\sigma_1^2}[(x-p)^2 + (y-q)^2]\right\} \times \exp\left\{-\frac{1}{2\sigma_2^2}[(J'_{inv}(x,y) - J'_{inv}(p,q))]^2\right\}. \quad (3.36)$$



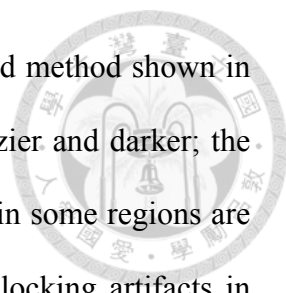
Fig. 3.11(c) shows the final dehazing images from input haze images by applying the proposed nighttime dehazed method and BFLCC post-processing.



Fig. 3.11 Insufficient brightness and non-uniform distributed haze compare with BFLCC post-processing. (a) The input nighttime hazy image. (b) Final dehazing image. (c) Final dehazing image with BFLCC post-processing.

3.4 Experimental Results

For comparing the experimental results, the source of the haze images are from [3], and some other haze images are captured in the daytime and nighttime. The experiment is separated into 3 cases: *Case 1*: the input image is captured in the daytime. *Case 2*: the input hazed image which is captured in the nighttime with insufficient brightness and various airlight color. *Case 3*: extended the proposed daytime method for underwater.

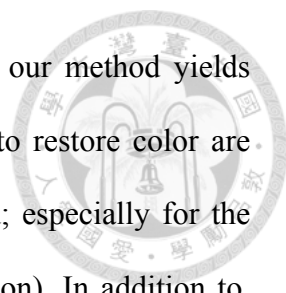


In *Case 1*, the input image is dehazed by applying the proposed method shown in Fig. 3.12. As shown in Fig 3.12 the results of He et al. [3] are fuzzier and darker; the results of Pei et al. [39] would not have such appearance but hazes in some regions are not removed completely; the result of Kim et al. [44] has some blocking artifacts in some region (e.g. near the boundary of the leaf.); the results of Nishino et al. [45] cause the hue change and over-saturation colors Besides, the color of the image is unnatural. We can acquire clearer and brighter dehazed images and preserve the fine transitions in the hazy regions by the proposed method.

As shown in Fig 3.13 the results of He et al. [3], He et al. [40] with multiple scattering model, and C. O. Ancuti et al.[41] are fuzzier and darker; the results of Pei et al. [39] would not have such appearance but cause the halo artifact around the headlights. The proposed method can acquire clearer and brighter dehazed images and preserve the fine transitions in the hazy regions without introducing displeasing artifacts.

As shown in Fig 3.14 the results of Tan et al. [3] are over-saturated, and the whole restored image looks unrealistic since their method is not physically based. Moreover, there are some halo artifacts in Tan's result, but there is not in our results. The image looks more realistic and its color is similar to the original one. Compare with Zhang et al. [46], there are some halo artifacts around the car and street sign in the result of Zhang et al. [46]. The color of the street sign in Nushimo et al's [45] result is not shown as its original one, but the shortcoming is solved by our method.

As shown in Fig 3.15, compare with Tan et al.'s method [1], our method is able to better preserve the fine transitions in the hazy regions without introducing displeasing artifacts. Moreover, the method of Tan et al. [1] produces results with over-saturated colors. The results of Fattal et al. [2] show some limitations with dense haze. Mainly due to the fact that the method is basically a static interpretation that requires variance



to estimate the depth map. Compare with He et al.'s method [3], our method yields similar results with the method of He et al. [3]. The results how to restore color are different between He et al.'s method [3] and our proposed method; especially for the distant regions (the sky and the clouds have a different hue rendition). In addition to, our method has the advantage of enhancing robustly such degraded images, decreasing the computationally expensive alpha matting procedure in the approach of He et al.'s method [3]. Compare with Nishino et al.'s method [45], it yields pleasing results, but may produce some artifacts in those regions considered to be at infinite depth (e.g. the skyline). Compare with Kim et al.'s method [44], our method is able to better preserve the fine transitions in the hazy regions without introducing displeasing artifacts. The method of Kim et al. [44] produces result with over-saturation colors. (e.g. the sky). Compare with C. O. Ancuti et al. [41], it is better to preserve the detail of the edge by our method.

In Case 2, the input image is dehazed by applying the proposed method shown in Fig. 3.8. The experimental results illustrate that the nighttime haze image using the proposed method has the reliable dehazing quality without inherent nighttime dehazing limitations. The experimental results are compared with He et al. [3] and Pei et al. [32]. As shown in Fig 3.16, the results of He et al. [3] are fuzzier and darker. Some of the regions may be incompletely recovered (e.g., for far region) and thus result in lower quality of the output haze removal image; the results of Pei et al. [32] cause the color change due to the procession of color transfer. In order to visualize how contrast is modified we employed the IQM metric [76] that was originally developed to evaluate tone mapping operators. This metric utilizes a model of the human visual system being sensitive to three types of structural changes: loss of visible contrast (green), amplification of invisible contrast (blue) and reversal of visible contrast (red). As a

general remark, compared with the other considered approaches, the most predominant structural change characteristic to our method is the amplification of the contrast (blue) and only very few locations exhibit reverse (red) and loss (green) of the contrast as shown in Fig 3.17. Fig 3.18 shows another nighttime dehazed results.

In Case 3, the input underwater image is dehazed by applying the proposed daytime dehazing method. Our proposed dehazing method can reduce the effect of haze caused by the scattering of light and is capable of providing a color correction through the airlight estimate. In such cases as shown in Fig. 3.19, even some enhancement could be obtained, the bluish appearance however still remains. Therefore, we develop another effective method to deal with this problem (i.e., mentioned in chapter 7). To quantitatively evaluate our proposed method, we use the blind contrast enhancement assessment metric proposed by Tarel *et al* [13]. Three indicators e , r and σ are computed in the evaluation for comparing the input hazy image and the processed image, where e represents the rate of edges newly visible after enhancement, r estimates the average visibility enhancement obtained by the enhancement algorithm, and σ is the percentage of pixels that becomes completely black or completely white after dehazing. Generally speaking, there should be higher values of e and r and lower value of σ in a better dehazed image. Table 3.2 shows the quantitative performance for Fig. 3.19. It is observed from r , and there are higher average visibilities in our result by proposed underwater enhancement method (i.e., mentioned in chapter 7). In addition, our proposed underwater enhancement method is able to achieve the smaller percentage of pixels which become completely black or completely white.

More experimental results can be found:

<https://sites.google.com/site/yutaisaithesis/dehaze>

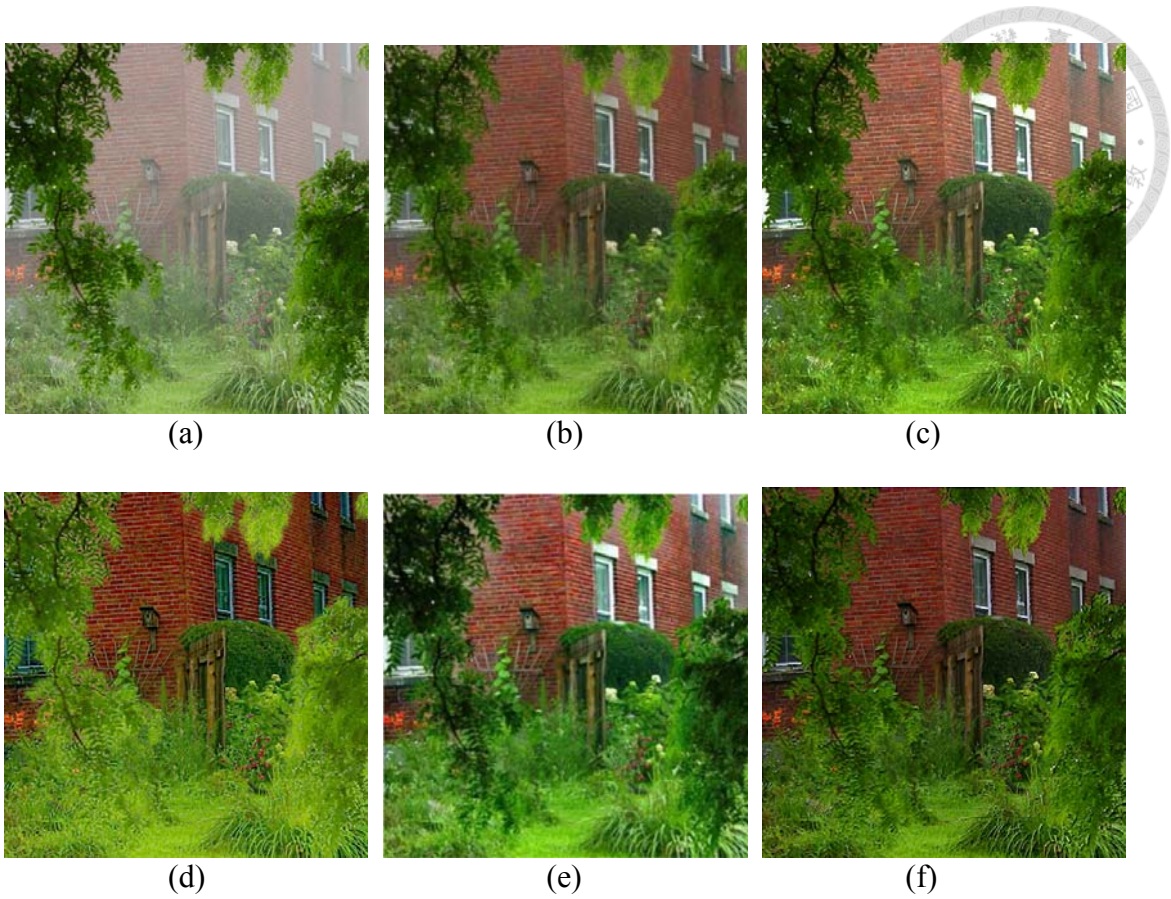


Fig. 3.12 Comparative results of the proposed method and the conventional methods on the “house” image. (a) The input hazy image. The dehazed images obtained by (b) He et al.’s method [3], (c) Pei et al.’s method [39], (d) Nishino et al.’s method [45], (e) Kim et al.’s method [44], and (f) the proposed method.

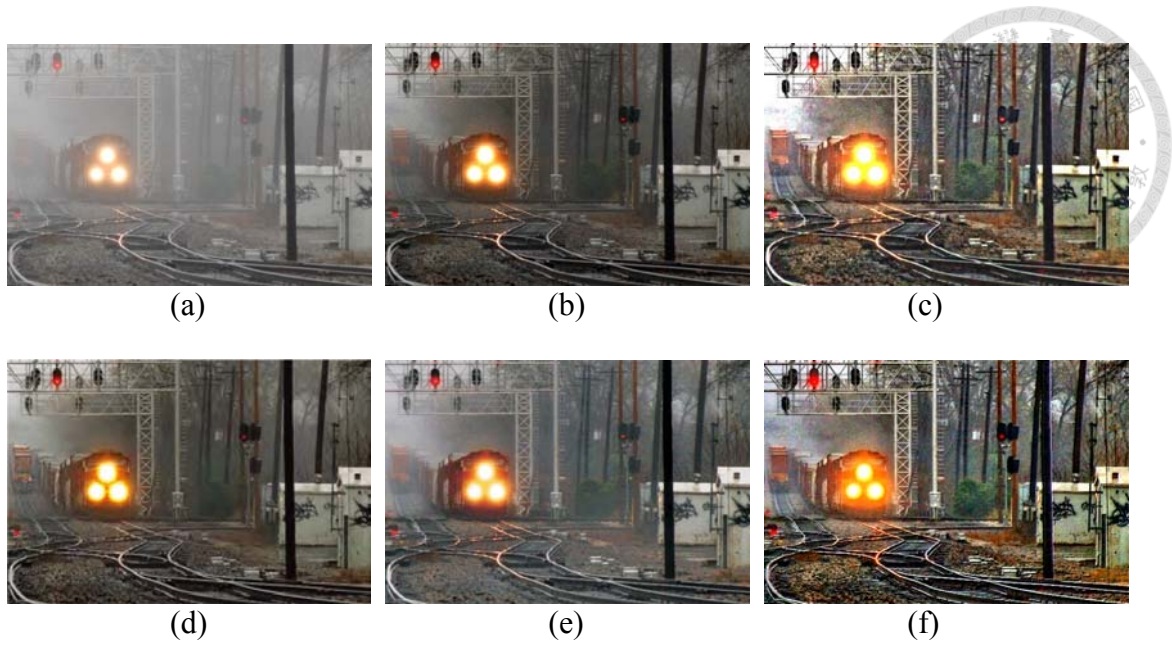


Fig. 3.13 Comparative results of the proposed method and the conventional methods on the “train” image. (a) The input hazy image. The dehazed images obtained by (b) He et al.’s method [3], (c) Pei et al.’s method [39], (d) He et al.’s method with multiple scattering model [40], (e) C. O. Ancuti et al.’s method [41], and (f) the proposed method.

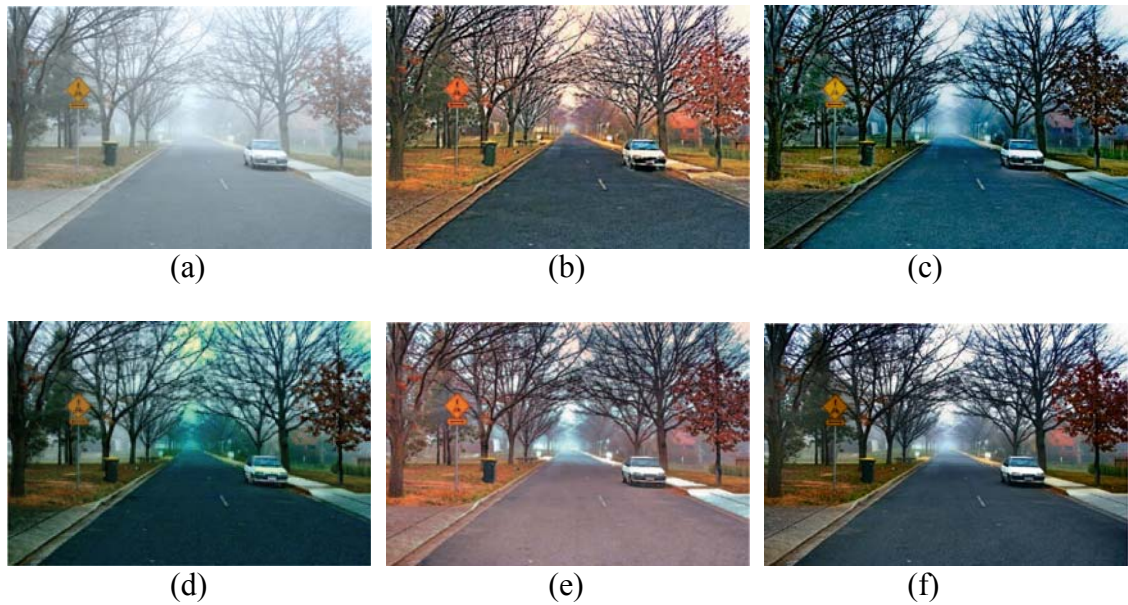


Fig. 3.14 Comparative results of the proposed method and the conventional methods on the “sweden” image. (a) The input hazy image. The dehazed images obtained by (b) Tan et al.’s method [3], (c) Zhang et al.’s method [46], (d) Nishino et al.’s method [45], (e) C. O. Ancuti et al.’s method [41], and (f) the proposed method.



(a)



(b)



(c)



(d)



(e)



(f)



(g)



(h)



(a)



(b)



(c)



(d)



(e)



(f)



(g)



(h)

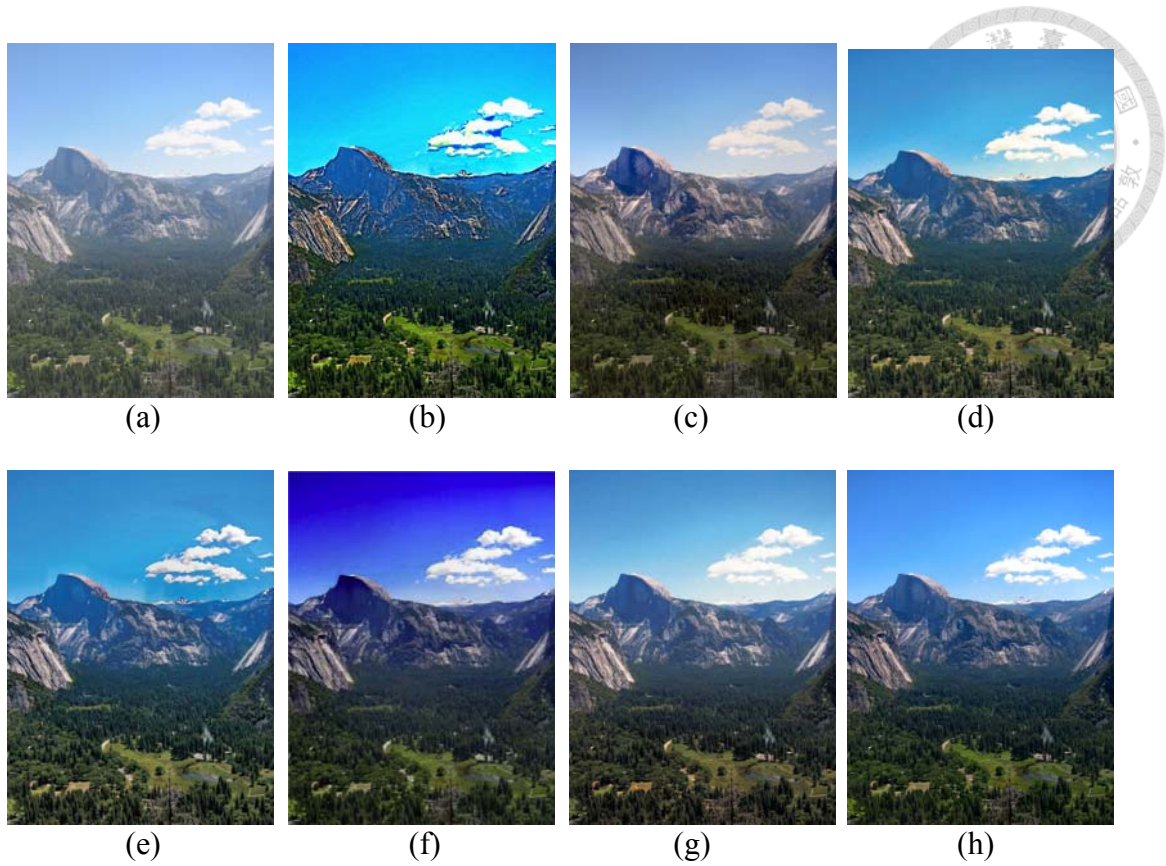


Fig. 3.15 Comparative results of the proposed method and the conventional methods on the “ny12”, “ny17”, and “y01” images. (a) The input hazy image. The de-hazed images obtained by (b) Tan et al.’s method [1] (2008), (c) Fattal et al.’s method [2] (2008), (d) He et al.’s method [3] (2009), (e) Nishino et al.’s method [45] (2012), (f) Kim al.’s method [44] (2013), (g) C. O. Ancuti al.’s method [41] (2013), and (h) the proposed method.

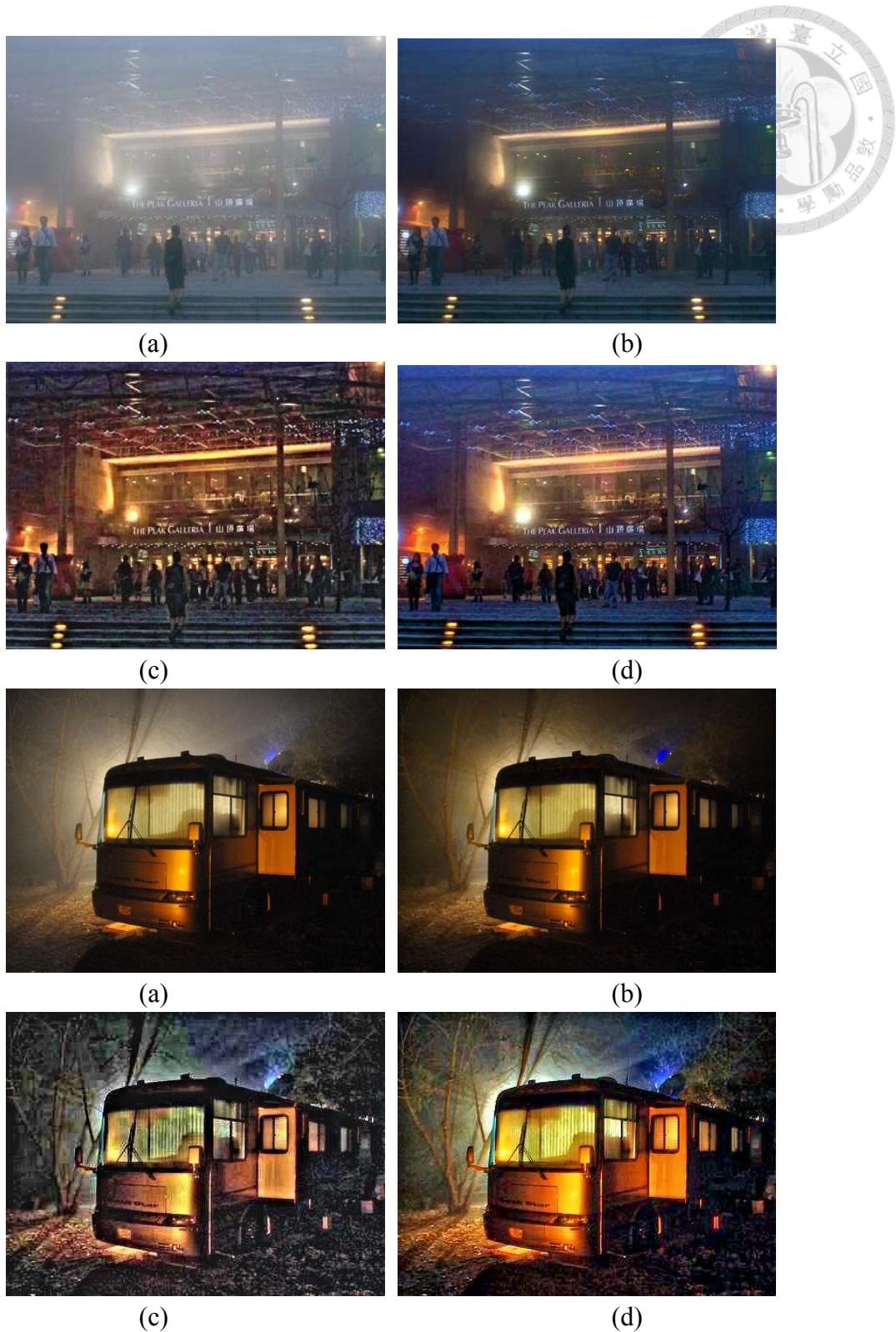
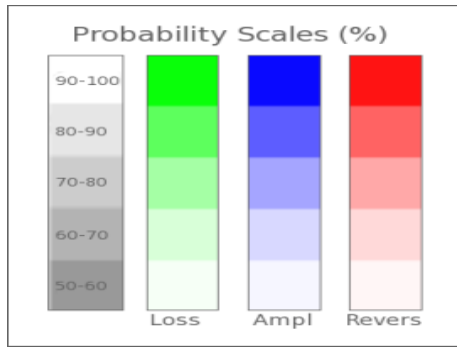


Fig. 3.16 Comparative results of the proposed method and the conventional methods on the nighttime haze images. (a) The input nighttime hazy images. The dehazed images obtained by (b) He et al.'s method [3], (c) Pei et al.'s method [32], and (d) the proposed method.



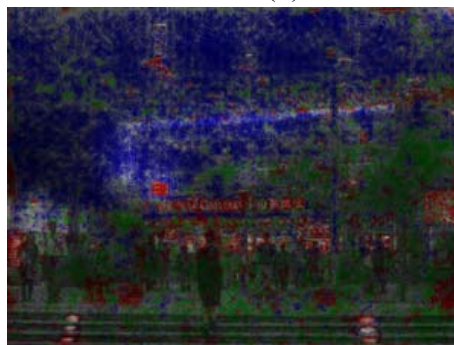
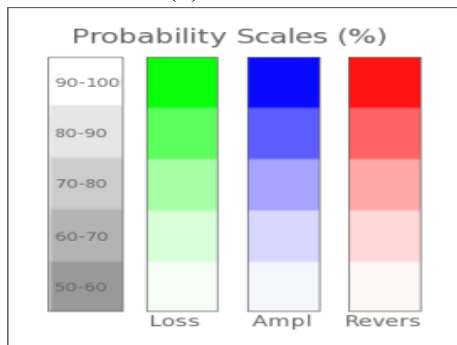
(a)

(b)



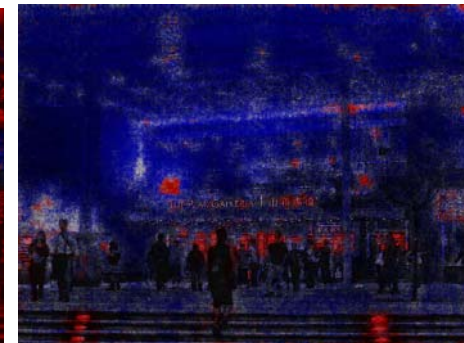
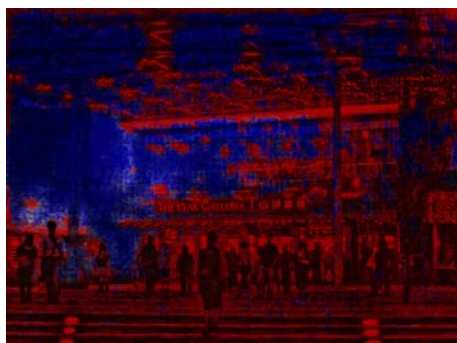
(c)

(d)



(a)

(b)



(d)

(d)

Fig. 3.17 Comparison of nighttime dehazed results: (a) Image quality metric. (b) He. et al.'s results extracted from Fig 3.15 when applied IQM metric. (c) Pei. et al.'s results extracted from Fig 3.15 when applied IQM metric. (d) Our results.



Fig. 3.18 Comparative results of the proposed method and the conventional methods on the nighttime haze images. (a) The input nighttime hazy images. The dehazed images obtained by (b) Pei et al.'s method [32], and (c) the proposed method.

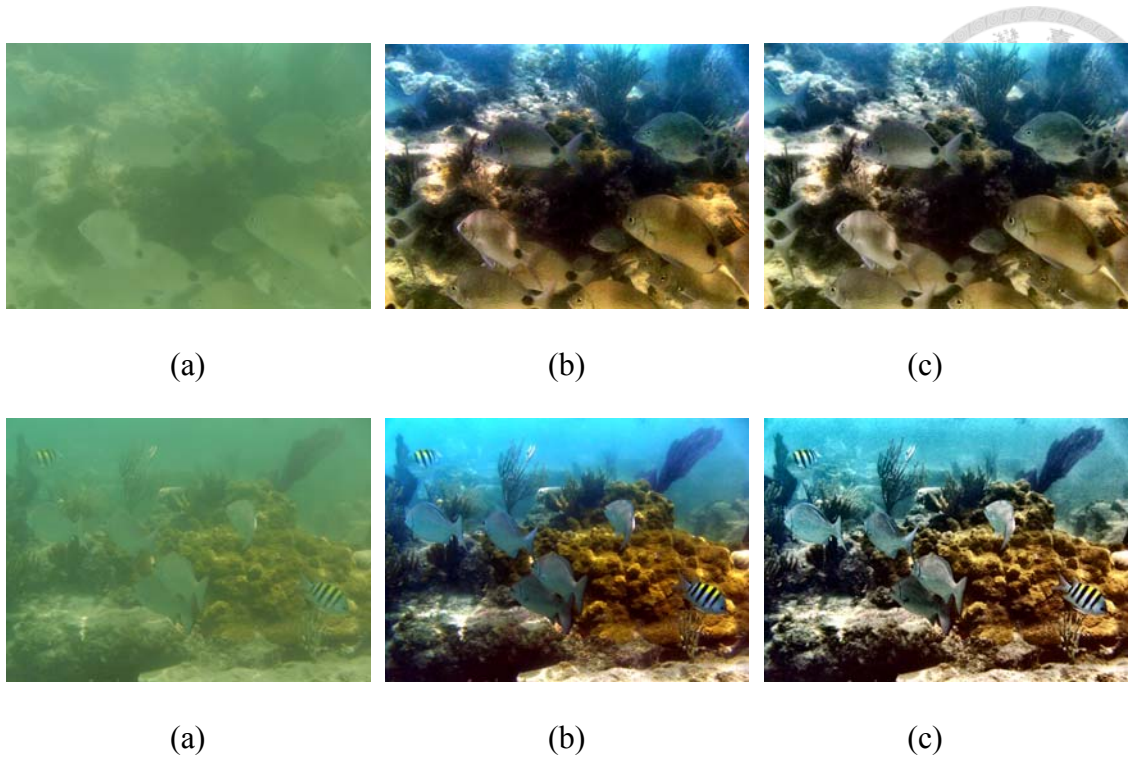


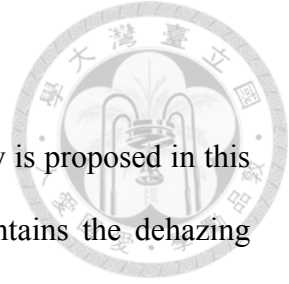
Fig. 3.19 Comparative results of the proposed method on the underwater image (up: PICT0403 and bottom: PICT0422). (a) Input underwater image. (b) Final enhancing image by proposed dehazing method. (c) Final enhancing image by proposed underwater enhancement method (i.e., mentioned in chapter 7).

	Ours dehazing method			Ours underwater enhancement method		
	e	σ (%)	r	e	σ (%)	r
PICT0403	457.7	0.449	7.76	325.8	0	6.27
PICT0422	9.361	0.172	5.61	7.181	0.001	6.33

Table 3.2 Qualitative Comparison of the two images (PICT0403 and PICT0422) show in Fig. 3.17. Based on the indicators of Hautiere et al. [13].

3.5 Conclusions

An attractive haze-removing method with high dehazing quality is proposed in this Chapter. Specifically, the proposed method is robustness and maintains the dehazing quality over various cases of haze images even in the limitation case (i.e., nighttime haze). Therefore, it provides a better choice than the methods previously designed. Some algorithmic refinements will be applied and then integrated into the haze-removing method in order to decrease the complexity and improve the dehazing image quality.



Chapter 4 Related Work of Rain/Snow Removal in Single Image



Most deraining methods [47–51] have focused on the removal of rain streaks in video sequences, which are captured with static or dynamic cameras. These methods detect and remove rain streaks by exploiting high temporal correlation between consecutive frames. They assume that rain streaks are shifted between consecutive frames and detect the rain streak regions by observing the temporal brightness change. Then, they restore rain-free pixels in each frame by taking the average pixel values of the previous frame and the following frame. But they require the temporal information in video sequences. Therefore, they are not applicable to still images.

4.1 Introduction

In this section, we introduce several properties of rain and snow. First, rain incorporates in many falling drops. These drops have a distribution with various sizes. The drops have high falling velocities when they are near the ground. Second, each drop behaves like a transparent sphere, refracting and reflecting light from the environment towards the camera showed in Fig. 4.1. Third, the brightness of raindrops is independent and brighter than the background as showed in Fig. 4.2. The background scene consisted of horizontal stripes of different brightness shown in Fig. 4.3. Furthermore, the finite exposure time of the camera, intensities due to rain are motion blurred and hence depend on the background intensities showed in Fig. 4.4.

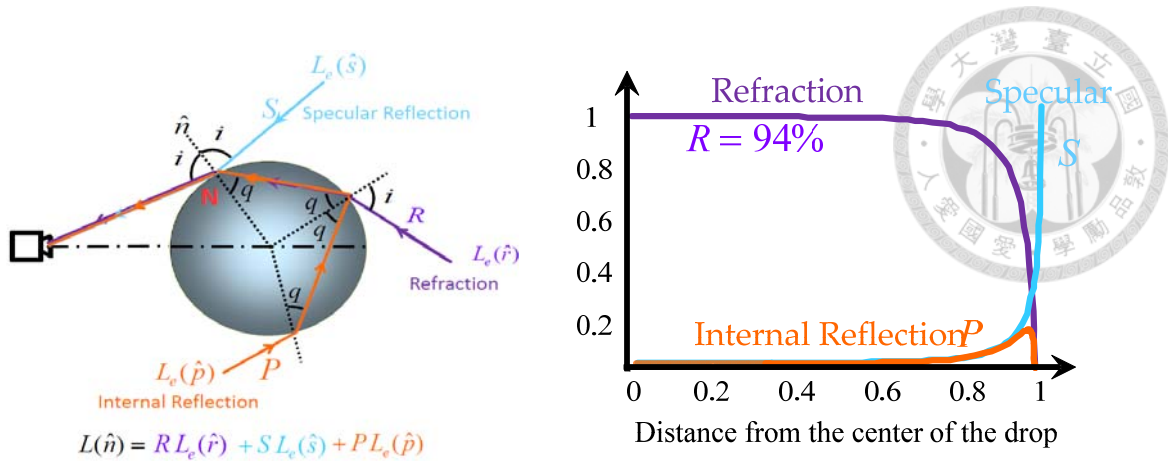


Fig. 4.1 Behavior of each drop.

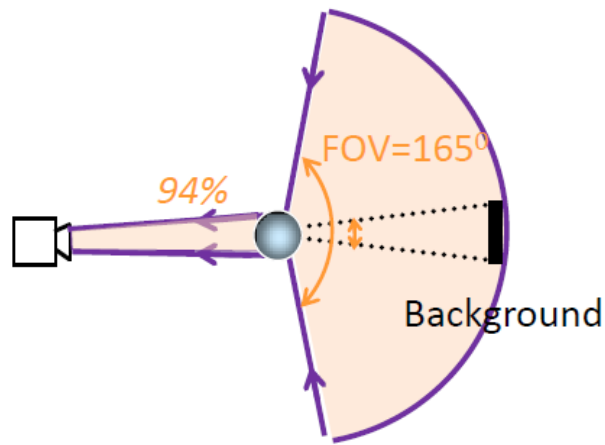


Fig. 4.2 Field view of a raindrop.

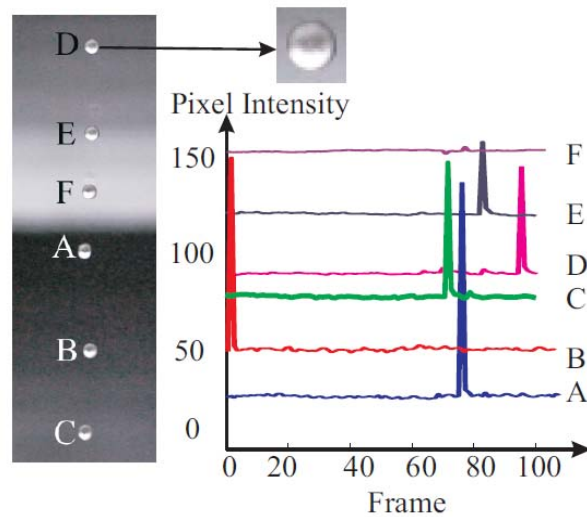


Fig. 4.3 Brightness levels produced by raindrops.



(a)

(b)

Fig. 4.4 Comparison of visual effects in two images at different exposure times. (a) Image with rain captured in high shutter speed (exposure time = $1/1000$ s). (b) Image with rain captured in normal shutter speed (exposure time = $1/30$ s).

Fourth, the size of a raindrop typically varies from the range from 0.1mm to 3.5 mm. Note that the density of raindrops exponentially decreases with the drop size. Generally, the shape of raindrops is spherical under smaller raindrops and oblate spherical under larger raindrops. Fig. 4.5 shows the distribution of a typical rainfall and the shapes of raindrops with various sizes. Fifth, the velocity is converged as a constant value when the raindrops fall through in the atmosphere. Sixth, the length of rain streaks is inversely proportional to the depth of raindrops. In most cases, rain streaks span several (up to ten) pixels in a frame. Seventh, two consecutive frames do not obtain the same rain streak because of the speed of raindrops. Moreover, since the raindrops are random over time, a pixel is not always covered by the raindrop during entire video. These raindrops properties are essential and important in many researches, and are also reviewed in this chapter for presentation completeness.

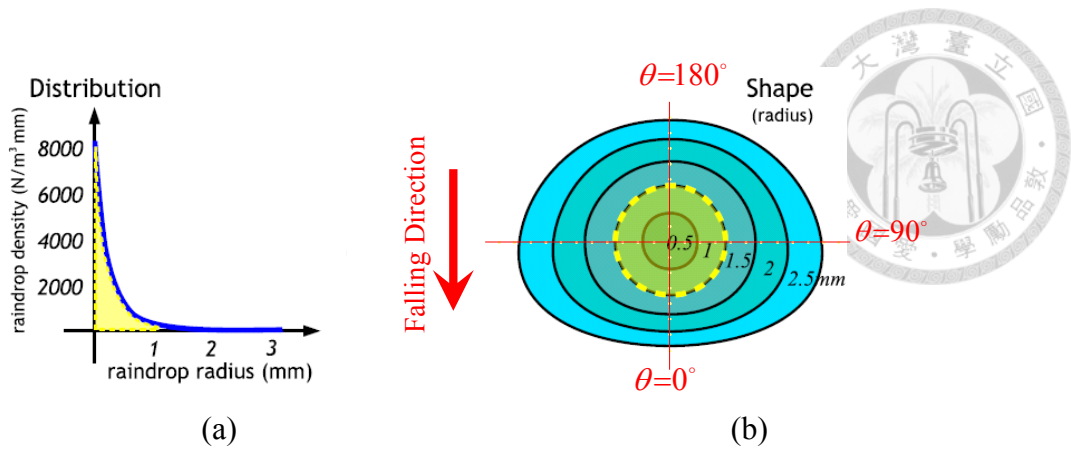


Fig. 4.5 Distribution of a typical rainfall and the shapes of raindrops with various sizes. (a) Drop size distribution. (b) Shapes of raindrops.

Several methods have been developed to remove rain and snow from videos. Two earlier proposed (i.e., [52], [53]) methods for removing dynamic weather use a temporal median filter for each pixel. They exploit the fact that in all but the heaviest rain, because in moderate intensity rain, each pixel is clear more often than corrupted. The problem is that any movement would become blurred. In order to overcome the drawbacks, more deraining methods [47–51] have focused on the removal of rain streaks in video sequences, which are captured with static cameras. These methods detect and remove rain streaks by exploiting high temporal correlation between consecutive frames. They assume that rain streaks are shifted between consecutive frames and detect the rain streak regions by observing the temporal brightness change. Then, they restore rain-free pixels in each frame by taking the average pixel values of the previous frame and the following frame. But they require the temporal information in video sequences. Therefore, they are not applicable to still images. In order to overcome the drawbacks, three existing typical rain removal methods: guidance image based [4], image decomposition analysis [5], adaptive nonlocal means filter [6], and frequency-based analysis [7] are introduced in the literature (i.e., Section 4.2 to 4.5). In this follows, we design a simple but effective rain and snow removal method by

combining the properties of rain or snow in spatial and temporal to detect and using inpainting procedures in Section 5.



4.2 Guidance Image Based Method

The Guidance Image based method had been proposed by Xu et al. [4] [54] in 2012. This method is based on the guidance image is derived from the imaging model. The removing of raindrops and snowflakes is quite challenging since each of them affects only on a small region of a single image. Describe in [54], to removal rain and snow only using one image, a guidance image such that no pixels-based statistical information to detect rain and snow are needed is derived from the imaging model of a raindrop or a snowflake when it is passing through an element on the CCD of the camera. Since only using this guidance image may lose some detailed information, Xu et al. improve the performance by refining guidance image [4]. This refined guidance image has similar contour with the un-degraded image and also maintains the detailed information which may be lost at the guidance image. Then a removal procedure is given by the use of the refined guidance image. The refined guidance image can be used to get a better result in rain removal and snow removal.

4.2.1 Basic Concept of Guidance Image

Xu et al. [4] focus on finding a way to keep the edges of objects and remove the edges caused by snow or rain. They apply a guidance image to decide which edge should be remained and which region should be smoothed. The flow chart of this method [4] is briefly expressed in Fig. 4.6. Let T is the exposure time and τ be the time that a rain drop or snowflake passing through an element on the CCD. The

intensity value I_{rs} at a pixel in an image captured at a rainy day or snow day is a linear combination of the time-averaged irradiance of rain drops or snow flakes \bar{E}_{rs} and the time-averaged irradiance of background \bar{E}_b . Hence, the image model can be expressed as followed

$$I_{rs} = \int_0^\tau \bar{E}_{rs} dt + \int_\tau^T \bar{E}_b dt \quad (4.1)$$

Let I_b be the intensity of background, I_E be the intensity value of raindrops or snowflake satisfies $I_E = T \cdot \bar{E}_{rs}$ and a variable α be the ratio between τ and T .

We could rewrite (4.1) as

$$I_{rs} = \alpha \cdot I_E + (1 - \alpha) \cdot I_b \quad (4.2)$$

Ordinarily snowflakes and raindrops are falling down with fast speed. The time duration τ is far less than T . So the value of variable $\alpha \rightarrow 0$. The time duration τ is affected by many factors such as the speed, the distance between raindrops or snowflakes and the camera. Therefore it could not compute the exact τ value of each pixel covered by raindrops or snowflakes.

In natural property, the raindrops and snow are brighter than background and have independent brightness of background. Besides, the intensity values of raindrops and snow almost have the same value in the *RGB* color space. They defined $I_{b-\max}$ and $I_{b-\min}$ as the maximum and minimum values of the three coordinate values of I_b . The relation can be expressed as

$$\begin{aligned} I_{rs-\max} &= \alpha \cdot I_{E-\max} + (1 - \alpha) \cdot I_{b-\max} \\ I_{rs-\min} &= \alpha \cdot I_{E-\min} + (1 - \alpha) \cdot I_{b-\min} \end{aligned} \quad (4.3)$$

Due to raindrop and snowflake have white color, $I_{E-\max}$ is same as $I_{E-\min}$. Subtract $I_{rs-\min}$ from $I_{rs-\max}$ to get the guidance image I_f .

$$I_f = I_{rs-\max} - I_{rs-\min} = (1 - \alpha)(I_{b-\max} - I_{b-\min}) \quad (4.4)$$

According to [55], they defined J as the output image of raindrop and snowflake removal. p is the input image, $|\omega|$ is the number of pixel in ω_k , ω_k is the region in the kernel, k is the location in the kernel, μ_k and σ_k^2 are the mean and variance of I respectively in ω_k . Hence, the output image J at each channel is as followed

$$J_i = \bar{a}_k \cdot I_i + \bar{b}_k \quad (4.5)$$

where

$$a_k = \frac{1}{|\omega|} \frac{\sum_{i \in \omega_k} I_i P_i - \mu_k p_k}{\sigma_k^2 + \varepsilon} \quad (4.6)$$

$$b_k = \bar{p}_k - a_k \mu_k \quad (4.7)$$

This method could remove rain or snow, but it also removes some detailed information such as tiny edge. Therefore, they focus on this problem and improve the guidance image. They assume x be the location of edge and $x+1$ is not on the edge. The relationship of these two intensity value satisfies $I(x) \neq I(x+1)$ but $J(x)$ is an average value of a local region due to guided filter method. Therefore, the subtraction image between $J(x)$ and $I(x)$ has the wrong elimination information. They use an average value of this subtraction image and the guidance image I_f as a refined guidance image

$$I_g = \frac{I_f + J_g}{2} \quad (4.8)$$

where J_g is the gray image of $J - I_{rs}$. Fig. 4.7 shows two results of rain and snow removal, respectively. The results show that the refined guidance image is better than the guidance image in rain removal and snow removal.

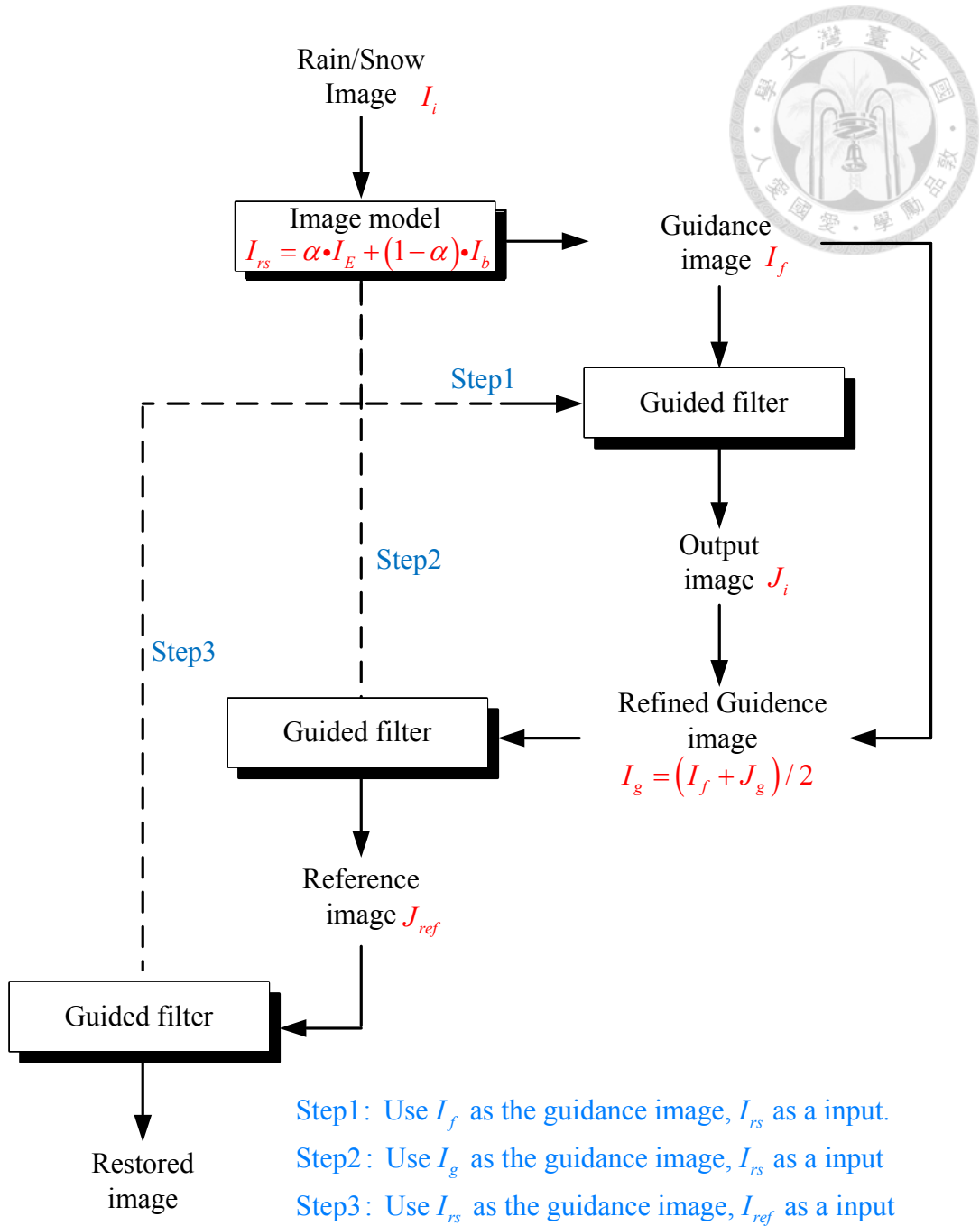


Fig. 4.6 Flow chart of the algorithm proposed by Xu. et al. [4].

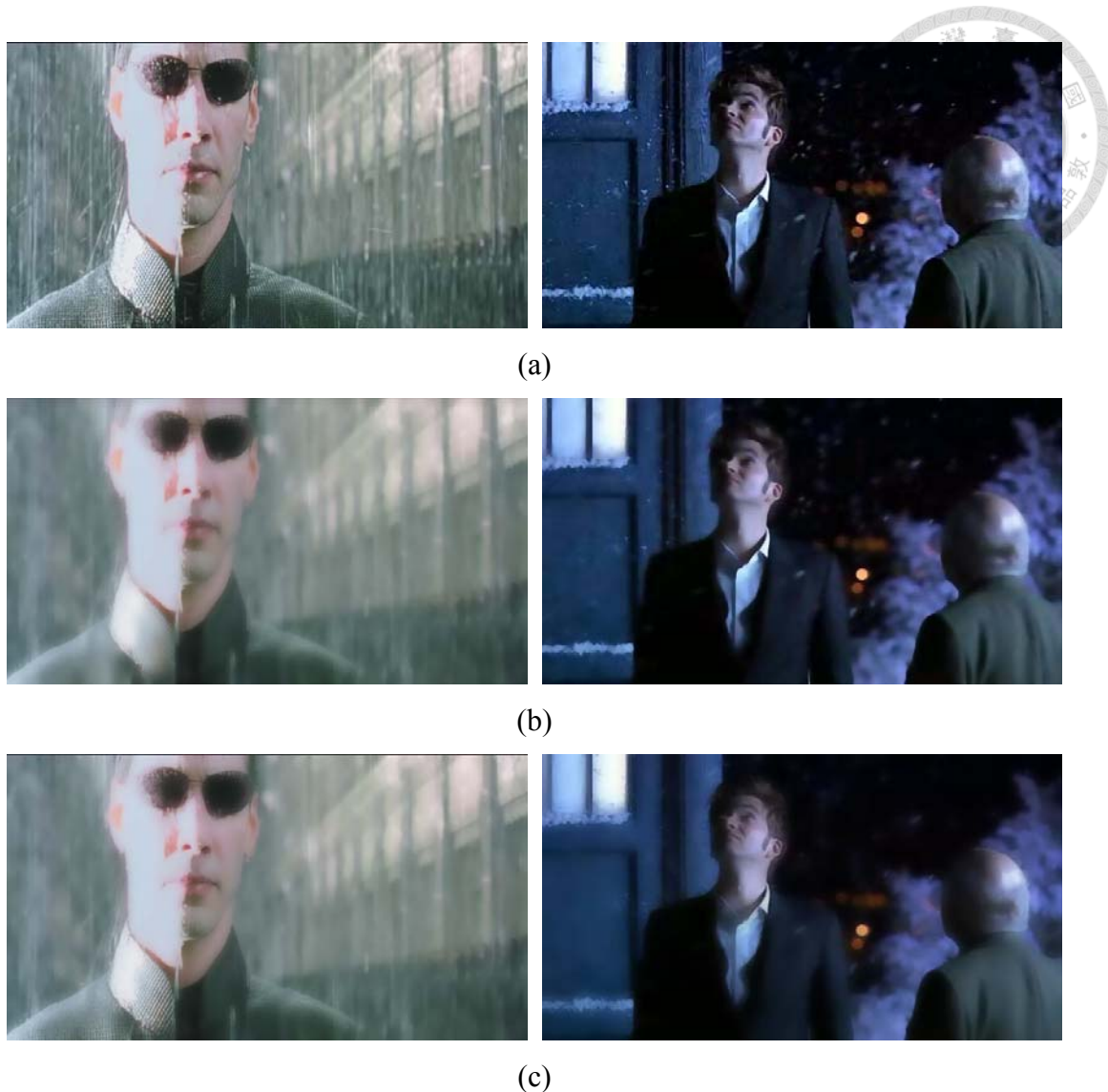


Fig. 4.7 The results of the rain and snow removal: (a) Input rain/snow image. (b) The removal results by using guidance image. (c) The removal results by using refined guidance image.

4.2.2 Advantage and Disadvantage

Guided filter is an edge-preserving smoothing filter, and has good behavior near the edges [55]. Guidance image can be itself or another reference image. Besides, “the guided filter has a fast and non approximate linear-time algorithm, whose computational complexity is independent of the filtering kernel size”. The refined guidance image has similar contour with the un-degraded image and also maintains the detailed information

which may be lost at the guided filter [55]. Although these methods can remove most rain or snow, but it still simultaneously removes other image detail as well.



4.3 Image decomposition

Kang et al. [5] proposed a single-image rain streak removal algorithm based on the morphological component analysis in 2012. Their method decomposes a rainy image into basis vectors based on the sparse representation. It then clusters the basis vectors into two kinds of components: geometrical components and rain streak components. Finally, it employs only the geometrical components to reconstruct a rain-free image.

4.3.1 Basic Concept of image decomposition

Kang et al. [5] proposed a single-image rain streak removal algorithm based on the morphological component analysis (MCA). The flow chart of this method [5] is briefly expressed in Fig. 4.8. First, they roughly decomposed an rainy image I into the low-frequency (LF) and high-frequency (HF) parts using the bilateral filter [38], i.e., $I = I_{LF} + I_{HF}$. The bilateral filter can smooth an image while preserving edges by means of a nonlinear combination of nearby images values. The most fundamental information will be retained in the LF part while the rain streaks and other edge or texture information will be included in the HF part. And then, they perform the dictionary learning and sparse coding based on MCA. They learn a dictionary D_{HF} based on the training exemplar patches extracted from I_{HF} to further decompose I_{HF} , where D_{HF} can be divided into two sub-dictionaries by performing HOG [56] feature-based dictionary atom clustering: the rain streak components D_{HF-R} and the

geometrical components D_{HF-G} as illustrated in Fig 4.9. Then, They perform sparse coding [57] by applying the OMP algorithm [57] for each patch b_{HF}^k extracted from I_{HF} via minimum (4.9)

$$\min_{\theta_{HF}^k \in R^m} \|b_{HF}^k - D_{HF} \theta_{HF}^k\|_2^2 \text{ s.t. } \|\theta_{HF}^k\|_0 < L \quad (4.9)$$

where $b_{HF}^k \in R^n$ defined as the k th patch extracted from I_{HF} , $k=1, 2, \dots, P$. $\theta_{HF}^k \in R^m$ are the sparse coefficients of b_{HF}^k with respect to $D_{HF} \in R^{n \times m}$, $n < m$, and L is the sparsity or maximum number of nonzero coefficients of θ_{HF}^k . Each reconstructed patch b_{HF}^k can be used to recover either the rain streak components I_{HF}^R or the geometrical components I_{HF}^G . They set the coefficients corresponding to D_{HF-R} in $\tilde{\theta}_{HF}^k$ to zeros to obtain θ_{HF-G}^k . Hence, each patch b_{HF}^k can be re-expresses as $\tilde{b}_{HF-R}^k = D_{HF-R} \times \tilde{\theta}_{HF-R}^k$, which can be used to recover I_{HF}^G . Followed by integrating with the LF part of the image to obtain the rain-free image $I^{Rain-free} = I_{LF} + I_{HF}^G$.

The performance of their algorithm depends on the clustering of basis vectors. When the clustering is not effective, their algorithm may erase textures, as well as rain streaks, and yield visual artifacts in a restored image.

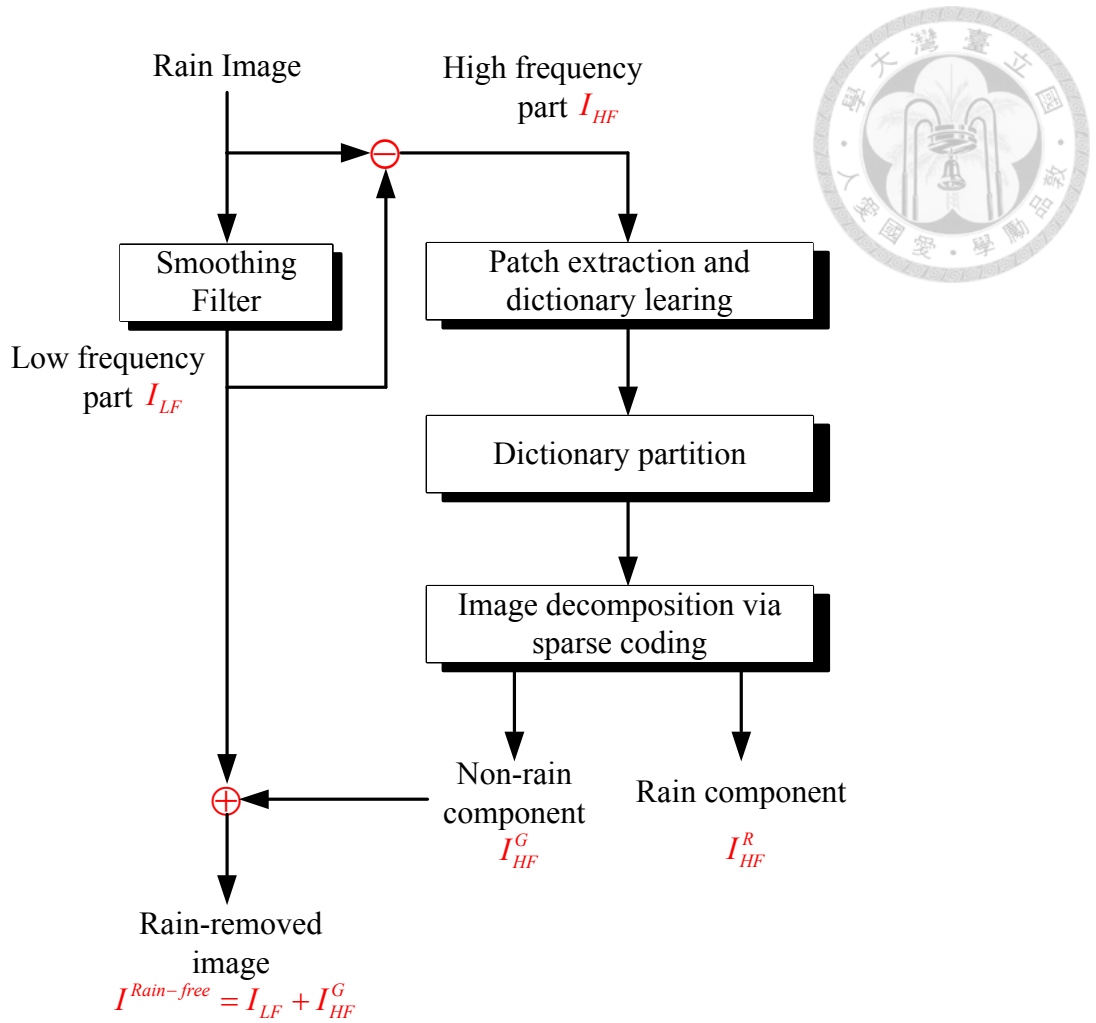


Fig. 4.8 Flow chart of the algorithm proposed by Kang. et al. [5].

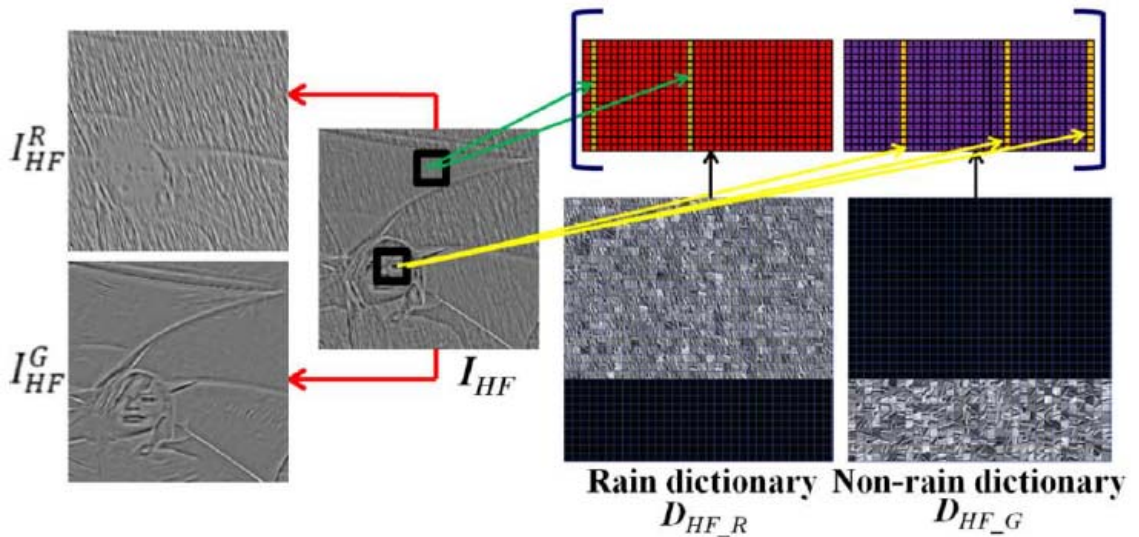


Fig. 4.9 The proposed by Kang. et al. based on two learned local dictionaries [5].



4.3.2 Advantage and Disadvantage

Kang et al. [2] proposed a single-image rain streak removal algorithm based on the morphological component analysis. Their algorithm decomposes a rainy image into basis vectors based on the sparse representation. It then clusters the basis vectors into two kinds of components: geometrical components and rain streak components. Finally, it employs only the geometrical components to reconstruct a rain-free image. The performance of their algorithm depends on the clustering of basis vectors. When the clustering is not effective, their algorithm may erase textures, as well as rain streaks, and yield visual artifacts in a restored image

4.4 Adaptive nonlocal means filter

Kim et al. [6] proposed a simple but efficient single-image deraining algorithm in 2013. They observe that a typical rain streak has an elongated elliptical shape with vertical orientation. Thus they detect rain streak regions by analyzing the rotation angle and the aspect ratio of the elliptical kernel at each pixel location. They use the nonlocal means filtering on the detected rain streak regions by selecting nonlocal neighbor pixels and their weights adaptively.

4.4.1 Basic Concept of adaptive nonlocal means filter

The adaptive nonlocal means filtering for rain removal algorithm had been proposed in [6]. The main idea is to exploit three properties of rain in single image and extract these components by employing the kernel regression method in [58]. They

defined W_p is a window centered at a pixel and analyze the structure of W_p by using the covariance matrix C_p , which is defined as below

$$C_p = \frac{1}{|W_p|} \sum_{\mathbf{q} \in W_p} \begin{bmatrix} g_x^2(\mathbf{q}) & g_x(\mathbf{q})g_y(\mathbf{q}) \\ g_x(\mathbf{q})g_y(\mathbf{q}) & g_y^2(\mathbf{q}) \end{bmatrix} \quad (4.10)$$

where $g_x(\mathbf{q})$ and $g_y(\mathbf{q})$ are the gradient values at pixel \mathbf{q} in the horizontal and vertical directions, respectively, and $|W_p|$ is the numbers of pixels in W_p . The orientation and shape of an ellipse can be confirmed by using the SVD to the covariance matrix C_p . i.e.

$$\begin{aligned} C_p &= \mathbf{U}\mathbf{\Sigma}\mathbf{V}^T \\ \mathbf{U} &= \begin{bmatrix} \cos \theta_p & -\sin \theta_p \\ \sin \theta_p & \cos \theta_p \end{bmatrix} \\ \mathbf{\Sigma} &= \begin{bmatrix} \lambda_p & 0 \\ 0 & \mu_p \end{bmatrix} \end{aligned} \quad (4.11)$$

where \mathbf{U} is the rotation matrix, $\mathbf{\Sigma}$ is the scaling matrix, θ_p is the rotation angle of the elliptical kernel, and two eigenvalues λ_p and μ_p are the kernel scales in the direction of the major and the minor axes. In order to avoid the structures of others subjects, they modify the covariance by weighting the gradient at each pixel. They overall weight $w_{all}(\mathbf{q}) = w_1(\mathbf{q})w_2(\mathbf{q})w_3(\mathbf{q})$ by combining the weights of the three properties. The first property is related to the luminance. They design a weight $w_1(q)$ for pixel \mathbf{q} using the difference between its luminance values $Y(\mathbf{q})$ and the average value of the luminance in the window W_p . Thus $w_1(\mathbf{q})$ can be expressed as

$w_1(\mathbf{q}) = \frac{1}{1 + \exp^{-\kappa[Y(\mathbf{q}) - \bar{Y}_p]}}$, where κ is the sensitivity of the luminance weighing function (set to 0.1). The second is the distance weight $w_2(\mathbf{q})$, which is defined as the

inversely proportional to the distance between pixel \mathbf{q} and the center pixel \mathbf{p} . If two pixels are far from each other, they are less likely to belong to the same rain streak.

Thus $w_2(\mathbf{q})$ can be expressed as $w_2(\mathbf{q}) = \exp(-\|\mathbf{p} - \mathbf{q}\|^2 / \sigma_b^2)$, where σ_b is set to 3

in this algorithm. The third property assumes that pixels in a rain streaks have same color. Thus the color weight $w_3(\mathbf{q})$ can be expressed as

$w_3(\mathbf{q}) = \exp(-\|I(\mathbf{p}) - I(\mathbf{q})\|^2 / \sigma_c^2)$, where σ_c is set to 9 in this algorithm. They

modify the covariance matrix as

$$\tilde{\mathbf{C}}_p = \frac{1}{\sum_{\mathbf{q} \in W_p} w_{all}^2(\mathbf{q})} \cdot \sum_{\mathbf{q} \in W_p} w_{all}^2(\mathbf{q}) \begin{bmatrix} g_x^2(\mathbf{q}) & g_x(\mathbf{q})g_y(\mathbf{q}) \\ g_x(\mathbf{q})g_y(\mathbf{q}) & g_y^2(\mathbf{q}) \end{bmatrix} \quad (4.12)$$

From (4.12), it can find that the rainy pixels contribute more than the rain-free pixels.

They state pixel \mathbf{p} is rain, i.e. $M(\mathbf{p}) = 1$, when the following three conditions are satisfied

$$\begin{aligned} |\theta_p - \pi/2| &< \pi/6 \\ \lambda_p / \mu_p &> 2 \\ \mu_p &> 10 \end{aligned} \quad (4.13)$$

Finally, they remove the binary rain streak map by applying the adaptive nonlocal mean filter. It can be expressed as

$$\tilde{I}(\mathbf{p}) = \frac{\sum_{\mathbf{q}} \exp\left(-\frac{\|\tilde{\mathbf{B}}_p - \tilde{\mathbf{B}}_q\|}{\sigma^2 N_{p,q}}\right) (1 - M(\mathbf{q})) I(\mathbf{q})}{\sum_{\mathbf{q}} \exp\left(-\frac{\|\tilde{\mathbf{B}}_p - \tilde{\mathbf{B}}_q\|}{\sigma^2 N_{p,q}}\right) (1 - M(\mathbf{q}))} \quad (4.14)$$

$$\text{where } \begin{cases} \tilde{\mathbf{B}}_p = \mathbf{B}_p \otimes (1 - \mathbf{R}_p) \otimes (1 - \mathbf{R}_q) \\ \tilde{\mathbf{B}}_q = \mathbf{B}_q \otimes (1 - \mathbf{R}_p) \otimes (1 - \mathbf{R}_q) \end{cases}$$

where \mathbf{B}_p and \mathbf{B}_q are the vectors represent the pixel within blocks centered at \mathbf{p} and

\mathbf{q} , respectively, σ is the Gaussian parameter, \mathbf{R}_p and \mathbf{R}_q are the binary vectors which correspond to the blocks centered at \mathbf{p} and \mathbf{q} , respectively, $N_{p,q}$ is the number of nonzero elements in the vector $(1-\mathbf{R}_p) \otimes (1-\mathbf{R}_q)$. Fig 4.10 shows an example of the rain streak map. Fig. 4.10(a) is an input image, Fig. 4.10(b) is the angel map of rotation angle θ_p , Fig. 4.10(c) is the ratio map λ_p/μ_p of eigenvalues, and Fig. 4.10(c) is the extracted rain streak map.

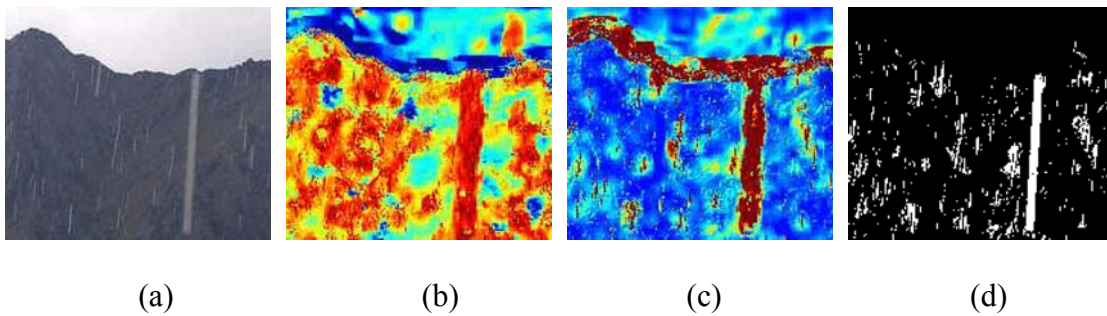


Fig. 4.10 An example of the rain streak map [6]. (a) Input image. (b) The angel map of rotation angle θ_p . (c) The ratio map λ_p/μ_p of eigenvalues. (d) The extracted rain streak map.

4.4.2 Advantage and Disadvantage

This method can remove rain streaks more faithfully, without yielding artifacts, than the conventional algorithms [6]. This method is effective when the streaks are against a relatively textureless background. However, defocused streaks and streaks on bright backgrounds produce a very small intensity changes so that are difficult to detect in the presence of noise. In this case, the rain streaks cannot be completely removed. When raindrops are broken with splashes falling on the subjects, the rotation angle of the rain streak may have a horizontal orientation. In this case, the rain streaks cannot be removed.

4.5 Frequency-Based Analysis

The frequency-based method had been proposed by Barnum et al. [7] in 2006. They show that dynamic weather has a predictable global effect in frequency space and develop a model of the shape and appearance of a single rain and snow streak in image space. They find that detecting individual streaks is difficult even with an accurate appearance model. Thus, they combine the streak model with the statistical characteristics of rain and snow to create a model of the overall effect of dynamic weather in frequency space. The model is proper to a video and is used to detect rain and snow streaks first in frequency space, and the detection result is then transferred to image space. The frequency model is fitted to an image sequence by matching streak orientation and rain (snow) intensity. Once the rain and snow streaks are detected, the major rain drops in the image can be eliminated.

4.5.1 Basic Concept of Frequency-Based Analysis Method

Barnum et al. [7] treat rain as image-global phenomena rather than individual pixels or patches. The main idea is that they do not need to find each of a hundred rain and snow streaks in the image. They just go to the frequency space, where it would form an elliptical structure, and this ellipse is the sum of all the rain streaks showed in Fig. 4.11.

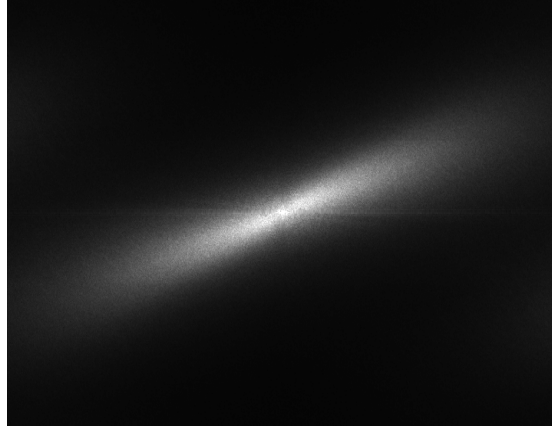


Fig. 4.11 Fourier transform of the streaks.

Thus, they predict the appearance of rain in the image by combining the information of how the rain and snow streak present and forecasting the range of streak sizes. The general shape and appearance of a streak can be approximated with a motion-blurred, circular Gaussian, moving at the same speed as the real raindrop, snowflake, making a streak of the same length and breadth (see in Fig. 4.12). For horizontal and vertical frequencies (u, v) , a blurred Gaussian G with breadth b and length l is given by

$$\begin{aligned}
 G(u, v; b, l) &= \int_0^1 \exp(-b^2(u^2 + v^2)) \exp(2\pi i y v) dy \\
 &= \begin{cases} i \frac{\exp(-b^2(u^2 + v^2))(1 - \exp(2\pi i l v))}{2\pi v} & v \neq 0 \\ \exp(-b^2 u^2) l & v = 0 \end{cases} \quad (4.15)
 \end{aligned}$$

where $(u, v; b, l)$ means at location (u, v) , with parameters (b, l) . Since streaks are often not completely vertical, the coordinate space can be rotated, giving the more general form $G(u, v; b, l, \theta)$. Then, all of the above components can be combined to make a model for illustrating how a rain appears in frequency space. The streak model can be written as

$$R(u, v; \alpha, \hat{\theta}) = \alpha \int_{a_{\min}}^{a_{\max}} \int_{z_{\min}}^{z_{\max}} G(u, v; b(a, z), l(a, z), \theta) dz da \quad (4.16)$$

where u and v are spatial frequencies, z is meters away from the camera, $\hat{\theta}$ is a set of

the different streak orientations, and α is a precipitation rate. In Fig. 4.13, it explains the physical meaning of the streak approximation model in (4.16).

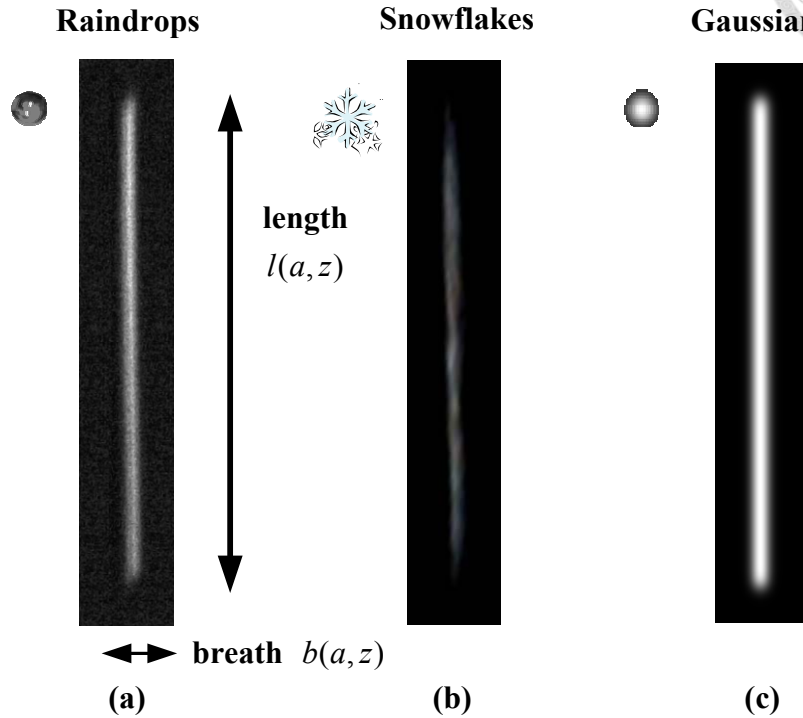


Fig. 4.12 Raindrops and snowflakes create streaks of different appearances, depending on factors such as the environmental illumination, their depth from the camera, and how much they are in focus. (a) A streak from a real raindrop. (b) A streak from a real snowflake. (v) A blurred Gaussian.

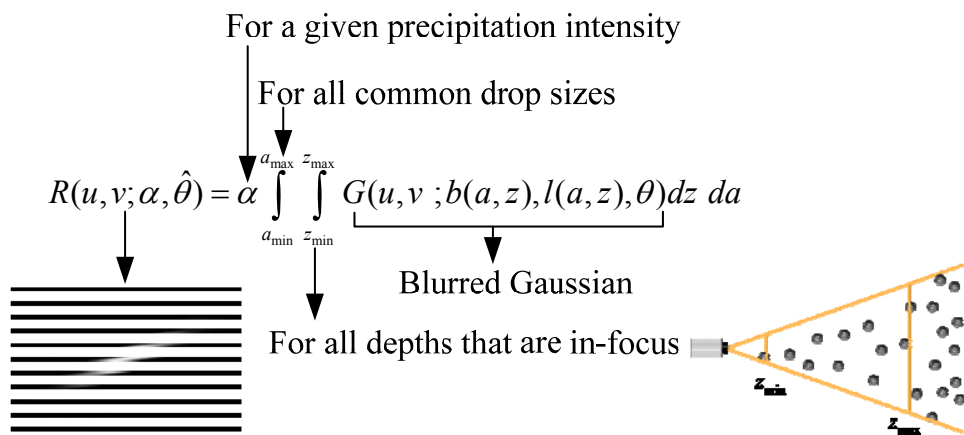


Fig. 4.13 Physical meaning of the streak approximation model in (4.6).

After generating a spatio-temporal model for streaks, a video of rain and snow $m(x, y, t)$ can be used to estimate the precipitation rate α and streak orientation θ per frame. Then, a rough streak model of the frequencies can be obtained by computing the standard deviation over time for each spatial frequency and T frames, expressed as

$$\begin{aligned}\tilde{R}(u, v) &= \sqrt{\frac{1}{T} \sum_{t=1}^T (\|M(u, v, t)\| - \|\bar{M}(u, v)\|)^2} \\ &= \text{stdev}(\|M(u, v, t)\|)\end{aligned}\quad (4.17)$$

where $M(u, v, t)$ is the 2D Fourier transform of $m(x, y, t)$ and \bar{M} is the mean across time. Then, the correct streak orientation θ is found by minimizing the following equation, for all $w \neq 0$.

$$\arg \min_{\theta} \int_{u, v, w} (\|R(u, v, w; \theta)\| - \tilde{R}(u, v))^2 du dv dw \quad (4.18)$$

Because rain generally fall in almost the same directions, so only one θ is needed showed in Fig. 4.14.

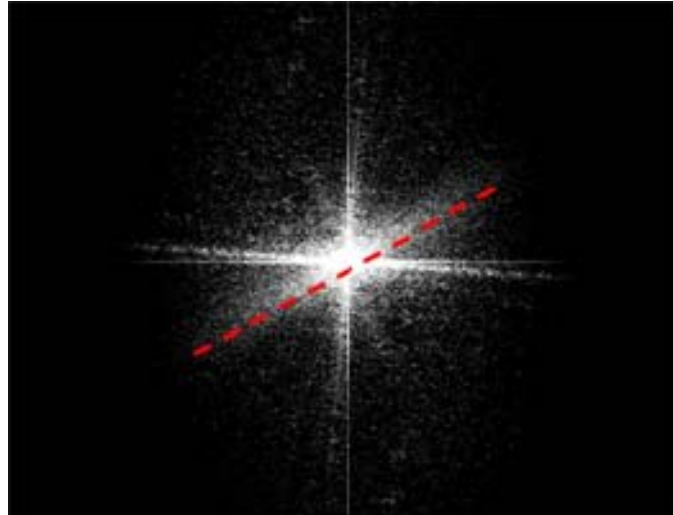
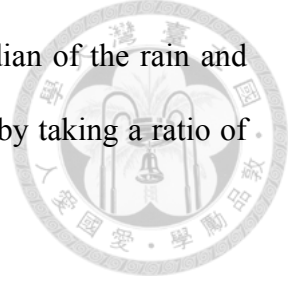


Fig. 4.14 Streak orientation.

Although most objects are clustered in the center, in the low-frequency portion of the spectrum, rain is widely distributed. Because of these two properties, they expect



the median of all frequencies to be approximately equal to the median of the rain and snow. Therefore, a rough estimate of the precipitation rate is found by taking a ratio of the median of all frequencies, again where $w \neq 0$, as

$$\alpha \approx \frac{\text{median}(|M(u, v, w)|)}{\text{median}(|R(u, v, w; \hat{\theta})|)} \quad (4.19)$$

Since rain and snow cover a wide part of frequency space, the median of all frequencies is robust enough to estimate α . By constructing the rain model and identifying the relevant parameters, they use a single frame and multiple frames to detect rain and snow. For a single frame, the probability that a given pixel is rain or snow is expressed as

$$p_2(x, y, t) = F^{-1} \left\{ \frac{|R(u, v; \alpha, \hat{\theta})|}{M(u, v)} \exp(i\phi\{M(u, v)\}) \right\} \quad (4.20)$$

where $M(u, v)$ is the two dimensional Fourier transform of one movie frame, ϕ is the phase of $M(u, v)$, and the lower case p is the probability in image space. When $R(u, v)$ is less or equal than $M(u, v)$, then the ratio indicates the estimated percentage of the rain and snow at that frequency. Contrarily, if $R(u, v)$ is greater than $M(u, v)$, then the ratio is greater than one and does not make sense. With mixed results, the rain or snow is found, but many errors are made. To fix them, evidence from multiple frames need to be used. According to the single frame operation, several consecutive single frames are estimated together. Then, finding out the best approach is to perform a three dimensional Fourier transform on blocks of two dimensional consecutive frames, to get a refined estimate. A three dimensional Fourier transform is applied $p_2(x, y, t)$ to obtain $P_2(u, v, w)$, and the resulting rain and snow estimation are then

$$p_3(x, y, t) = F^{-1} \left\{ \frac{R(u, v, w; \alpha, \hat{\theta})}{\|P_2(u, v, w)\|} \exp(i\phi\{M(u, v, w)\}) \right\} \quad (4.21)$$

where $p_3(x, y, t)$ denotes the final estimated location of the rain and snow. This is straightforward by taking three single frame estimates. Since rain and snow are constant across the temporal dimension, the model is constant in w . With this small change, most of the errors are vanished. Finally, they have to remove rain and snow by using the frequency space model. The detected rain or snow $p_3(x, y, t)$ that is estimated in (4.21) is used as a mixing weight between the original image m and an initial estimate \tilde{c} of the clear image c . Then, the detection $p_3(x, y, t)$ is multiplied by the removal rate α , where the product of $\alpha p_3(x, y, t)$ is capped at one:

$$c(x, y, t) = (1 - \alpha p_3(x, y, t))m(x, y, t) + \alpha p_3(x, y, t)\tilde{c}(x, y, t) \quad (4.22)$$

Images created with this equation will be temporally blurred only while the rain and snow are present. However, the disadvantage is that it can never remove more rain and snow than the initial estimate. Thus, they also propose another idea that if removal is more important than smoothness, then they iterate the detection and removal by

$$c^n(x, y, t) = (1 - \alpha p_3^n(x, y, t))c^{n-1}(x, y, t) + \alpha p_3^n(x, y, t)\tilde{c}^{n-1}(x, y, t) \quad (4.23)$$

Although the result from each subsequent iteration is clearer than the previous, the amount of rain and snow streaks removed decrease with iterations. Fig. 4.15 shows the results from the iterative removal method on two sequences with moving cameras and scenes. The flow chart of this paper [7] is illustrated in Fig. 4.16.

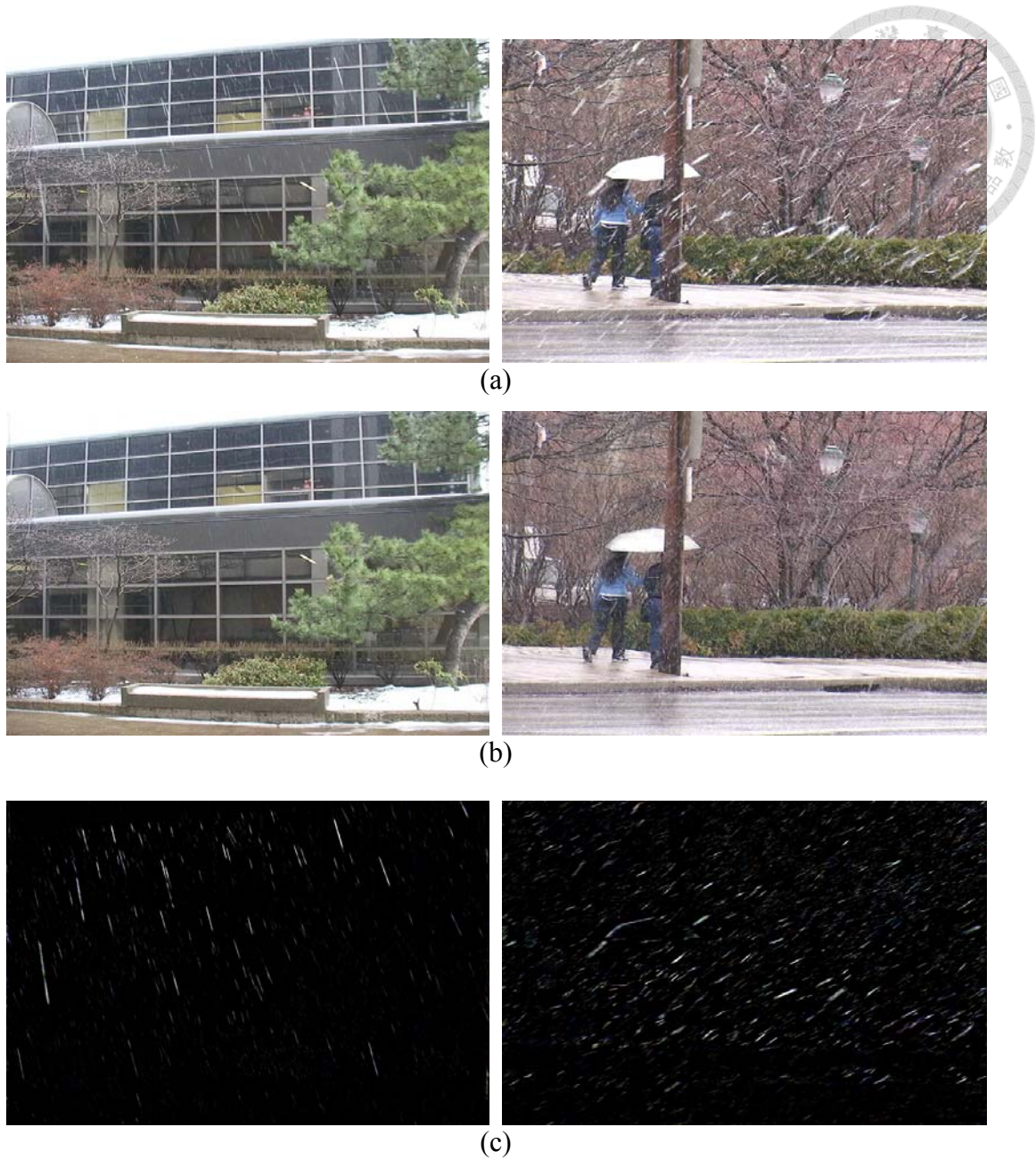


Fig. 4.15 Results from the iterative removal method on two sequences with moving cameras and scenes. (a) Sequence in the original video. (b) Derain and desnow results, respectively. (c) Improved estimation of rain and snow image with temporal information.

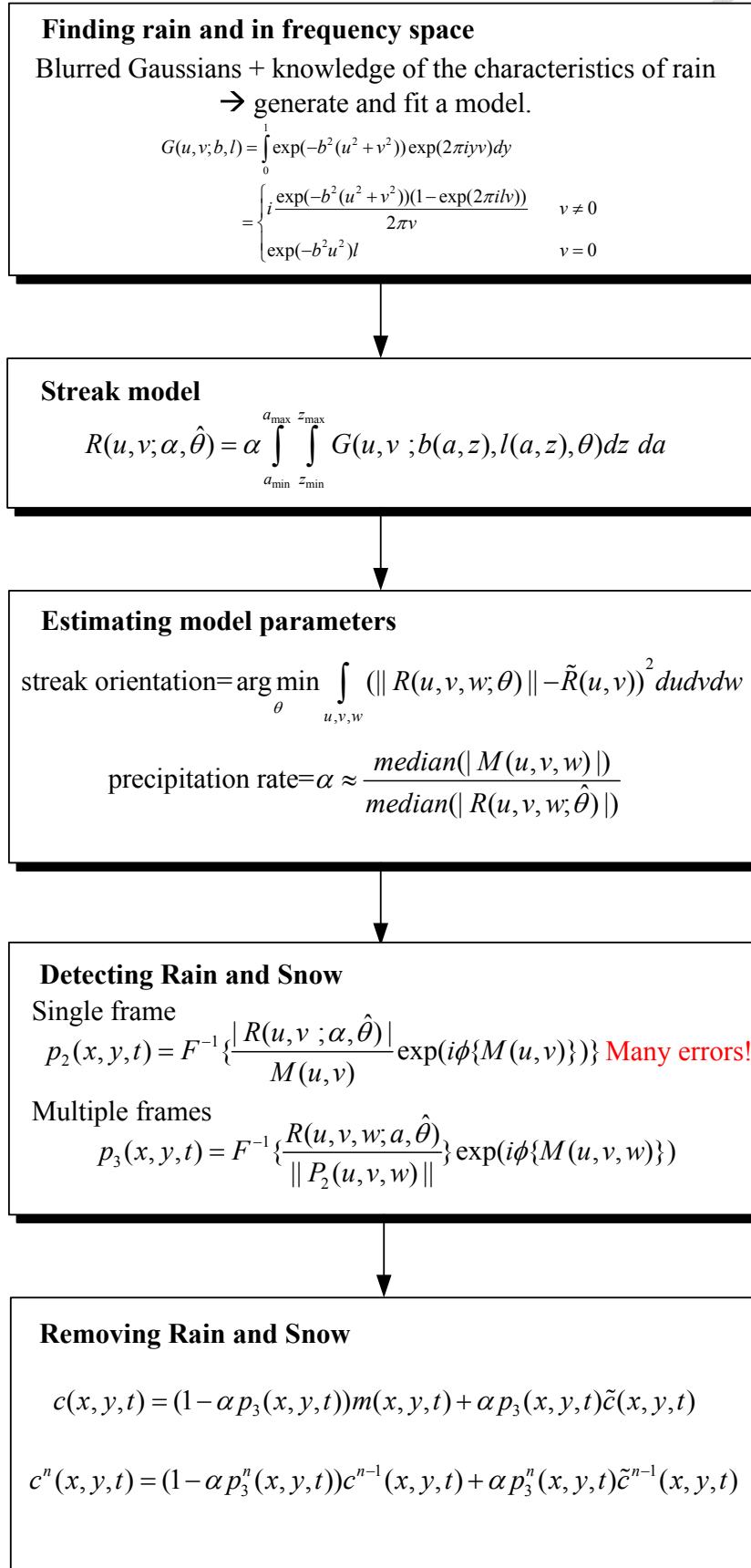
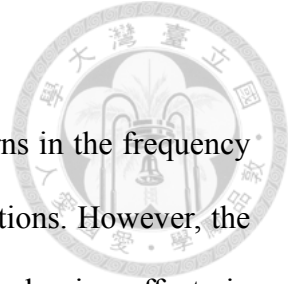


Fig. 4.16 Flow chart of the paper proposed by Barnum et al. [7].

4.5.2 Advantage and Disadvantage

The algorithm [7] can be fast analyzed with the repeated patterns in the frequency domain and is effective for videos under both scene and camera motions. However, the frequency variation among the frames do not always cause visual pleasing effects in image space. Although, the segmentation accuracy surpasses any image space method developed so far, the removal results do not always have the best appearance. Besides, the result of processing the single image by the algorithm is not quite better and too complicated to reference for the beginner.





Chapter 5 Proposed Method of Rain/Snow Removal in Single Image



5.1 Introduction

The existing derained and desnow methods usually remove other objects detail, blur the image, and need much more computation time. Thus, we propose a rain or snow removal method, which not only has low computation time but also get a high quality result. In [4], Xu et al. uses the guided filter to remove rain or snow, but it still simultaneously removes other image detail as well. In [5], Knag et al. proposed a single-image rain streak removal algorithm based on the morphological component analysis. The performance of their algorithm depends on the clustering of basis vectors. When the clustering is not effective, their algorithm may erase textures, as well as rain streaks, and yield visual artifacts in a restored image. This method [5] requires huge computation (i.e., caused by the dictionary learning) for detection and removal. By contrast, our proposed method uses the properties in spatially and temporally of rain and snow to detect, which is intuitive and simple, and then removes rain by conjugate gradient for Lagrangian inpainting. Therefore, the computational complexity is substantial reduction and can obtain an appealing result for our proposed method. Fig. 5.1 shows the flow chart of our proposed method.

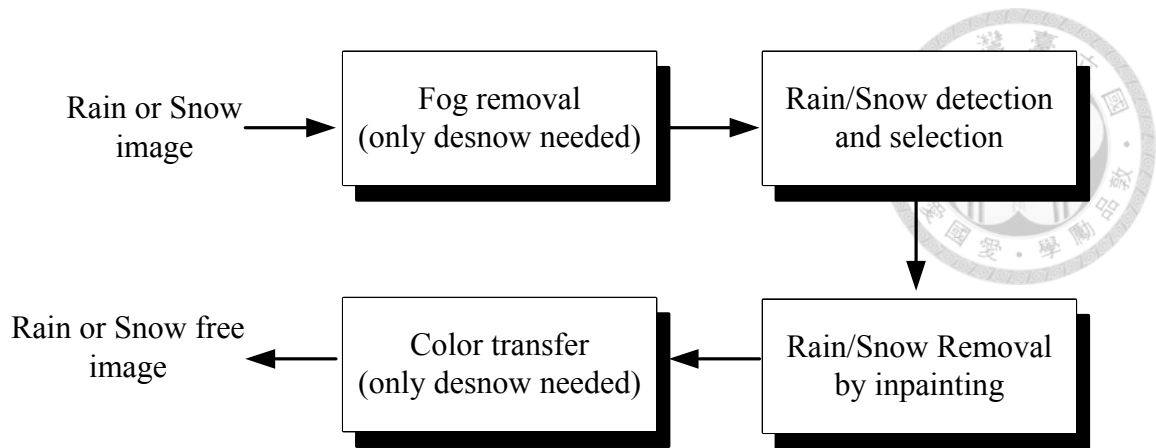


Fig. 5.1 Flow chart of the proposed method.

5.2 Proposed Method

5.2.1 Fog Removal Pre-Processing

In the case of the dynamic weather, individual particles are visible in the image (0.1–10mm) and the aggregate scattering models used for steady conditions are not applicable in here such as rain, snow, and hail. However, the visual effects of raindrops and snow are very weak and appear as fog when raindrops and snow are very far from the camera. In order to overcome the problem, we pre-process the proposed dehazing method mentioned in Chapter 3. Fig. 5.2 shows the result of the fog removal pre-processing.

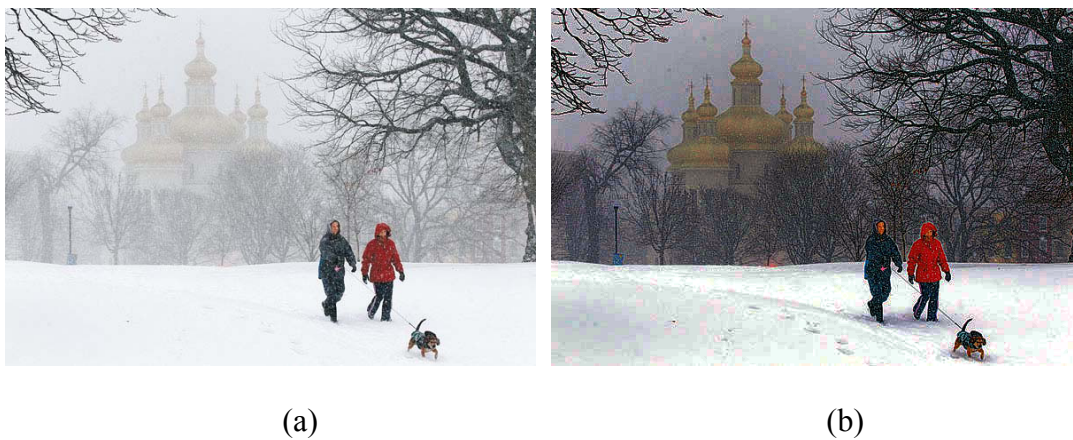


Fig. 5.2 Result of the fog removal pre-processing. (a) Input snow image. (b) Results after applying fog removal pre-processing.

5.2.2 Rain/Snow Detection and Selection Process

In the case of the rain presents on the window surface, raindrops located against a clear area (generally the sky) are not perceptible even by a human expert as shown in Fig 5.3. Therefore, the first step is separated into dark and clear regions, but we only apply the detection methods in the darker region. Dark areas are extracted by a combination of morphological operations as following process:

Step 1: Erosion of the original image by a disk of a diameter of 20 pixels as a structuring element.

Step 2: Morphological reconstruction [59] of the original image with the eroded image as a mask.

Step 3: Application of step1 and 2 on the complement of the reconstructed image.

Step 4: Segmentation of the result using Ostu's method [60].

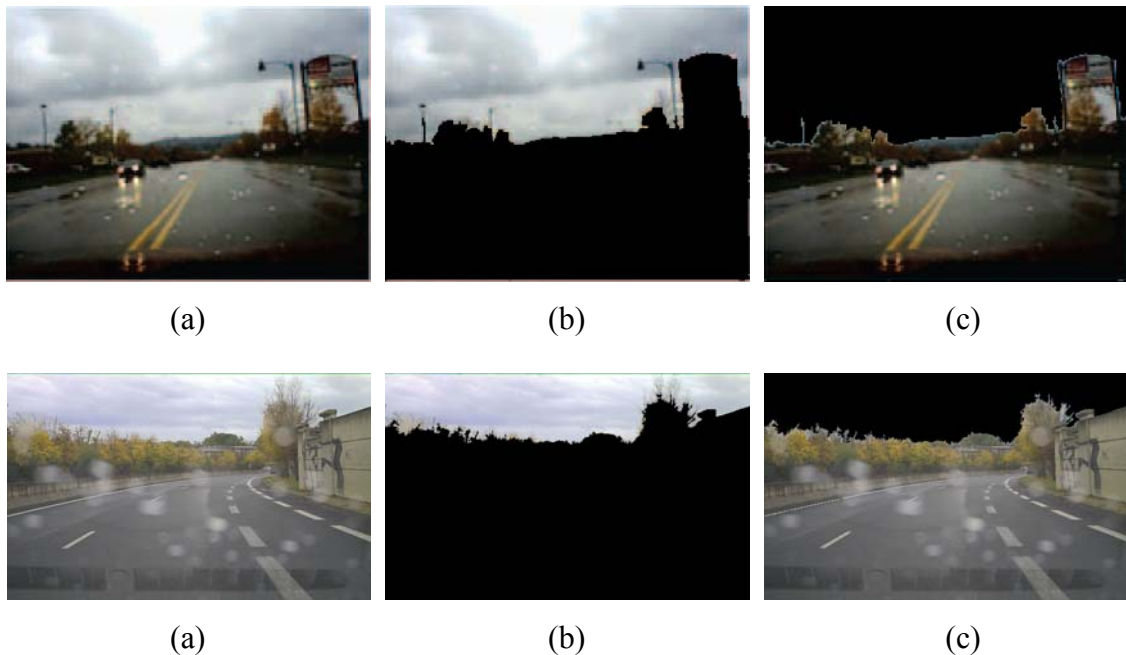


Fig. 5.3 Segmentation of dark versus clear region. (a) Original image. (a) The sky region. (b) The dark region (raindrops are visible in this region).

In natural property, the rain and snow are brighter than background. Thus, we exploit three properties of rain and snow. First, a rain or snow pixel tends to be brighter than a rain-free or snow-free pixel. Second, pixels in rain and snow have similar color. Third, the power spectral distribution of rain and snow “streaks” in the 2D frequency space is elliptical and oriented with certain direction, this ellipse is the sum of all the rain or snow streaks, but snow ”flakes” is random and not orientated to any directions, as show in Fig.5.4. Hence, we need different model to process.

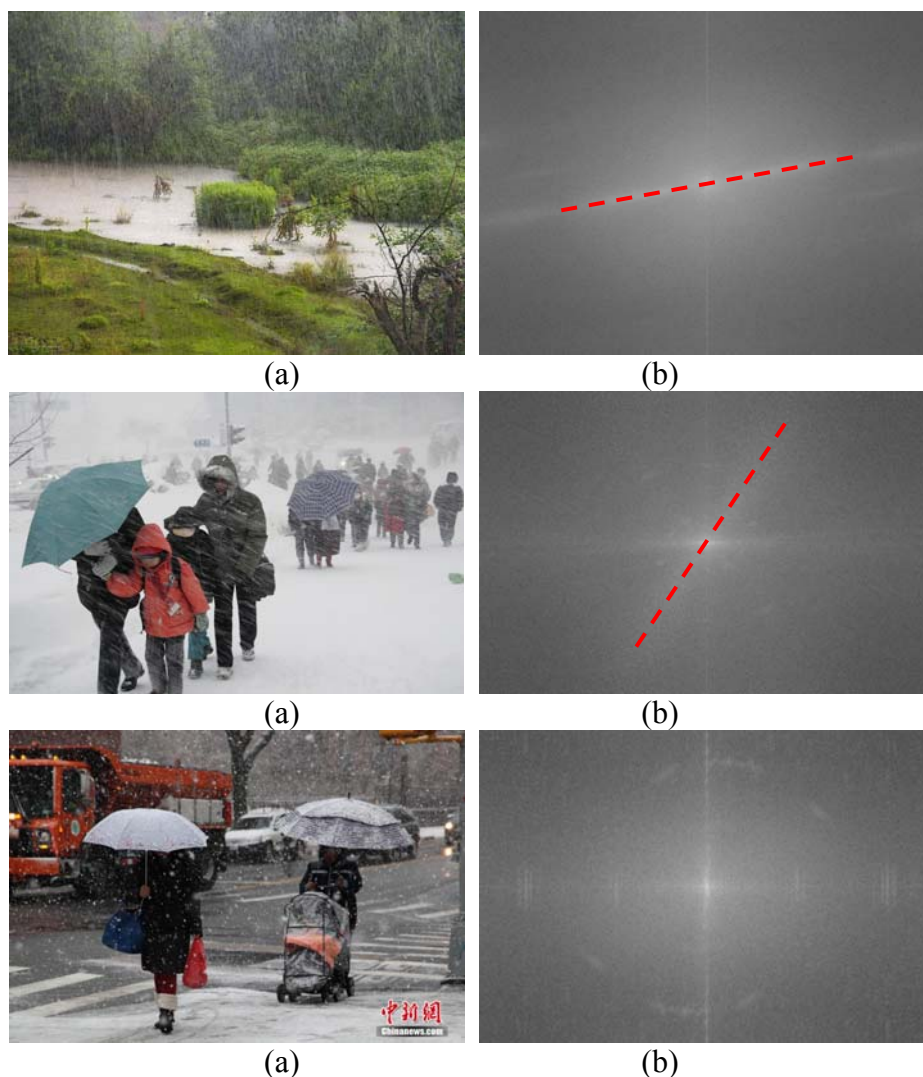
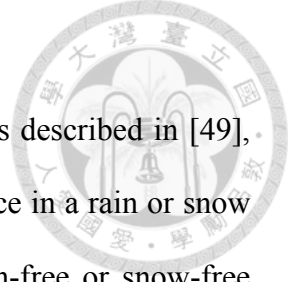


Fig. 5.4 Power spectral distributions of rain and snow images in frequency domain. (a) The original images. (b) Its two dimensional Fourier transform.



The first property is related to the intensity levels of pixels, As described in [49], when a pixel has ever been covered by rain, the average of luminance in a rain or snow region A is higher than the average of luminance for those in rain-free or snow-free region B in general. Thus, we design the following process to detect rain and snow effectively:

Step 1: Calculate the average intensity of the pixel p in a single image, where N is the number of pixels.

$$A_1 = \left(\frac{1}{N} \sum_{i=1}^N p_i \right) \quad (5.1)$$

Step 2: Determine the threshold TH_1 . X is a parameter and may be various in different cases of rain.

$$TH_1 = A_1 \cdot X\% \quad (5.2)$$

Step 3: Determine whether the pixel p is larger than the threshold (TH_1). If the pixel p is larger than the threshold (TH_1), it is regarded as the rain or snow pixel; otherwise, it is regarded as the rain-free or snow-free region. According to the experiments, we get the following conclusion: if X is smaller we can get more candidate rain or snow pixel, and vice versa.

$$\begin{cases} p_i > TH_1, & \text{rain or snow pixel} \\ else & \text{, background (rain-free or snow free) pixel} \end{cases} \quad (5.3)$$

Fig 5.5 shows the different threshold with the candidate rain pixels. We can simply and readily get a preliminary rain detection results through the rain detection process (see Fig. 5.6) and then save them as a binary field (1 & 0) to represent the rain (snow) and non-rain (non-snow) pixel.

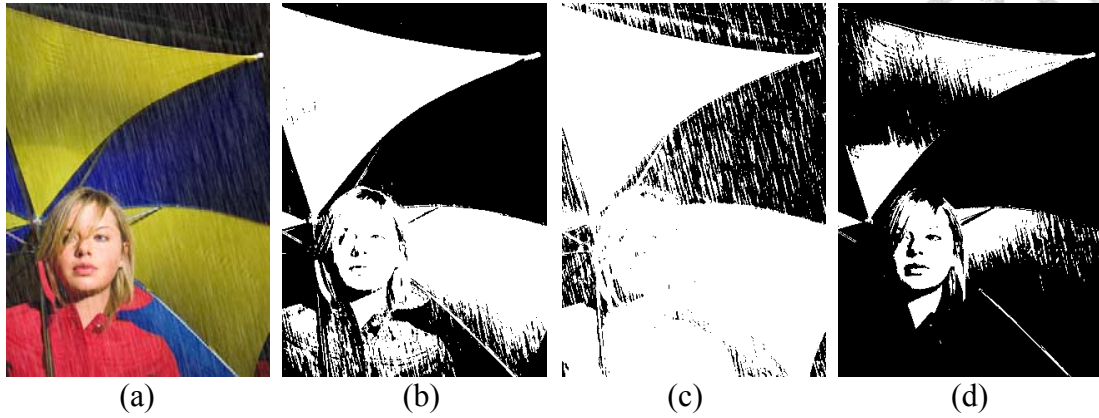


Fig. 5.5 The possible rain candidates with different threshold (initial binary field). (a) Input rain image. (b) The possible rain candidates (TH_1 is set to A). (c) The possible rain candidates (TH_1 is set to smaller than A). (d) The possible rain candidates (TH_1 is set to larger than A).

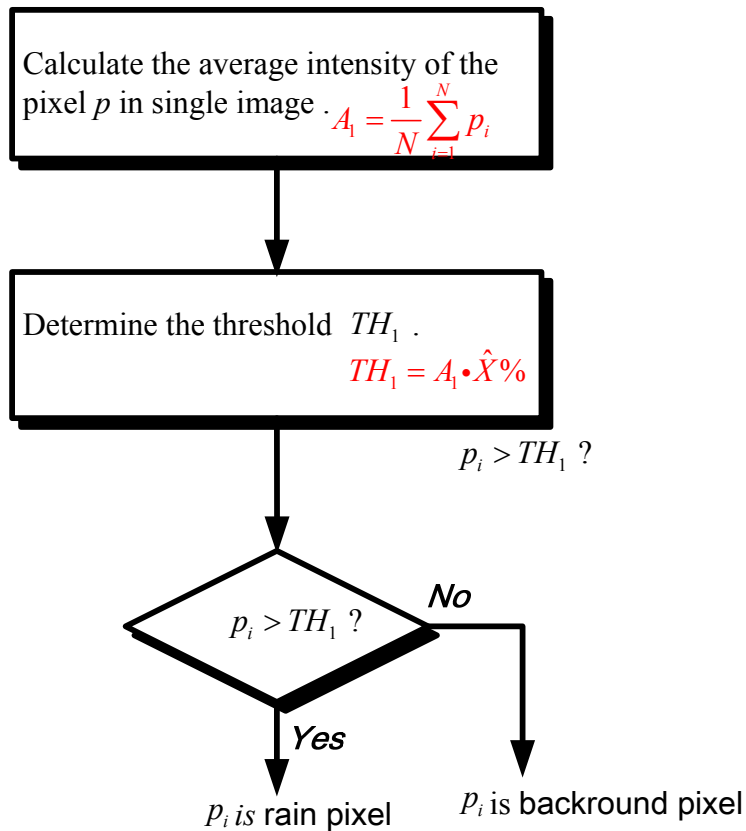


Fig. 5.6 Flow chart of the rain or snow detection process with first property.

The second property is related to the pixels in rain or snow which have similar color. According to the chromatic property, the amounts of change ΔR , ΔG , and ΔB for pixels covered by rain and snow are approximately the same (actual rain and snow pixel). When a pixel has ever been covered with the rain or snow, the peak values can be obtained in its RGB component histogram. Although there can be more than one local maximum, there is only one global maximum (peak). The global maximum can be obtained in its histogram distribution of RGB components. A pixel has ever been covered by rain or snow, and the RGB components in a rain or snow region A are close to its global maximum. Thus, we design the following process to detect rain effectively

Method 1:

Step 1: Draw the histogram distribution of the RGB components, as show in Fig 5.7.

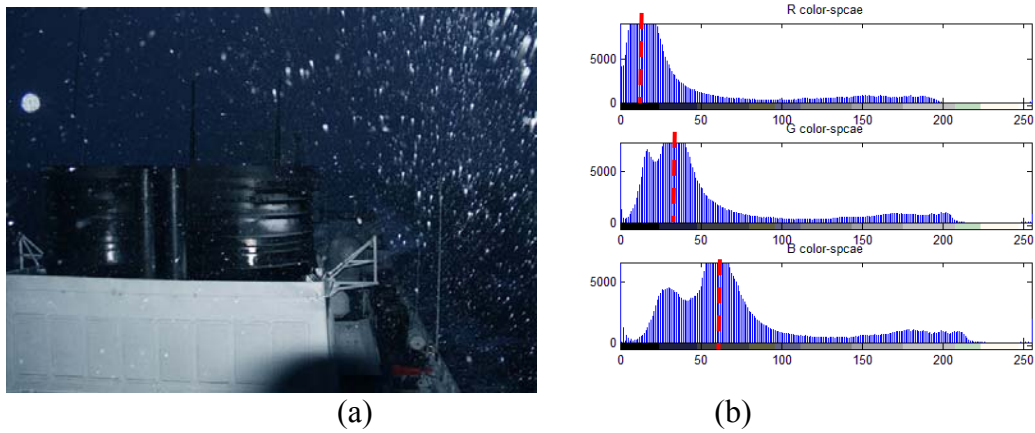
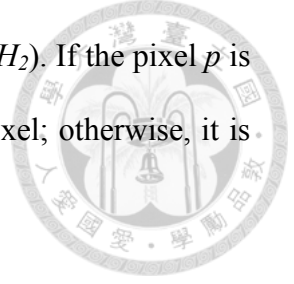


Fig. 5.7 The histogram distribution of the RGB components. (a) The original snow image. (b) Its histogram distribution of RGB components.

Step 2: Calculate the average pixel index \tilde{x} from the global maximum in the RGB components, where x is the pixel index and H is the histogram operator.

$$\tilde{x} = \frac{1}{3} \sum_{c \in \{r, g, b\}} \max [H^c(x)] \tag{5.4}$$



Step 3: Determine whether the pixel p is larger than the threshold (TH_2). If the pixel p is larger than the threshold (TH_2), it is regarded as the rain or snow pixel; otherwise, it is regarded as the rain-free or snow-free region.

$$\begin{cases} p > TH_2 & , \text{rain or snow pixel} \\ else & , \text{background pixel} \end{cases} \quad (5.5)$$

Method 2: It is similar to the process of first property.

Step 1: Calculate the mean R , G , and B values of the pixels p in the image, where N is the number of pixels.

$$A_2^c = \left(\frac{1}{N} \sum_{\substack{i=1 \\ c \in \{r, g, b\}}}^N p_i^c \right) \quad (5.6)$$

Step 2: Determine the threshold TH_3 .

$$TH_3 = \min_{c \in \{r, g, b\}} A_2^c \quad (5.7)$$

Step 3: Determine whether the pixel p in the RGB component are larger than the threshold (TH_3). If the pixel p is larger than the threshold (TH_3), it is regarded as the rain or snow pixel; otherwise, it is regarded as the rain-free or snow-free region. According to the experiments, we get the following conclusion: if X is smaller we can get more candidate rain or snow pixel, and vice versa.

$$\begin{cases} p_i > TH_3 & , \text{rain or snow pixel} \\ else & , \text{background (rain-free or snow free) pixel} \end{cases} \quad (5.8)$$

We can simply and readily get a preliminary rain detection results through the rain detection process (see Fig. 5.8) and then save them as a binary field (1 & 0) to represent the rain (snow) and non-rain (non-snow) pixel. Fig. 5.9 illustrates three examples. Fig.

5.9 (a) highlights regions in the video in which pixel colors are examined. Fig. 5.9 (b) shows the mean R , G , and B values of the pixels in the selected regions, and Fig. 5.9 (c) shows the corresponding means and standard deviations of ΔR , ΔG , and ΔB . These examples show that the mean ΔR , ΔG , and ΔB are indeed different and related to the mean R , G , and B intensities.

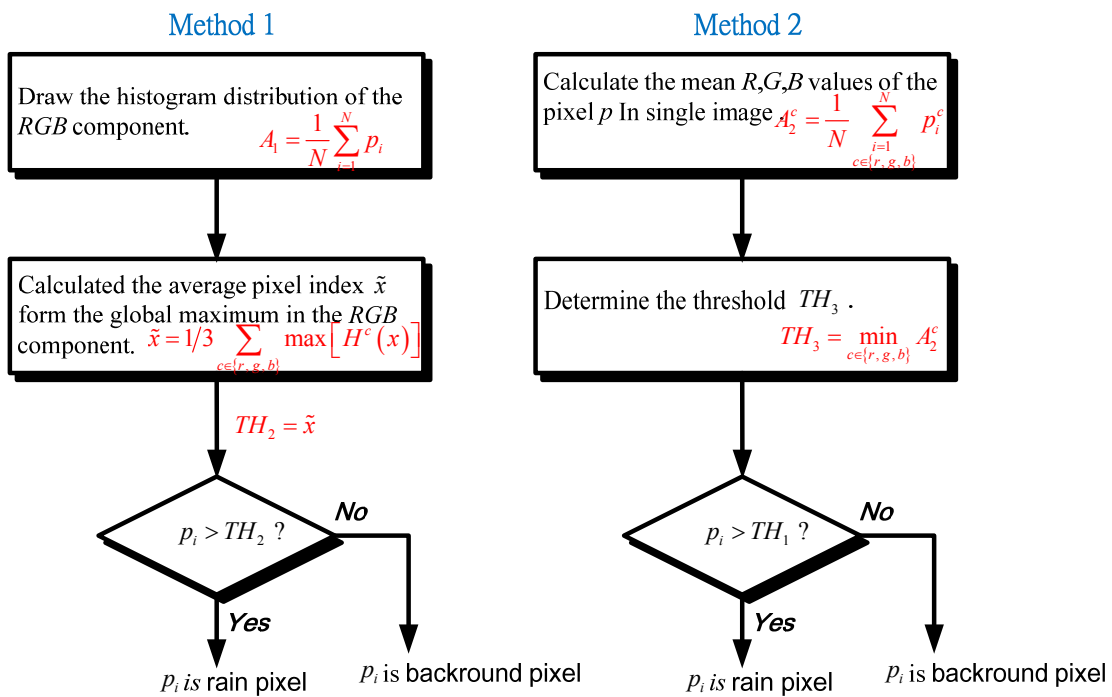


Fig. 5.8 Flow chart of the rain or snow detection process with second property.

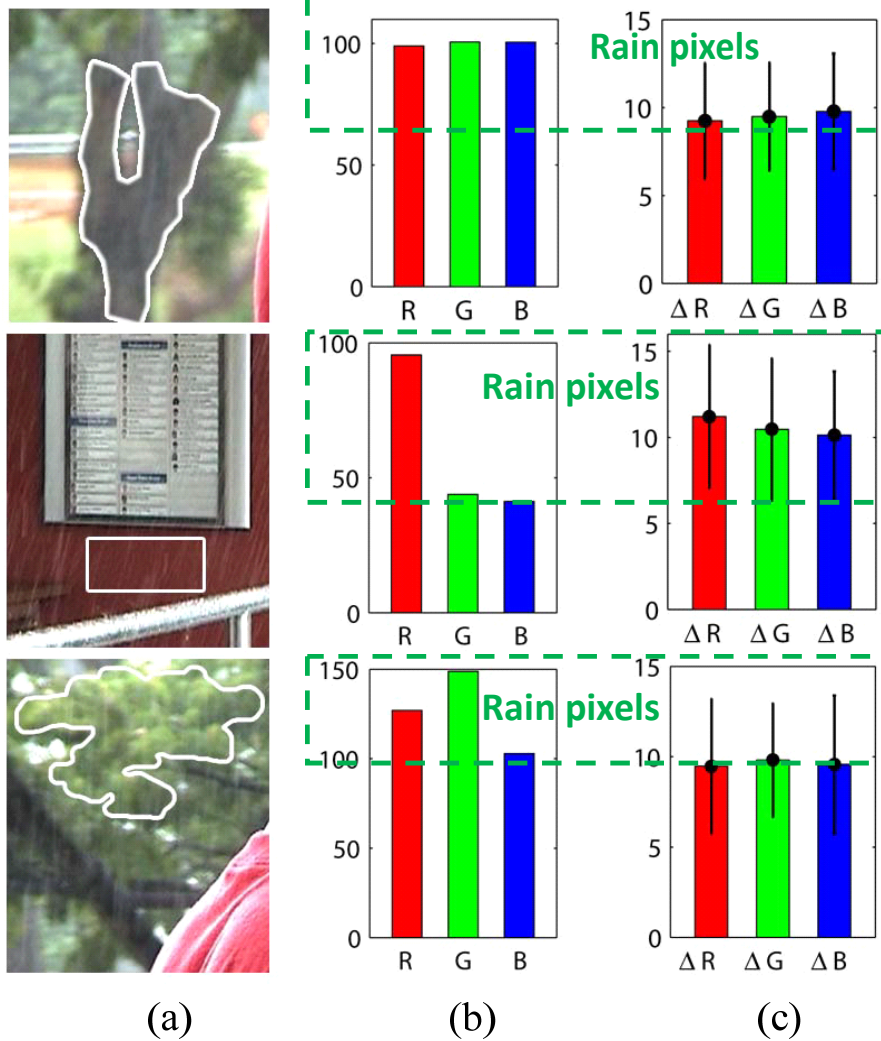


Fig. 5.9 (a) The regions selected for investigation. (b) The mean R , G , and B values of the pixels in the selected regions. (c) The corresponding means the standard deviation of ΔR , ΔG , and ΔB .

The third property is related to the power spectral distribution of rain and snow “streaks” in the 2D frequency space is elliptical and oriented with certain direction, this ellipse is the sum of all the rain or snow streaks, but snow “flakes” is random and not orientated to any directions. We design the following process to detect rain or snow effectively

Step 1: The properties of rain and snow are high-intensity and low-saturation. Thus, we

exploit these unique properties of rain and snow to detect the candidates of rain and snow pixel. For the purpose of getting the rain or snow initial candidate ($C_{initial}$) pixel of the snow or rain, we merge the saturation layer (S) in HSI color model and Intensity layer (I) in color model as

$$C_{initial} = (1 - S) \cdot I \quad (5.9)$$

Step 2: Use a high pass filter to enhance the rain or snow candidates by multiplying the high pass filter and the rain or snow candidates in the frequency domain. The High pass filter can be expressed as

$$HF[\bullet] = 1 - e^{-r/\sigma} \quad (5.10)$$

where r is the distance between the core of the image and the pixel p , σ is the coefficient which decides the stop band of the filter.

Step 3: Use the orientation filter to separate the rain (snow) streak or background object. Rain or snow streaks generally fall in almost the same direction, so only one θ_p is needed. However, snowflake is not.

Step 4: Determine whether the rotation angle in pixel p is in the constrained threshold α . If the pixel p is smaller than the constrained threshold (α), it is regarded as the rain or snow “streak” pixel; otherwise, it is regarded as the background region.

$$\left| \theta_p - \frac{\pi}{2} \right| < \alpha \quad (5.11)$$

We can simply and readily get a preliminary rain detection results through the rain detection process (see Fig. 5.10) and then save them as a binary field (1 & 0) to represent the rain (snow) and non-rain (non-snow) pixel.

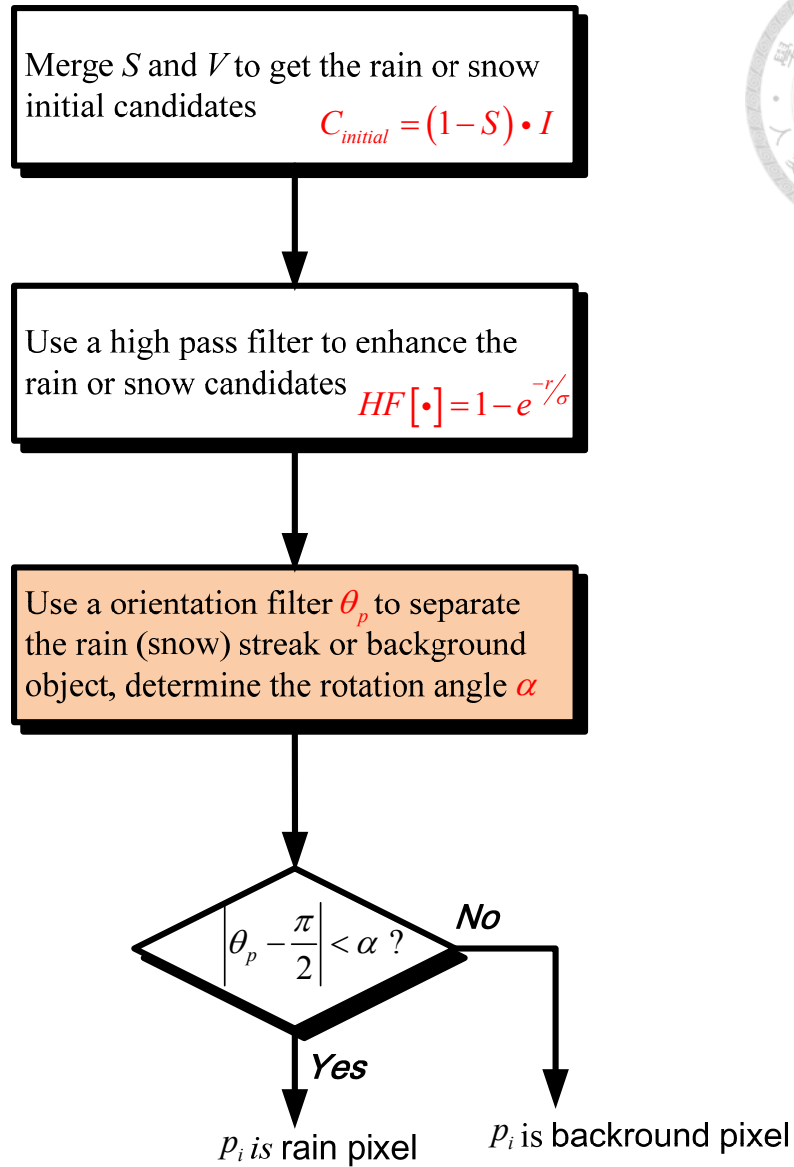


Fig. 5.10 Flow chart of the rain or snow detection process with third property.

Above all, there may be a problem caused by other brighter subjects in the scene (e.g. white car, accumulated snow) so that the rain or snow detecting result is not quite perfect. Hence, we add the following restrict to exclude the above situation: the actual number of pixels in the region R_p of rain or snow will smaller than a threshold (TH_4) as

$$R_p < TH_4 \quad (5.12)$$

We can find that other brighter subjects have been removed as illustrated in Fig 5.11.

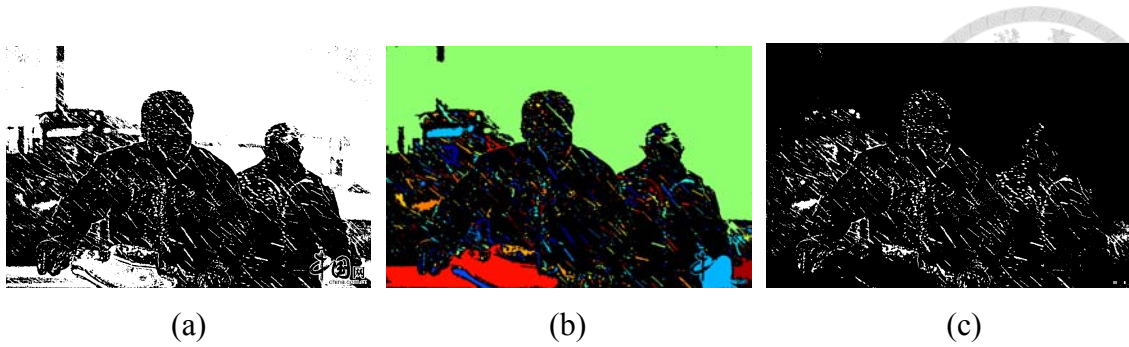


Fig. 5.11 Result of the identification of snow streaks by our proposed method. (a) All potential snow streaks (initial snow binary map). (a) All potential snow streaks (initial snow jet colormap). (b) Initial snow mask refined by area restrict.

Besides, some surrounding rain pixels have a chance to be undetected because of their low intensity or unfocused, when we process the single rain or snow (e.g. [61]-[64]). In order to avoid this, we extend the outer contour of the detection regions. We assume that a rain or snow streak column (i.e., (4, 5), (5, 5), (6, 5)) is detected, after that we extend this column into both side columns to produce a block-matrix as in Fig. 5.12. Finally we combine the binary field (1 & 0) from the properties to get the precise rain or snow pixel. We assume that two binary fields are detected from the snow image, and then we combine them to get the precise one as in Fig. 5.13. Further, we apply the proposed rain removal process to remove the rain from the image.

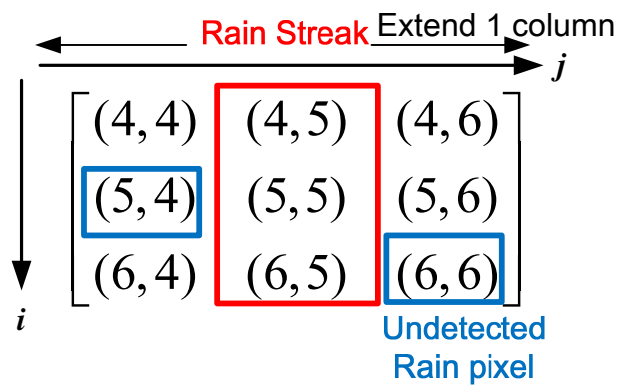


Fig. 5.12 Schematic diagram of rain or snow extending.

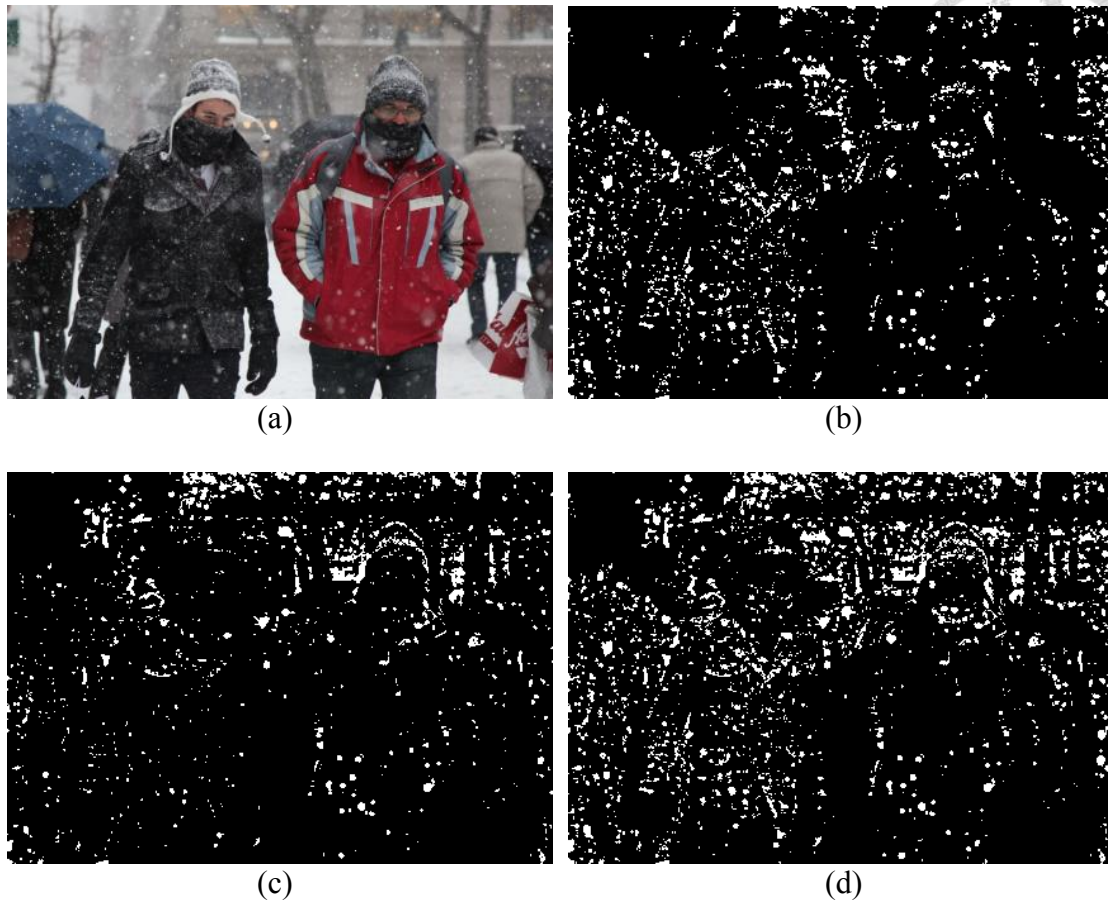


Fig. 5.13 The result of combination process. (a) The original snow image. (b) The first binary field. (c) The second binary field. (d) The combined binary field.

5.2.3 Rain/Snow Removal Process

Rain or snow removal in single image is similar to image inpainting, which tries to recover occluded objects in image, so we remove rain or snow by conjugate gradient for Lagrangian inpainting. It can be able to replace with other inpainting schemes (e.g. [65], [66]). The conjugate gradient method is an iterative method that is tailored to solve large symmetric linear systems $Ax = b$. We consider here the inpainting problem, which corresponds to the interpolation of missing data in the image. We define a binary field $M \in \mathbb{R}^N$ where $M_i = 1$ if the pixel indexed by i is missing,

and $M_i = 0$ otherwise. We consider here random missing pixel, and a large missing region in the upper left corner. Define the degradation operator $\Phi: \mathbb{R}^N \rightarrow \mathbb{R}^N$, that corresponds to the masking with M_i , i.e. a diagonal operator $\Phi = \text{diag}_i(M_i)$. Compute the observation $y = \Phi(x)$.

To perform the recovery of an image from the damaged observations y , we aim at finding an image x that agrees as much with the measurements, i.e. $\Phi x \approx y$, but at the same time is smooth. We measure the smoothness using the norm of the gradient $\|\nabla x\|^2$, which corresponds to a discret Sobolev norm. This leads us to consider the following quadratic minimization problem

$$\min_{x \in \mathbb{R}^N} F(x) = \|y - \Phi x\|^2 + \lambda \|\nabla x\|^2 \quad (5.13)$$

This problem has a unique solution if $\ker(\Phi) \cap \ker(\nabla) = \{0\}$. This condition holds in our case since $\ker(\nabla)$ is the set of constant images. The solution can be obtained by solving the following linear system:

$$Ax = b \quad \text{where} \begin{cases} A = \Phi^* \Phi - \lambda \Delta \\ b = \Phi^* y \end{cases} \quad (5.14)$$

Here we can remark that for the inpainting problem, $\Phi^* \Phi = \Phi$ and $\Phi^* y = y$. The value of the parameter λ should be small. Fig. 5.14 shows the procession of the image inpainting.

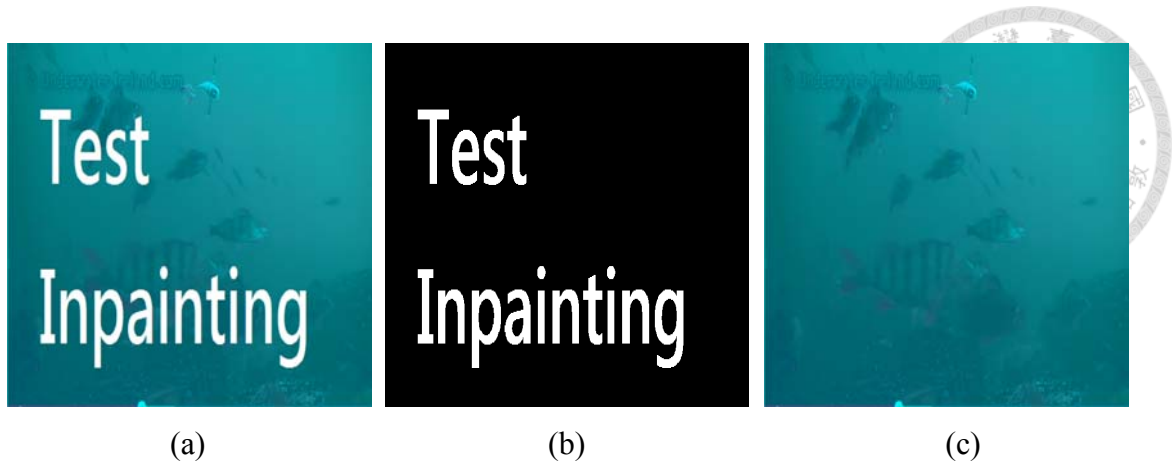


Fig. 5.14 Image inpainting. (a) The original input image. (b) The binary mask of missing area ($M_i = 1$ defines the pixel indexed by i is missing). (c) The image after inpainting.

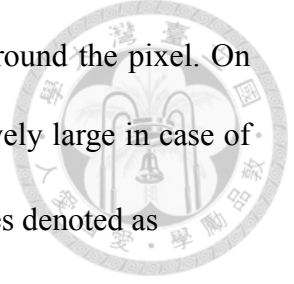
5.2.4 Impulse Noise Removal Process

The image after rain or snow removal, it may cause the non-uniform color distribution on the edge of blocks. We regard this phenomenon as impulse noises and then remove them by applying the fuzzy random impulse reduction method [67]. The detection method is a subunits that is used to define the impulse noise pixel. The subunit investigates the neighborhood around a pixel to conclude if the pixel can be considered as impulse noise or not.

We consider a two dimensional image denoted as A and observe the elements in a $(2N + 1) \times (2N + 1)$ with $N \geq 1$ window centered around $A(i, j)$. Then we calculate the mean differences in the window denote as

$$g(i, j) = \frac{\sum_{k=-N}^N \sum_{l=-N}^N |A(i+k, j+l) - A(i, j)|}{(2N+1)^2 - 1} \quad (5.15)$$

Corrupted impulse noise pixels generally cause large $g(i, j)$ values, because impulse



noise pixels normally occur as outliers in a small neighborhood around the pixel. On the other hand we also found that the $g(i, j)$ -value could be relatively large in case of an edge pixel. Therefore we have considered the following two values denoted as

$$obs_1(i, j) = \sum_{k=-K}^K \sum_{l=-K}^K g(i+k, j+l) / (2K+1)^2 \quad (5.16)$$

$$obs_2(i, j) = g(i, j)$$

If $obs_1(i, j)$ and $obs_2(i, j)$ are large, then the pixel can be considered as an edge pixel instead of an impulse noise. If $obs_1(i, j)$ and $obs_2(i, j)$ are similar, then we conclude the pixel is noise free. If the difference between $obs_1(i, j)$ and $obs_2(i, j)$ is large, then we conclude the pixel is noise. Then we implement the following fuzzy rule:

Fuzzy Rule: Define a central pixel $A(i, j)$ is corrupted with impulse noise

IF $|obs_1(i, j) - obs_2(i, j)|$ is *large*

THEN the central pixel $A(i, j)$ is an impulse noise pixel.

In this fuzzy rule, large can be represented as a fuzzy set [68]. A fuzzy set in turn can be represented by a membership function. An example of a membership function LARGE (for the corresponding fuzzy set *large*), which is entitled as μ_{large} , is pictured in Fig. 5.15. From such functions we can derive membership degrees. If the difference $|obs_1(i, j) - obs_2(i, j)|$ for example has a membership degree one (or zero) in the fuzzy set *large*, it means that this difference is considered as large (or not large) for sure. Membership degrees between zero and one indicate that we do not know for sure if such difference is large or not, so that the difference is large to a certain degree. In Fig. 5.14 we need to determine two important parameters a and b . The parameter a corresponds to the $g(i+k, j+l)$ coming from the most homogeneous region around $A(i, j)$, which

should correspond to the region with the smallest amount of impulse noise pixels is denoted as

$$a(i, j) = \min_{k, l \in \{-N, \dots, N\}} (g(i+k, j+l)) \quad (5.17)$$

Experimental results have shown that the best choice for parameter $b(i, j)$ is

$b(i, j) = a(i, j) + 0.2a(i, j)$, i.e. the larger the parameter a , the larger the uncertainty

interval $[a, b]$ should be.

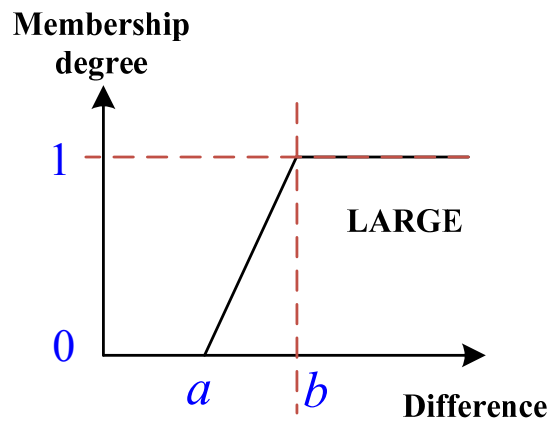


Fig. 5.15 The membership function μ_{large}

The outputs of the detection method are the membership degree in the fuzzy set impulse noise for each pixel separately. The membership function that represents the fuzzy set is defined as μ_{impulse} . The corresponding membership degree $\in [0,1]$ are calculated using Fuzzy Rule. The activation degree of the rule is used to determine the membership degree μ_{impulse} , $\mu_{\text{impulse}} = \mu_{\text{large}} |obs_1(i, j) - obs_2(i, j)|$. Finally, we apply the proposed removal process (i.e., mentioned in sub-section 5.2.3) to remove the impulse from the image. Fig. 5.16 shows the impulse noise detection result.

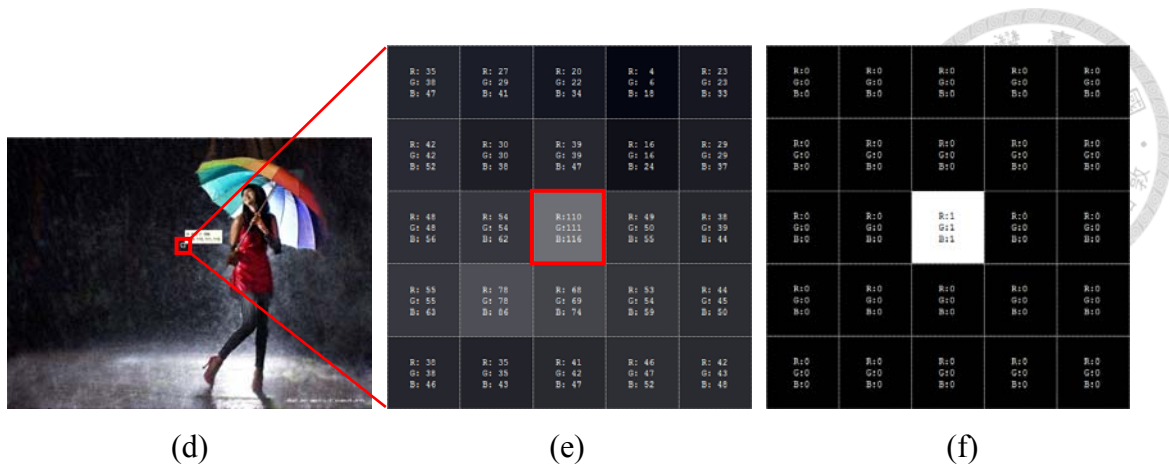


Fig. 5.16 Impulse noise detection result. (a) The image after rain removal. (b) Zoom-in patch of (a). (c) The detected result of impulse noise.

5.2.5 Color Transfer Post-processing

With the snow-free image can be obtained by section 5.2.3 but has higher dynamic than the non-dehazed one. Color mapping should be done as essential step to allow the visual comparison of the resulting images obtained by our proposed method as well as for comparison with the non-pre-processing image. Balancing the two comparisons, we adopt the snow-free image and the snow-free image without fog removal pre-processing image to obtain the composite information and use color transfer model [33] to obtain a linear color mapping on the resulting images. After this paragraph, we will introduce the basic concept of color transfer model. The multiscale retinex with color restoration (MSRCR) [36] is a visibility restoration algorithm which makes the recovered image have wealthy color information and color distortion. MSRCR is applied to the original image $I(x)$ to obtain $R(x)$ and the bottom third part of $I(x)$ is regarded as less fog influenced areas. According to the concepts, we combine $R(x)$ with the bottom third part of $I(x)$ by a weight σ to obtain the source image (non fog removal pre-processing image). The rain/snow-free image $J(x)$ is the target image. Color transfer model is a

linear transformation from the source image to the target image based on the simplest statistics of two images' global color distributions:

$$T(x) = [(1-\sigma)a_R + \sigma a_I] + \frac{(1-\sigma)d_R + \sigma d_I}{d_J} [J(x) - a_J] \quad (5.18)$$

where $[(1-\sigma)a_R + \sigma a_I, (1-\sigma)d_R + \sigma d_I]$, and $[a_J, d_J]$ are the mean and standard deviation of the source and target images in the $l\alpha\beta$ color space, respectively. The weight σ balances the effects of two images and is set as 0.5. The final obtained image $T(x)$ will be with suitable visual appearance.

A fast and effective technique for color transfer between images has been proposed by Reinhard et al.[33]. This method changes the color characteristics of the source image I from the target image I_t by statistic correction. The basic concept of the proposed method is to decorrelate color space so that an uncorrelated orthogonal color space can be identified between the axes. First, we process a conversion from RGB to XYZ tristimulus values and convert XYZ space to LMS space. Further, the resulting of these two converted matrices between RGB and LMS cone space can be combined as

$$\begin{bmatrix} L \\ M \\ S \end{bmatrix} = \begin{bmatrix} 0.3811 & 0.5783 & 0.0402 \\ 0.1967 & 0.7244 & 0.0782 \\ 0.0241 & 0.1228 & 0.8444 \end{bmatrix} \begin{bmatrix} R \\ G \\ B \end{bmatrix}. \quad (5.19)$$

Apparently, the data in this color space shows a great deal of skews and the skews must be eliminated. We convert the data to logarithmic space for eliminating these skews by

$$\begin{cases} \mathbf{L} = \log L \\ \mathbf{M} = \log M. \\ \mathbf{S} = \log S \end{cases} \quad (5.20)$$

By avoiding unwanted cross effect and treating the three color channels separately, Reinhard et al. [33] uses the $l\alpha\beta$ color space for ensuring each channel maximal

uncorrelated and represents as the following transform

$$\begin{bmatrix} 1 \\ \alpha \\ \beta \end{bmatrix} = \begin{bmatrix} \frac{1}{\sqrt{3}} & 0 & 0 \\ 0 & \frac{1}{\sqrt{6}} & 0 \\ 0 & 0 & \frac{1}{\sqrt{2}} \end{bmatrix} \begin{bmatrix} 1 & 1 & 1 \\ 1 & 1 & -2 \\ 1 & -1 & 0 \end{bmatrix} \begin{bmatrix} \mathbf{L} \\ \mathbf{M} \\ \mathbf{S} \end{bmatrix}. \quad (5.21)$$



After transferring the color space from RGB to $l\alpha\beta$, each channel of the source image I subtracts the mean of itself for every pixel as

$$\begin{cases} l^* = l - \langle l \rangle \\ \alpha^* = \alpha - \langle \alpha \rangle \\ \beta^* = \beta - \langle \beta \rangle \end{cases} \quad (5.22)$$

where l represents an achromatic channel, α and β are chromatic yellow-blue and red-green opponent channels, and $\langle \rangle$ is the calculation of mean. Then, the difference of each channel in (5.11) is scaled by the standard deviations of target image (σ_t) and source image (σ_s), respectively. Besides, the scaled data must add the mean of the target image (I_t) [33]:

$$\begin{cases} l' = \frac{\sigma_t^l}{\sigma_s^l} l^* + \langle l \rangle \\ \alpha' = \frac{\sigma_t^\alpha}{\sigma_s^\alpha} \alpha^* + \langle \alpha \rangle \\ \beta' = \frac{\sigma_t^\beta}{\sigma_s^\beta} \beta^* + \langle \beta \rangle \end{cases} \quad (5.23)$$

After this, the source image I has the average color tone and luminance from the target image, and the result is converted back to $R'G'B'$ color space for acquiring the output image I' by

$$\begin{bmatrix} R' \\ G' \\ B' \end{bmatrix} = \begin{bmatrix} 0.5773 & 0.2621 & 11.3918 \\ 0.5773 & 0.6071 & -5.0905 \\ 0.5833 & -1.0628 & 0.4152 \end{bmatrix} \begin{bmatrix} I' \\ \alpha' \\ \beta' \end{bmatrix}. \quad (5.24)$$



In Fig. 5.17, it is shown that the transfer process of snow images by using the proposed method.

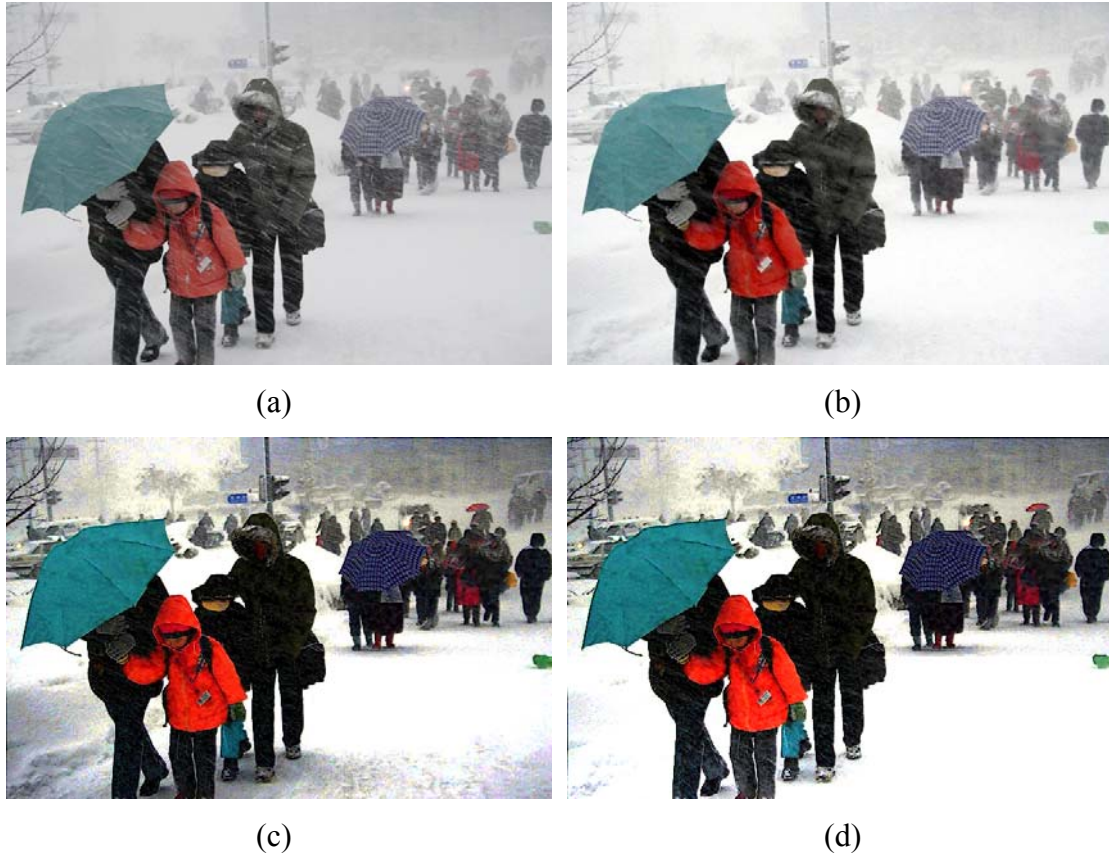


Fig. 5.17 Transfer process of snow images by using the proposed method. (a) The original snow image. (b) The result of snow removal. (c) The result of snow removal is further used to haze remove by our proposed method. (d) The result after the color transfer mapping.

5.3 Experimental Results

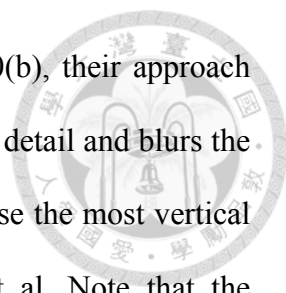
The experiment is separated into 4 cases: *Case 1*: the input rainy images. *Case 2*: the input snow streak images. *Case 3*: the input snow flake images. *Case 4*: the rain and

snow in video sequences with dynamic cases. *Case 5*: the rain presents on the window surface.

In *Case 1*, the input image is used the proposed method to remove rain. The rain removal results are shown in Fig. 5.18. Compare with our method, Kang et al. [5] and Kim et al. [6] in Fig. 5.18, and it shows that the background textures is be distorted because the most vertical patterns is be regarded as rain streaks in the result by Kang et al. Note that the background texture patterns in Fig. 5.18(b) are not contained in the original image in Fig. 5.18(a). In the image, rain streaks are removed and original textures are preserved by Kim et al. approach. But the defocused streaks and streaks on bright backgrounds show very small intensity changes so that they are hard to detect as shown in Fig. 5.18(c). In contrast, we see that most rain streaks in all test images are successfully removed, and original textures are faithfully preserved at the same time by the proposed algorithm. The reason why the result is caused is that the proposed algorithm selectively applies more properties in spatial and frequency domain.

In Fig. 5.19, the proposed, Xu et al. [4], and Kang et al. [5] approaches are compared, and it shows that the result of the Xu et al. approach removes more rain, but it still simultaneously removes other image detail and blurs the image as shown in Fig 5.19(b). The background textures is be distorted because the most vertical patterns is be regarded as rain streaks in the result by Kang et al. Note that the background texture patterns in Fig. 5.19(c) are not contained in the original image in Fig. 5.19(a). In contrast, we see that most rain streaks in all test images are successfully removed, and original textures are faithfully preserved at the same time by the proposed algorithm. The reason why the result is caused is that the proposed algorithm selectively applies more properties in spatial and frequency domain.

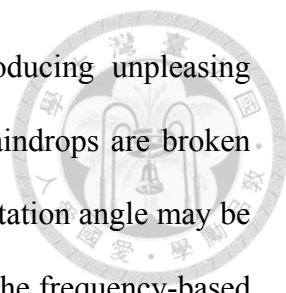
In *Case 2*, the input image is snow “streak” removed by applying the proposed



method. Compare with the result of the Xu et al.'s [4] in Fig 5.20(b), their approach removes more snow, but it still simultaneously removes other image detail and blurs the image. In Fig 5.20(c), the background textures is be distorted because the most vertical patterns is be regarded as rain streaks in the result by Kang et al. Note that the background texture patterns. In contrast, we see that most snow streaks in all test images are successfully removed, and original textures are faithfully preserved at the same time by the proposed algorithm. Furthermore, clearer and brighter defogged images can be acquired, and the fine transitions can be preserved by the proposed method in the fog like appearance without introducing unpleasing artifacts.

In *Case 3*, the input image is used the proposed method to remove the snow “flake”. In Fig 5.21(b) and Fig 5.21(c), the refined guidance images have similar contour with the un-degraded image and also maintain the detailed information which may be lost by using the guided filter [55]. Although most snow can be removed by these methods, other image detail will be removed and image will be blurred in the meantime. We see that most snowflakes in all test images are successfully removed, and original textures are faithfully preserved at the same time by the proposed algorithm. Fig 5.22 shows other snowflakes removal results.

In *Case 4*, the frequency-based analysis method [7] focuses on the removal of rain and snow streaks in video sequences captured by static or dynamic cameras. Compare with the results of Barnum et al. [7] shown in Fig 5.23-26, we just consider frame by frame in our proposed method. The evaluation method as [69] is used in their approach, and it is used to track points while each sequence is played forward then backwards. Because each sequence starts and ends on the same frame, each point should be in the same location at the beginning and the end. Tracking accuracy is defined as the distance between each point at the beginning and end of the loop. There are some redundant



textures around the rain removal regions, but there are not producing displeasing artifacts as shown in Fig 5.23 in our method. In Fig 5.24, when raindrops are broken with splashes falling on the subjects, the orientation of rain-streak rotation angle may be horizontal. In this case, the rain streaks cannot be removed well by the frequency-based [7], but our proposed method can be used to deal with this problem. In Fig 5.25, we see that most rain streaks in the video sequence are successfully removed, and original textures are faithfully preserved at the same time by the proposed method. This is a very difficult sequence with a lot of high frequency textures, very heavy snow, and multiple moving objects as shown in Fig 5.26. In Fig 5.26(b), much of the snow is removed, but the edge of the umbrella is misclassified. In contrast, we see that most snow streaks in this video sequence are successfully removed, and original textures are faithfully preserved at the same time by the proposed method as shown in Fig 5.26(c).

In *Case 5*, we focus that rain presents on the window surface. In Fig 5.27(b), the scene and reflections are preserved; raindrops on the window are removed but a few small artifacts do remain by Eigen et al. [61] approach. There are no artifacts and most of water drops are removed while retaining image detail as shown in Fig 5.27(c) in our method. Fig 5.28 shows another focused rain removal results. We see that most raindrops in single image are successfully removed, and original textures are faithfully preserved at the same time by the proposed method as shown in Fig 5.28(f). Compare with the result of the Cord et al.'s [63] in Fig 5.29(h), their approach has much false and missed detection. Fig 5.30 shows another unfocused rain removal results. More experimental results can be found [70]:

https://sites.google.com/site/yutaisaithesis/rain_removal

https://sites.google.com/site/yutaisaithesis/snow_removal

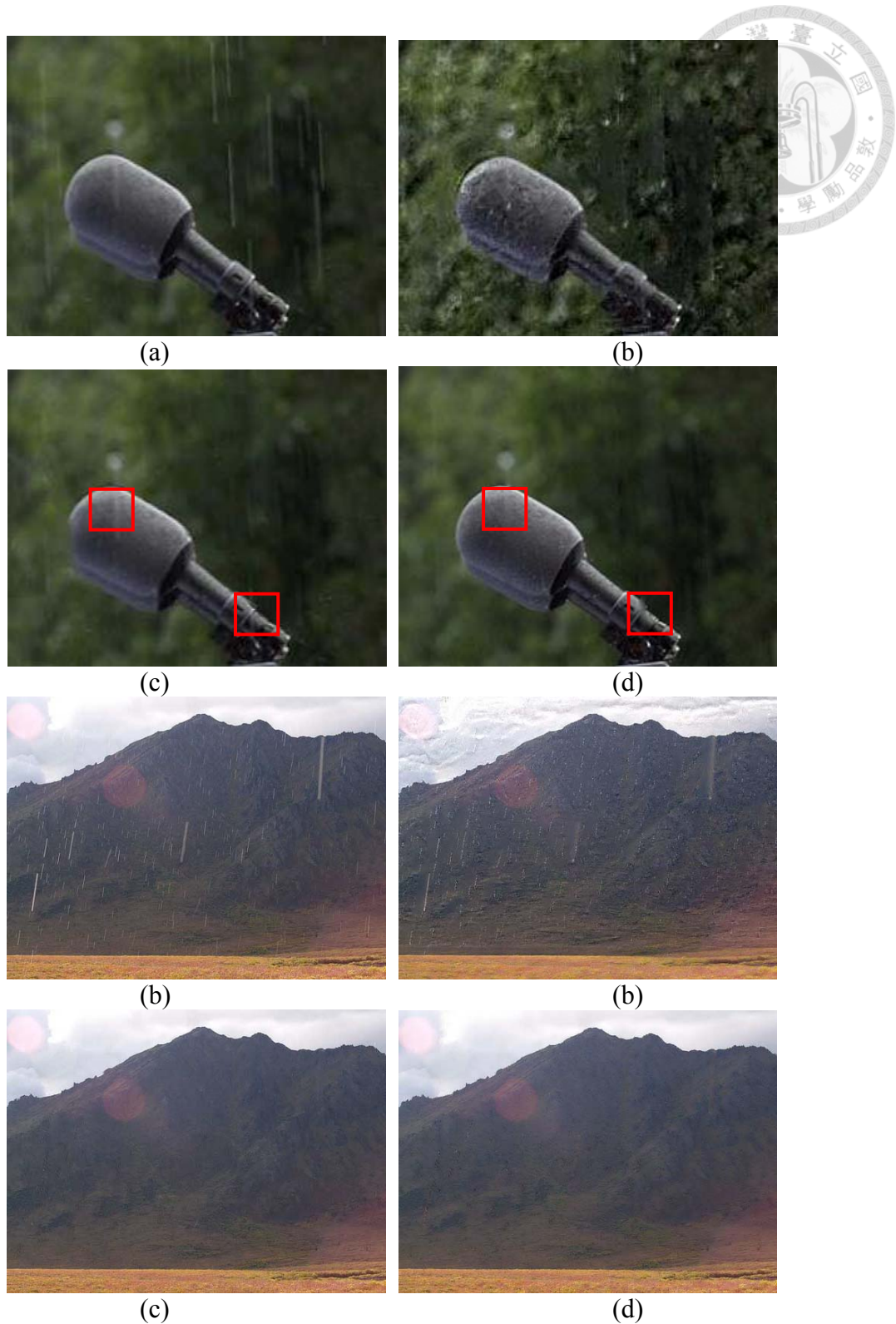


Fig. 5.18 Comparison of rain removal results: (a) the original rain image; the rain-removed version via: (b) Kang et al.'s method with the single-frame-based image decomposition [5], (c) Kim et al.'s method with the adaptive nonlocal mean filter [6]; and (d) the proposed rain removal scheme.



(a)



(b)



(c)



(d)



(a)



(b)



(c)



(d)



(a)



(b)



(c)



(d)



(a)



(b)



(c)



(d)



(a)



(b)



(c)



(d)

Fig. 5.19 Comparison of rain removal results: (a) the original rain image; the rain-removed version via: (b) Xu et al.'s method with the guided filter [4]; (c) Kang et al.'s method with the single-frame-based image decomposition [5]; and (d) the proposed rain removal scheme.



(a)



(b)



(c)



(d)



(a)



(b)



(c)



(d)



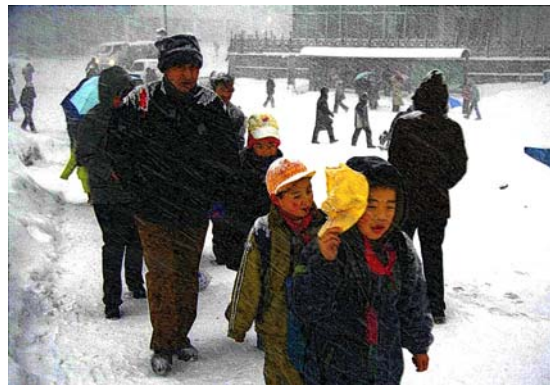
(a)



(b)



(c)



(d)

Fig. 5.20 Comparison of snow “streak” removal results: (a) the original snow image; the snow-removed version via: (b) Xu et al.’s method with the guided filter [4]; (c) Kang et al.’s method with the single-frame-based image decomposition [5]; and (d) the proposed snow removal scheme.



Fig. 5.21 Comparison of snow “streak” removal results: (a) the original snow image; the snow-removed version via: (b) Xu et al.’s method with the guided filter [4]; (c) Xu et al.’s method with the refined guidance image [4]; and (d) the proposed snow removal scheme.

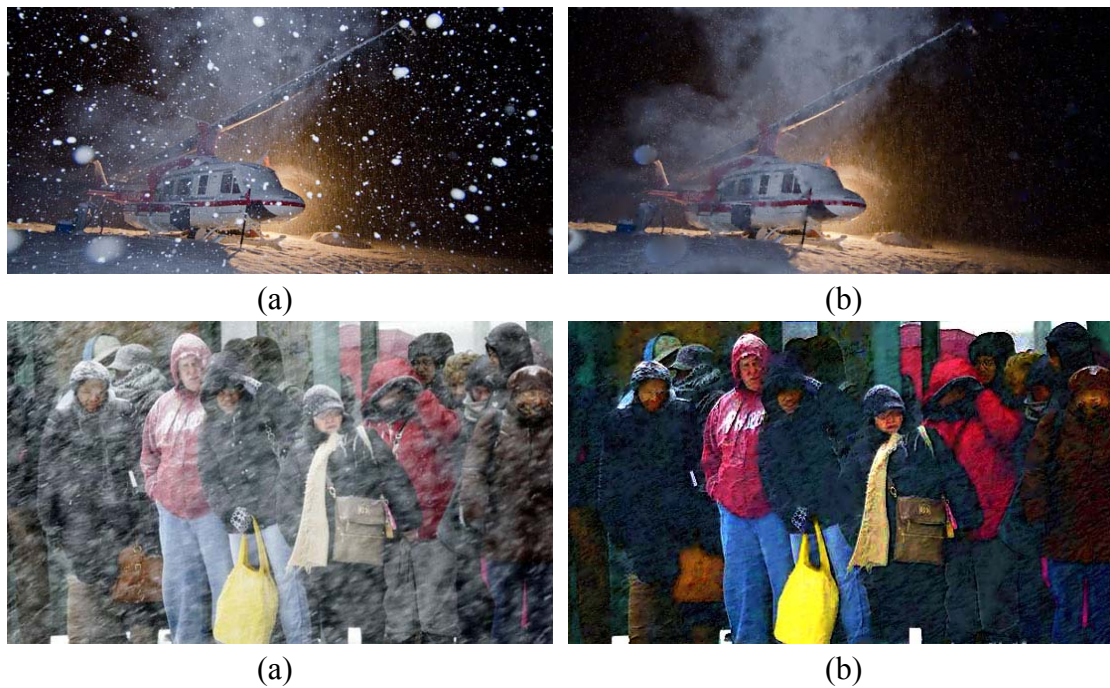


Fig. 5.22 Snowflakes removal results: (a) Input snow images. (b) Our results.



Fig. 5.23 Comparison of rain streaks removal results: (a) the sitting man sequence. (b) rain removal by the frequency-based analysis [7]. (c) the proposed rain removal scheme.

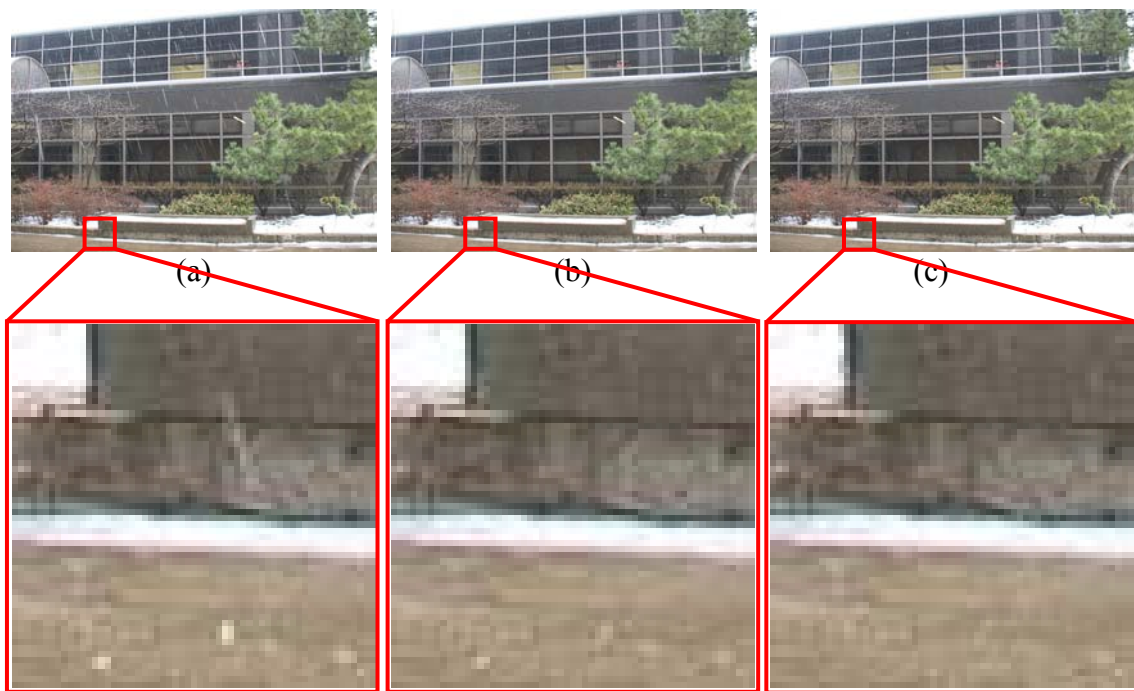


Fig. 5.24 Comparison of rain streaks removal results: (a) the window building sequence. (b) rain removal by the frequency-based analysis [7]. (c) the proposed rain removal scheme.

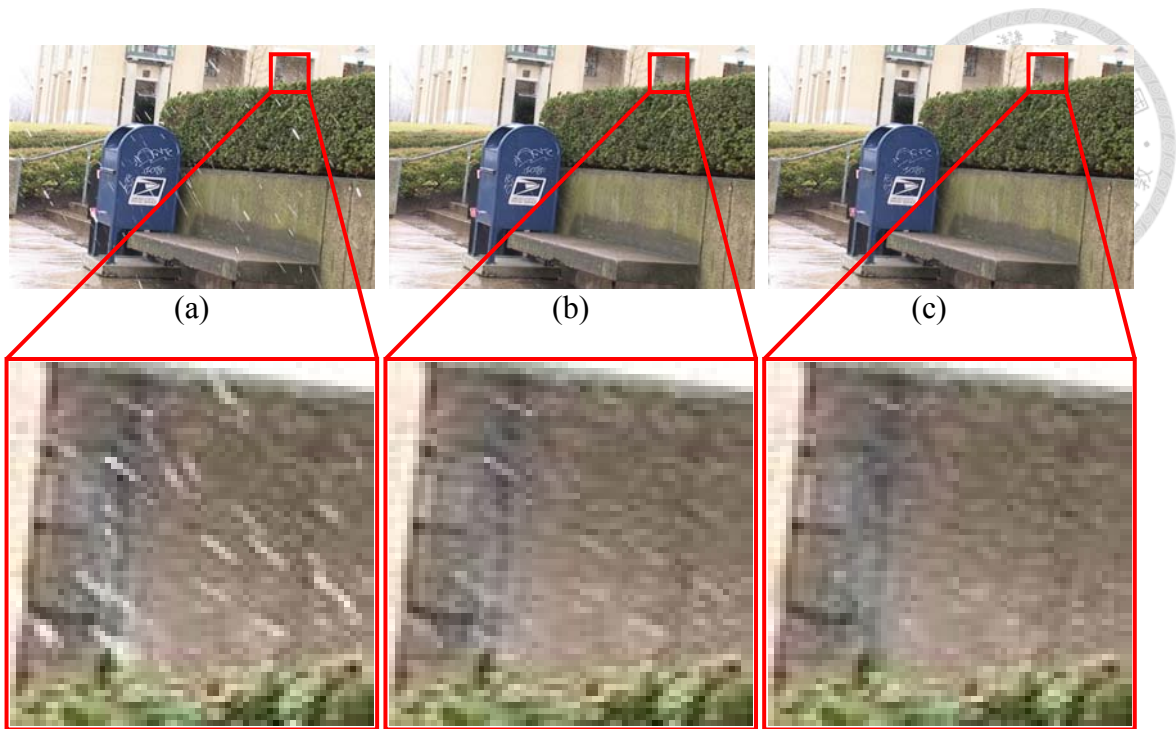


Fig. 5.25 Comparison of snow removal results: (a) the mailbox sequence. (b) snow removal by the frequency-based analysis [7]. (c) the proposed snow removal scheme.

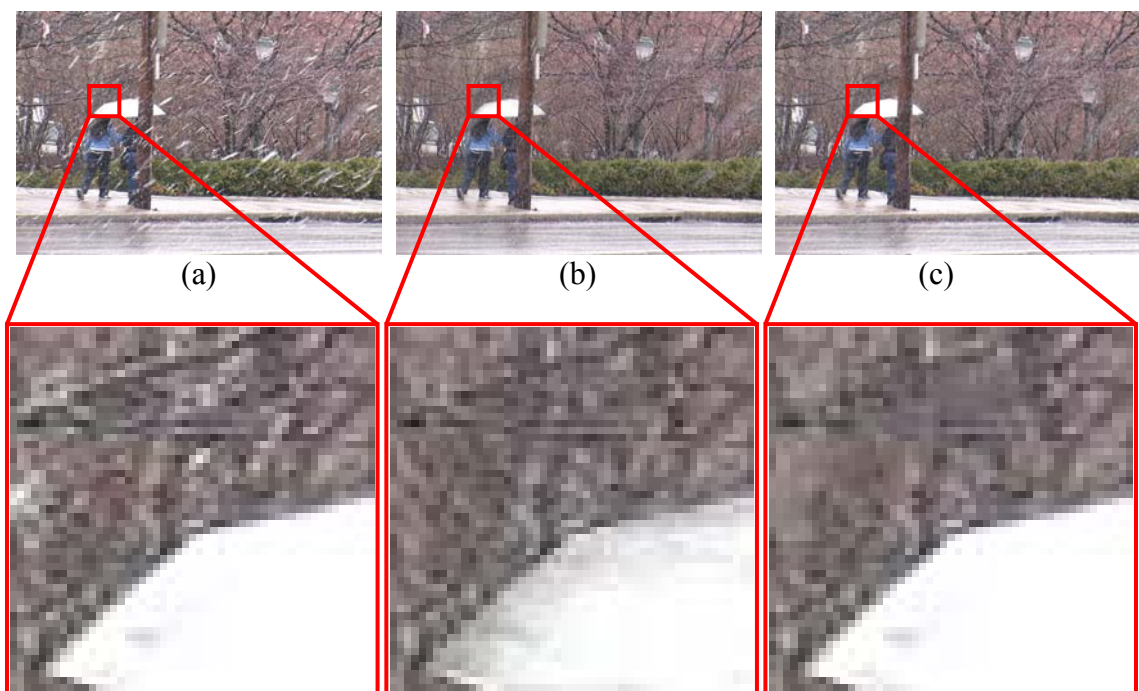


Fig. 5.26 Comparison of snow removal results: (a) the walker in the snow sequence. (b) snow removal by the frequency-based analysis [7]. (c) the proposed snow removal scheme.

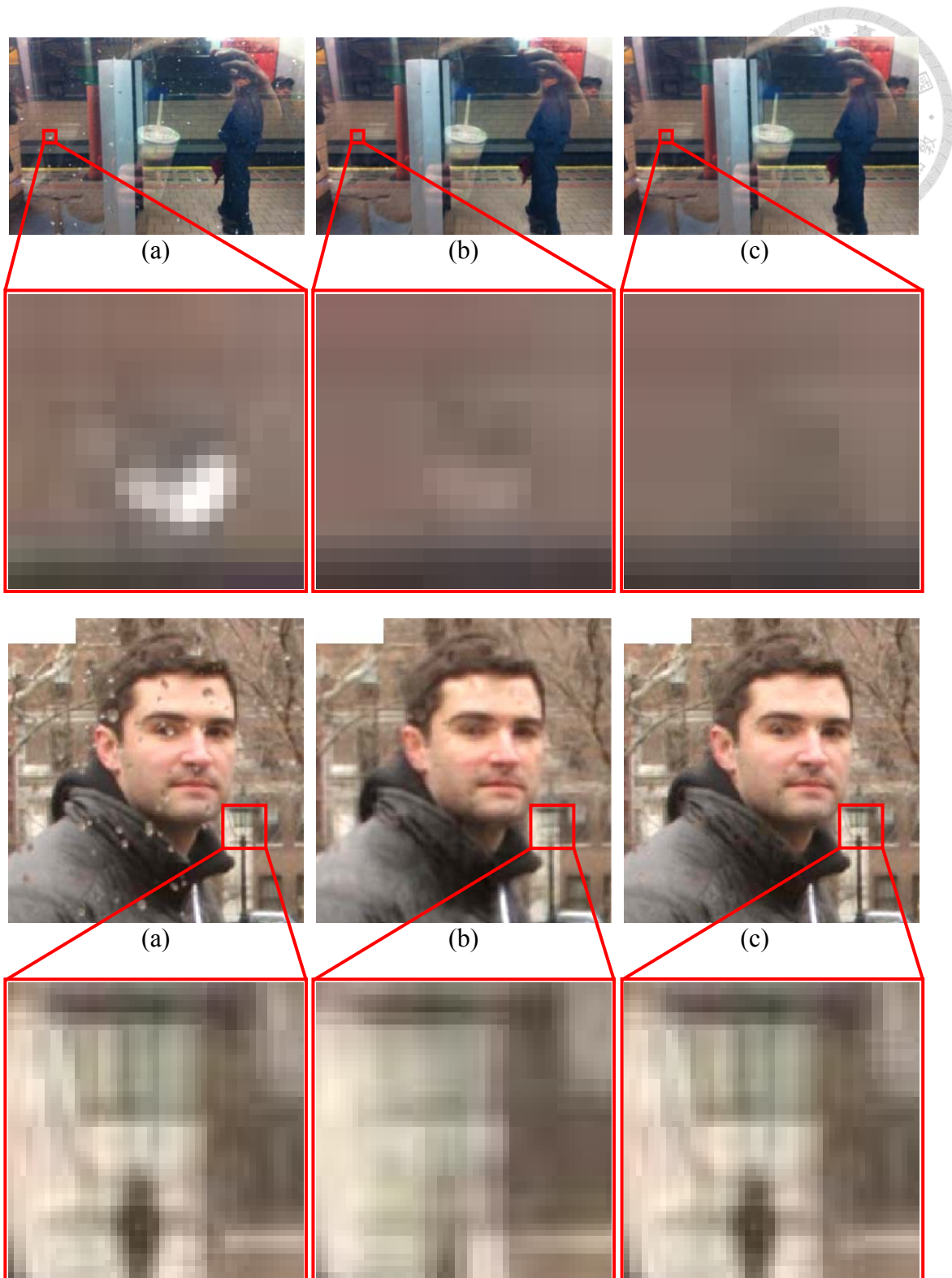


Fig. 5.27 Comparison of rain drops removal results: (a) smartphone shot through a rainy window on a train. (b) rain removal by [61]. (c) the proposed rain removal scheme.

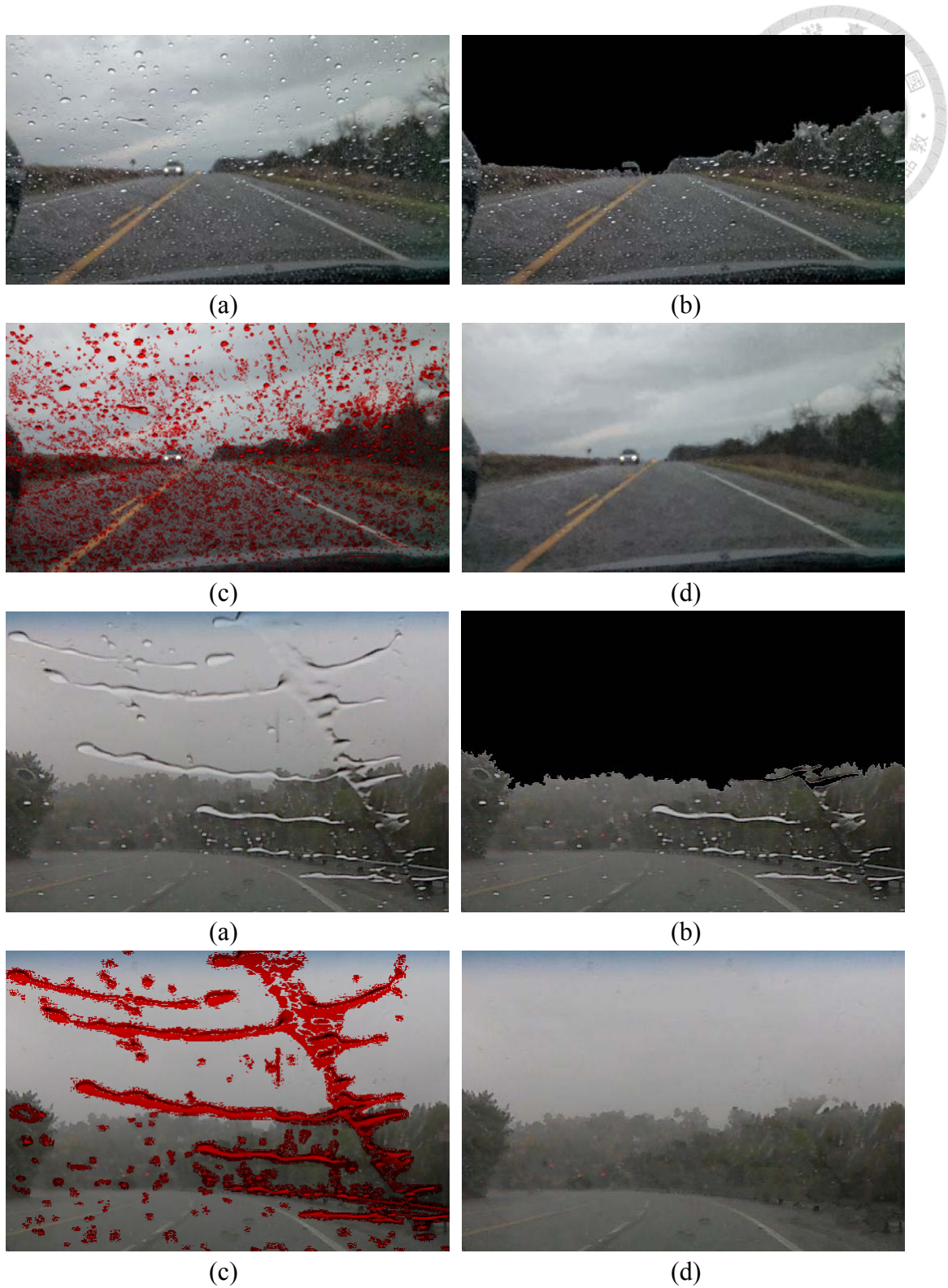


Fig. 5.28 Comparison of focused raindrops detection results: (a) original image acquired by camera. (b) the dark region. (c) raindrops detected by our proposed scheme. (d) the result after the proposed rain removal scheme.

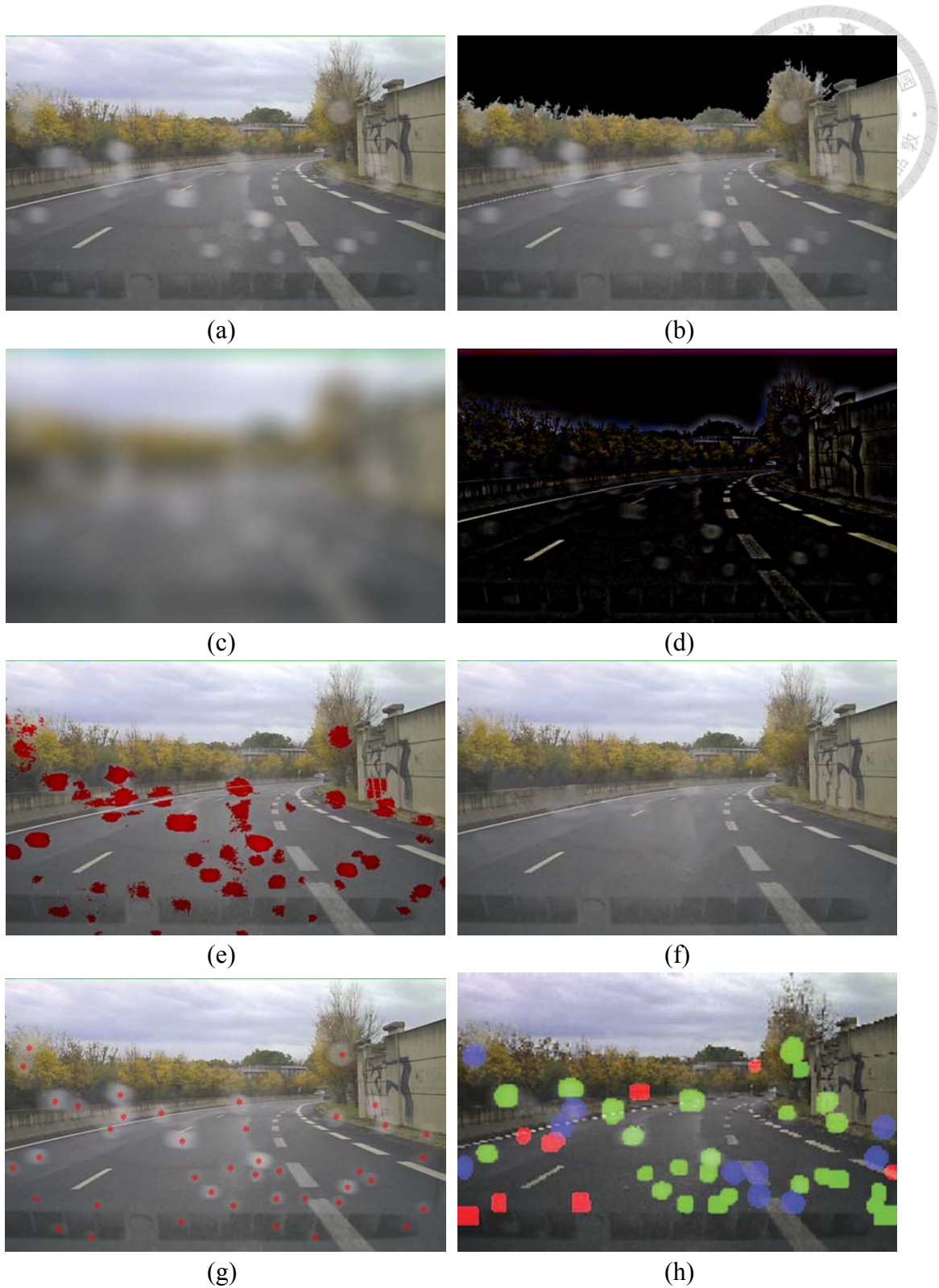


Fig. 5.29 Comparison of unfocused raindrops detection results: (a) original image acquired by camera. (b) the dark region (raindrops are visible in this region). (c) the background image. (d) the difference between the original image and background image.

(e) raindrops detected by our proposed scheme. (f) the result after the proposed rain removal scheme. (g) ground truth: red stars correspond to the mark made by operator. (h) raindrops detected using the background subtraction method [63]. Green: correctly detected raindrops. Blue: missed raindrops. Red: false detection.

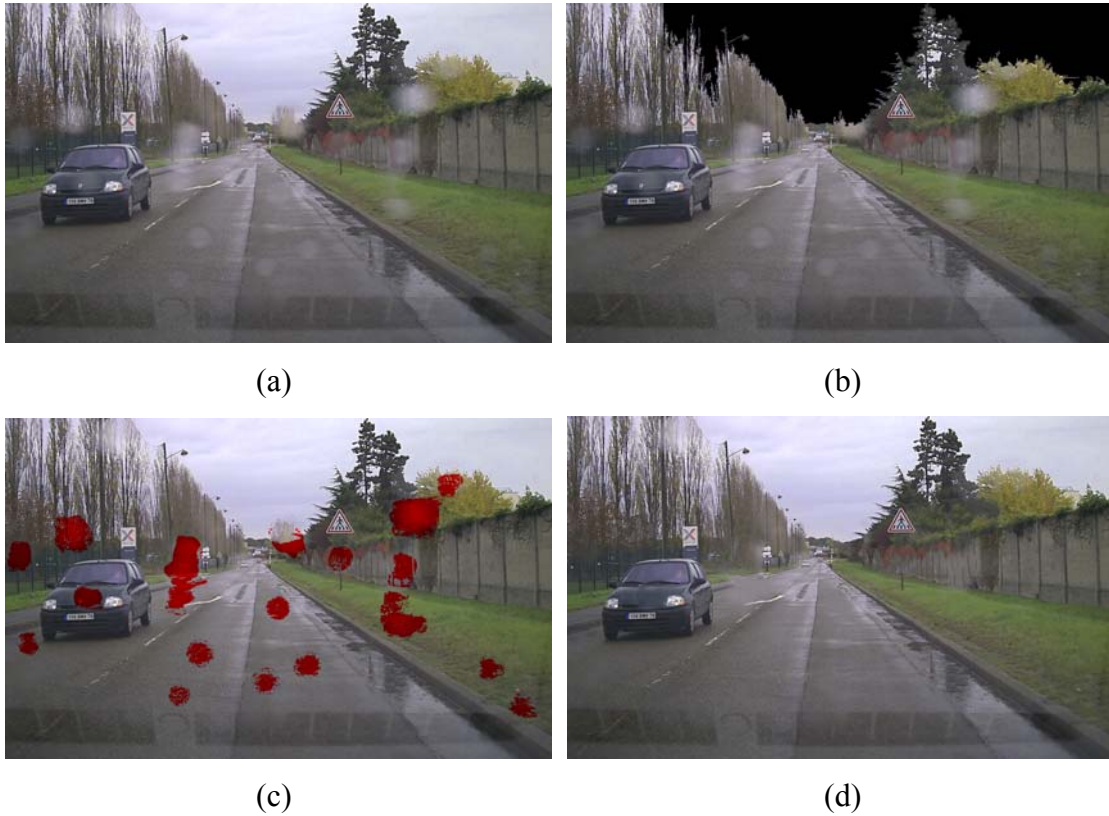
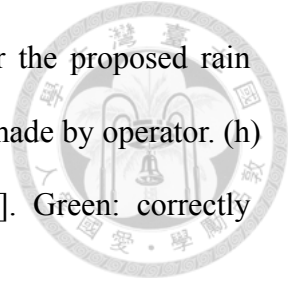
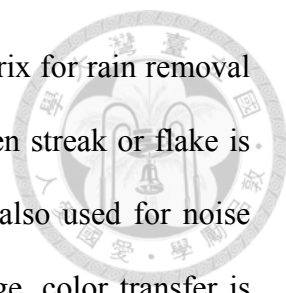


Fig. 5.30 Comparison of unfocused raindrops detection results: (a) original image acquired by camera. (b) the dark region (raindrops are visible in this region). (c) raindrops detected by our proposed scheme. (d) the result after the proposed rain removal scheme.

5.4 Conclusions

According to the natural property of rain and snow, we divide the rain or snow removal scheme into two parts: the first part is detection of rain or snow and the second part is inpainting. How to select a proper threshold is important. Furthermore, we make



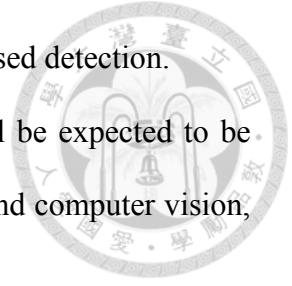
the column extended into both side columns to produce a block-matrix for rain removal so that it may get more benefits for single image consideration when streak or flake is not obvious. The fuzzy random impulse reduction method [61] is also used for noise removal. Specifically, to obtain a quality vision of a resulting image, color transfer is utilized to protect the final snow-free image's color from high dynamic. The results show that our method is attractive and effective for the rain and snow removing quality. As follows, rain and snow removal methods with low complexity, low computational time, and high rain removing quality are proposed.

Our proposed method is computationally effective taking approximately 2 seconds (Matlab code) for a 400×400 image. Kang et al.'s [5] method taking approximately 66 seconds and Xu et al.'s [4] method taking approximately 0.3 seconds. Although Xu et al.'s [7] method use the shortest time, this method simultaneously removes other image detail and blurs the image. The performance of Kang et al.'s [5] method depends on the clustering of dictionary basis vectors. When the clustering is not effective, their method may erase textures, as well as rain streaks, and yield visual artifacts in a restored image. Furthermore, the procession of dictionary learning needs much more processing time.

Our proposed method can also deal with the case that rain presents on the window surface. Although Eigen et al.'s [61] method can effective remove dirt and rain in outdoor test conditions; this method simultaneously removes other image detail and blurs the image. Furthermore, the quality of the results does depend on the statistics of test cases being similar to those of the training set. In the cases, where this does not hold, and we see significant artifacts in their output. The corruption cannot be much larger than the training patches. It means that their input image may need to be down-sampled, e.g. as in the rain application, leading to a loss of resolution relative to the original. The performance of Cord et al.'s [63] method depends on the watershed segmentation and

background subtraction. Their method may have much false and missed detection.

In the future work, the rain and snow removal techniques will be expected to be used for many applications, such as traffic safety, film processing, and computer vision, etc..



Chapter 6 Related Work of Underwater Image Enhancement



Underwater image enhancement is a challenging problem because of the physical properties existing in such environment. Different from common images, underwater images are suffered from degradation because of poor visibility conditions and effects such as the attenuation of the propagated light, light absorption, light reflection, bending of light and scattering of light. The main reasons why light is attenuated exponentially with the distance and depth are absorption and scattering effects. The absorption substantially reduces the light energy while the scattering causes changes in the light direction. Thus, underwater enhanced technique becomes an essential and necessary in many application fields especially in computer vision.

6.1 Introduction

In seawater, the objects at a distance of more than 10 meters are hard to be distinguished because the colors are faded since their characteristic wavelengths are cut as the depth increases. Fig. 6.1 shows the absorption of light by water. For every 10m increase in depth, the brightness of sunlight will drop by half. Almost all red light is gone by 50% from the surface, but blue light travels the longest in the water due to its shortest wavelength. That is why most underwater images are dominated by blue-green coloration.

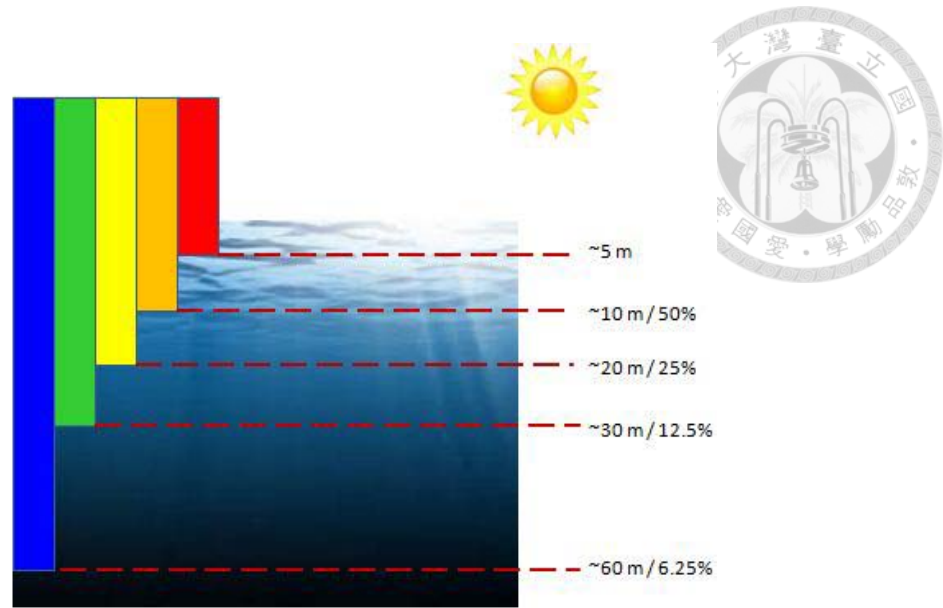


Fig. 6.1 Absorption of light by water.

Therefore, many methods have been proposed. The first method is based on (e.g. [15], [16]) polarization filters. The main idea of this approach is to exploit two or more images including different DOP in the same scene, which are obtained by rotating a polarizing filter attached to the camera. However, the common drawback of the methods in this approach is that they cannot be applied in dynamic scenes because the changes are more rapid than the filter rotation in finding the maximum and minimum DOP. This method is relatively feasible for outdoor hazy and foggy images, but the setup of the camera might be in trouble for the underwater case. Fig. 6.2 shows some results by applying the polarization based method, including the white balanced raw frame (a) and the final restored raw frame (b).

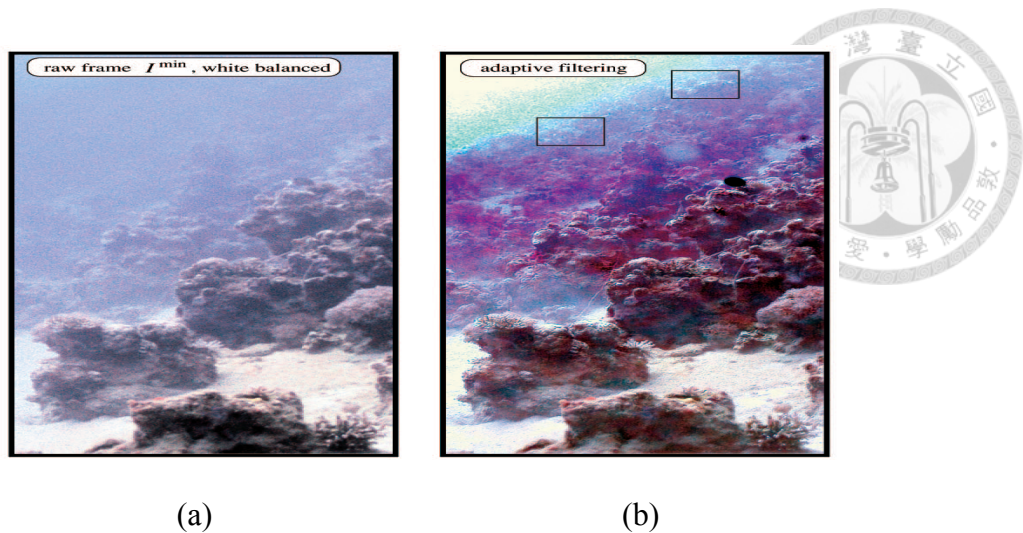


Fig. 6.2 Results of the polarization based method. (a) the white balanced raw frame. (b) the final restored raw frame.

The second method by using multiple images is taken from bad weather scenes (e.g. [17], [18], [19], [20]). The basic idea of this method is to manipulate on the differences of two or more images in the same scene including different properties of the participating medium. Although visibility can be significantly enhanced by the method in this approach, the results are unable to be delivered immediately by their requirements because the results have to be shown after the properties of the medium change.

The third is depth based method, which demands the rough depth information form approximated 3D geometrical model of the input scene (e.g. [21], [22], [23]). The third method is based on depth, and the rough depth information formed approximated 3D geometrical model of the input scene is be demanded by the method. The fourth method is based on specialized hardware [71] which is relatively expensive and complex. In order to overcome the drawbacks, the single image algorithms have been investigated in [8], [9], and [10]. In the following sections, we will specifically introduce these three typical underwater enhancement methods, respectively.

6.2 Histogram-Based Equalization Based



6.2.1 Basic Concept of Histogram-Based Equalization

Histogram equalization (HE) is one of the well-known methods for enhancing the contrast of given images, making the result image have a uniform distribution of the gray levels. It flattens and stretches the dynamic range of the images histogram and results in overall contrast improvement. HE has been widely applied when the image needs intensification however, it may significantly change the brightness of an input image and cause problem in some applications where brightness preservation is necessary. So other histogram techniques may need to be used, such as adaptive histogram equalization and contrasted limited adaptive histogram equalization.

The Contrast Limited Adaptive Histogram Equalization had been proposed in [72]. The main idea is to separate the image into a number of tiles, and then adjust the contrast such that the tile histogram has the desired shape. The tiles are then stitched together using bilinear interpolation. Overview of it, this is an image contrast enhancement algorithm that overcomes limitations in standard histogram equalization. If plotting the cumulative distribution function (CDF) of an image histogram, it can be noticed that the CDF does not form a straight line means the pixel values are not equally likely to occur as illustrated in Fig6.3. Thus the process of flattening the CDF is called histogram equalization.

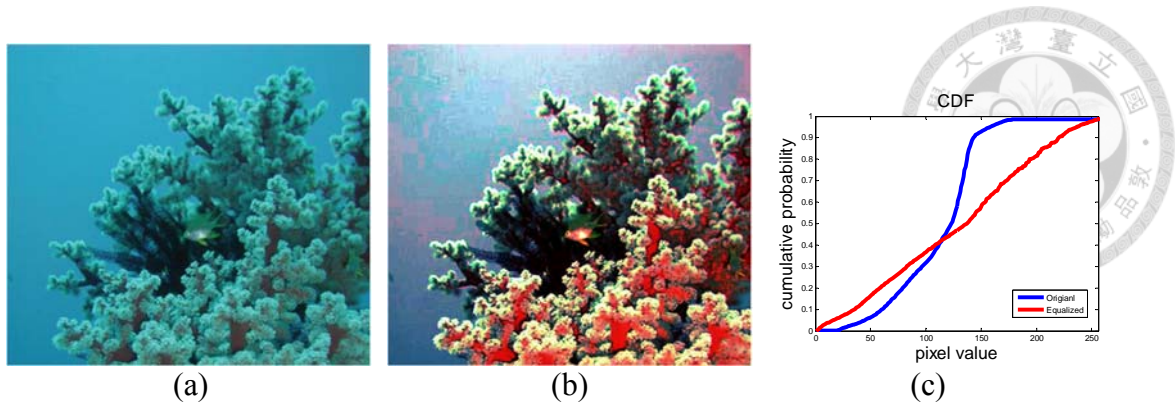


Fig. 6.3 Result of histogram equalization for an underwater image. (a) Original underwater image, (b) HE image, and (c) CDF of original underwater image and HE image in gray level.

The two primary features is adaptive HE (AHE), which divides the images into regions into smaller tiles, applies histogram equalization to each tile, then interpolates the results, and the contrast limited AHE (CLAHE), which reduces noise by partially reducing the local HE. Bilinear interpolation is used to avoid visibility of region boundaries. They differ from standard histogram equalization in the respect that both methods operates on small tiles in the image and computes several histograms, each corresponding to a distinct section of the image and use them to redistribute the lightness values of the image.

The expression of modified gray level for standard CLAHE method with uniform distribution can be written as

$$g = [g_{\max} - g_{\min}] \times P(f) + g_{\min} \quad (6.1)$$

where g is the pixel value, g_{\max} is the maximum pixel value, g_{\min} is the minimum pixel value, and $P(f)$ is its CDF. In addition to, for exponential distribution in gray level, it can be adapted as

$$g = g_{\min} - \left(\frac{1}{\alpha} \right) \times \ln[1 - P(f)] \quad (6.2)$$

where α is the clip parameter. This underwater image highlights two peculiarities of CLAHE [73], as shown in Fig. 6.4. First, sharp edges, like those around the corals. This occurs because CLAHE computes histograms over areas, and the sharp change in values from the background to the corals affects the normalization. (The effect is related to what you would get by dividing the original image by the low-pass filtered version of the image.) Fortunately, that additional contrast near the edges can help some edge detection algorithms, even if the glow is not natural. The second effect from CLAHE is seen in the background areas, where some out-of-focus corals become visible and the overall noise increases. This is exactly what CLAHE is supposed to do: increase the contrast, even in the background areas. It is also limiting the amount of contrast adjustment.

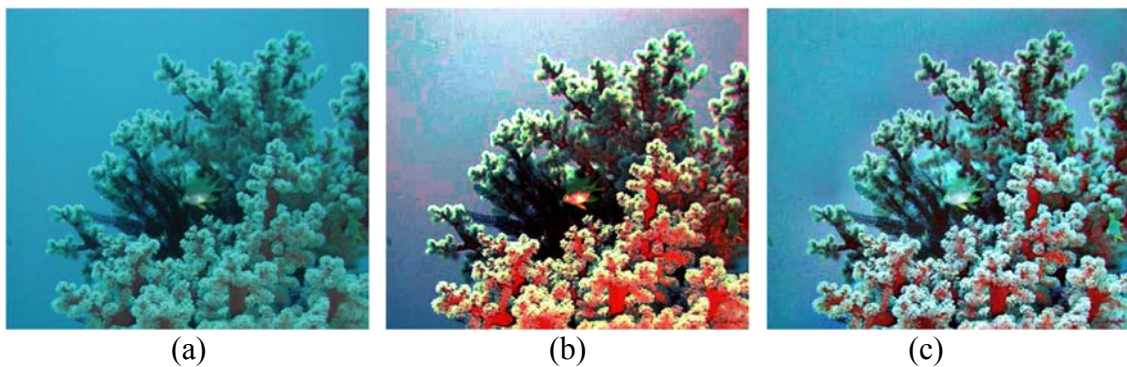


Fig. 6.4 Comparison with the equalization method for an underwater image. (a) Original underwater image, (b) HE image, and (c) CLAHE on *RGB* color model image.

6.2.2 Advantage and Disadvantage

Adaptive histogram equalization and contrasted limited adaptive histogram equalization improve local contrast of an image more than standard histogram equalization does by bringing out more details but still has tendency to amplify noise.



6.3 Wavelength-Based Compensation

The wavelength compensation and image dehazing method had been proposed by Chiang et al. [9] in 2011. They can process light scattering and color shift distortion suffered by underwater images simultaneously.

6.3.1 Basic Concept of Wavelength Compensation

The method in [9] is based on the hazy image formation model (e.g. [1], [2], [11], [12] and [13]), which is similar like model (1.1)

$$I_{\lambda}(x) = J_{\lambda}(x) \cdot t_{\lambda}(x) + (1 - t_{\lambda}(x)) \cdot B_{\lambda}, \quad \lambda \in \{red, green, blue\} \quad (6.3)$$

where $I_{\lambda}(x)$ is the observed intensity of the image, x is the pixel's index, $J_{\lambda}(x)$ is the scene radiance of the image which is desired to be obtained by underwater enhancing techniques, $t_{\lambda}(x)$ is the residual energy ratio of $J_{\lambda}(x)$ after reflecting from pixel x in the underwater scene and reaching the observer, and B_{λ} is the homogeneous background light. The first term is the direct attenuation of scene in water, and the second term is the homogeneous background light. The residual energy ratio $t_{\lambda}(x)$ can be represented as

$$t_{\lambda}(x) = \frac{E_{\lambda}^{residual}(x)}{E_{\lambda}^{initial}(x)} = \text{Nrer}(\lambda)^{d(x)} \quad (6.4)$$

which means the residual energy of light beam with wavelength λ traveling distance $d(x)$. The normalized residual ratio $\text{Nrer}(\lambda)$ depends on the light wavelength transmitted [74], as illustrated in Fig 6.5. The flow chart of this algorithm [9] is briefly expressed in Fig. 6.6.

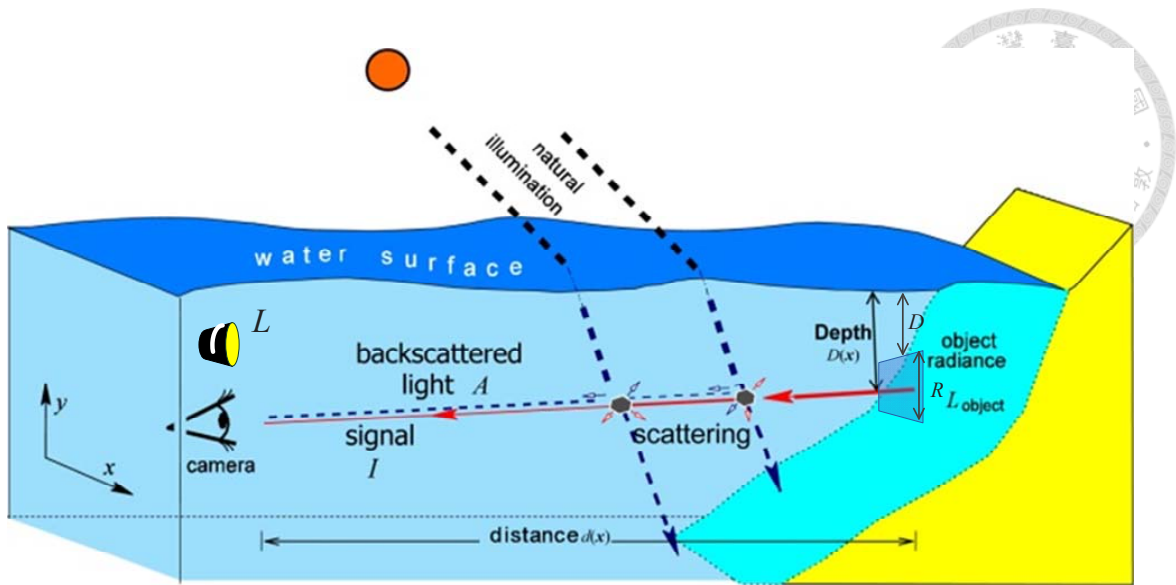


Fig. 6.5 Underwater optical imaging model (Y. Schechner et al.).

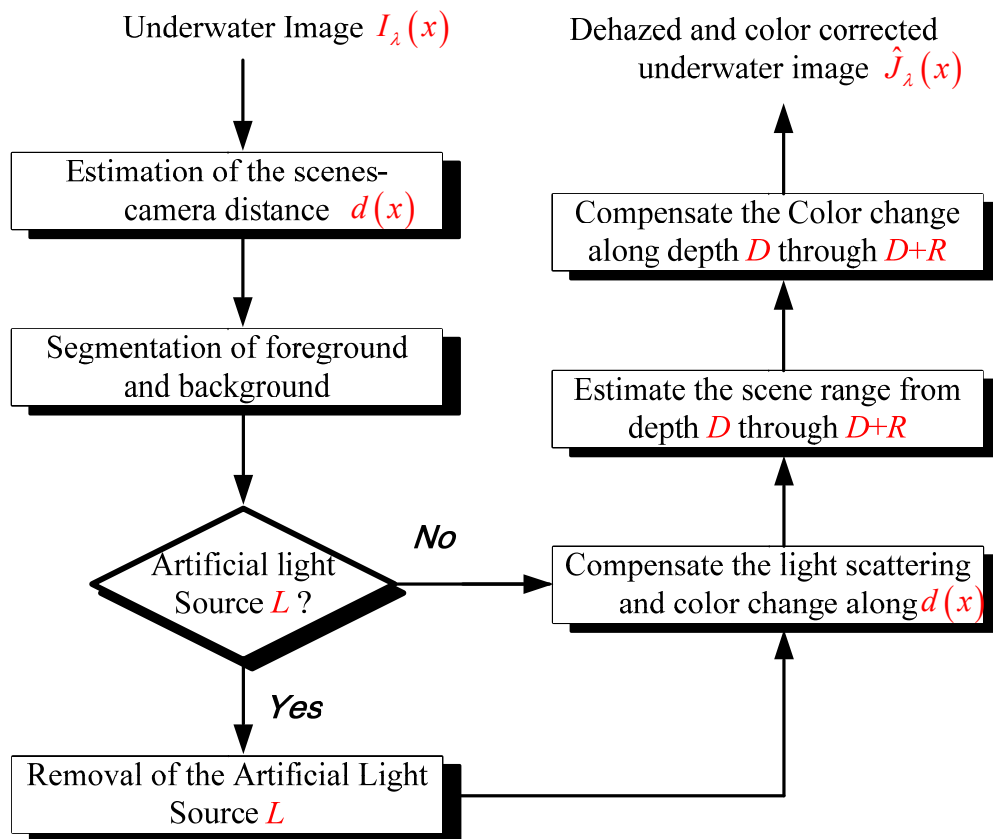


Fig. 6.6 Flow chart of the paper proposed by Chiang et al. [9].

Firstly they consider the influence of the artificial light L. When airlight A incident from air to the water reaches the underwater scene point x with depth $D(x)$, the energy of residual light can be expressed as

$$E_{\lambda}^W(x) = E_{\lambda}^A(x) \cdot \text{Nrer}(\lambda)^{D(x)}, \quad \lambda \in \{red, green, blue\} \quad (6.5)$$

Light emanated from point x is equal to the amount of illuminating ambient light reflected, hence the image formation model (6.1) can be represented as

$$I_{\lambda}(x) = \left(E_{\lambda}^A(x) \cdot \text{Nrer}(\lambda)^{D(x)} \cdot \rho_{\lambda}(x) \right) \cdot t_{\lambda}(x) + (1 - t_{\lambda}(x)) \cdot B_{\lambda}, \quad (6.6)$$

$$\lambda \in \{red, green, blue\}$$

or

$$I_{\lambda}(x) = \left(E_{\lambda}^A(x) \cdot \text{Nrer}(\lambda)^{D(x)} \cdot \rho_{\lambda}(x) \right) \cdot \text{Nrer}(\lambda)^{d(x)} + \left(1 - \text{Nrer}(\lambda)^{d(x)} \right) \cdot B_{\lambda}, \quad (6.7)$$

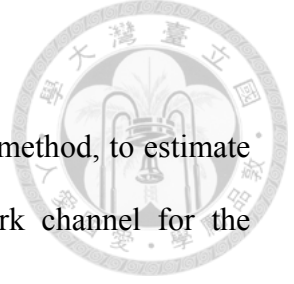
$$\lambda \in \{red, green, blue\}$$

where $\rho_{\lambda}(x)$ is the reflectivity of point x for light with wavelength λ .

Due to the inadequate lighting in an underwater photographic environment we should use the artificial light L to overcome this problem. If we want to get the scene radiance of the image which is desired, the artificial light should be removed before the WCID operation. According to the concept of (6.5), we know the residual energy of the artificial light after the course propagation is $E_{\lambda}^L(x) \cdot \text{Nrer}(\lambda)^{d(x)}$. During the forward and backward course of propagation pertinent to $d(x)$, color change occurs. The image formation model (6.4) or (6.5) can further modified as

$$I_{\lambda}(x) = \left(\left(E_{\lambda}^A(x) \cdot \text{Nrer}(\lambda)^{D(x)} + E_{\lambda}^L(x) \cdot \text{Nrer}(\lambda)^{d(x)} \right) \cdot \rho_{\lambda}(x) \right) \cdot \text{Nrer}(\lambda)^{d(x)} + \left(1 - \text{Nrer}(\lambda)^{d(x)} \right) \cdot B_{\lambda}, \quad \lambda \in \{red, green, blue\} \quad (6.8)$$

From (6.6), there are some parameters should be estimated. We explain the procedure in the following:



Step 1: The estimation of the scenes-camera distance $d(x)$

They use the dark channel prior [3], a scenes-depth derivation method, to estimate the distances of the scenes to the camera. They defined the dark channel for the underwater as

$$J^{dark}(x) = \min_{\lambda} (\min_{y \in \Omega(x)} (J_{\lambda}(y))), \quad \lambda \in \{red, green, blue\} \quad (6.9)$$

If point x belong to the foreground subject, the value of the dark channel is closer to zero. take the min operation in the local patch among three color channels on (6.8) to obtain

$$\begin{aligned} \min_{y \in \Omega(x)} (I_{\lambda}(y)) &= \min_{y \in \Omega(x)} \left\{ J_{\lambda}(y) \cdot \text{Nrer}(\lambda)^{d(y)} + (1 - \text{Nrer}(\lambda)^{d(x)}) \cdot B_{\lambda} \right\} \\ , \quad \lambda &\in \{red, green, blue\} \end{aligned} \quad (6.10)$$

Since B_{λ} is the homogeneous background light and the residual energy ratio $\text{Nrer}(\lambda)^{d(y)}$ on the small local patch surrounding point x is essentially a constant $\text{Nrer}(\lambda)^{d(x)}$ [2], the min value on the second term can be removed. They rearrange the above equation (6.10) and do min operation among all three color channel as

$$\begin{aligned} &\min_{\lambda} \left\{ \frac{\min_{y \in \Omega(x)} (I_{\lambda}(x))}{B_{\lambda}} \right\} \\ &= \min_{\lambda} \left\{ \frac{\min_{y \in \Omega(x)} (J_{\lambda}(y))}{B_{\lambda}} \cdot \text{Nrer}(\lambda)^{d(x)} \right\} + \min_{\lambda} (1 - \text{Nrer}(\lambda)^{d(x)}) \\ , \quad \lambda &\in \{red, green, blue\} \end{aligned} \quad (6.11)$$

where the first term in (6.11) satisfy the following inequality

$$0 < \min_{\lambda} \left\{ \frac{\min_{y \in \Omega(x)} (J_{\lambda}(y))}{B_{\lambda}} \cdot \text{Nrer}(\lambda)^{d(x)} \right\} \leq \frac{\min_{y \in \Omega(x)} (J_{\lambda}(y)) \cdot \min_{\lambda} (\text{Nrer}(\lambda)^{d(x)})}{\min_{\lambda} (B_{\lambda})} \quad (6.12)$$

The dark channel J^{dark} for the underwater tends to be zero. According to (6.11), it can

be rewritten as

$$\min_{\lambda} \left\{ \text{Nrer}(\lambda)^{d(x)} \right\} = 1 - \min_{\lambda} \left\{ \frac{\min_{y \in \Omega(x)} (I_{\lambda}(y))}{B_{\lambda}} \right\}, \quad \lambda \in \{red, green, blue\} \quad (6.13)$$

In all of three color channels, $\text{Nrer}(red)$ have the lowest value. In order to increase the estimation of background light, a min operation is performed in every local patch of all pixels in image I . The value of the brightest pixel in the background light can be expressed as

$$B_{\lambda} = \max_{x \in I} \min_{y \in \Omega(x)} (I_{\lambda}(y)) \quad (6.14)$$

Have the values of the $I_{\lambda}(y)$, B_{λ} , and $\text{Nrer}(red)$, the distance between point x on a subject and the camera can be obtained. They also apply image matting to the depth map to remove the mosaic distortion.

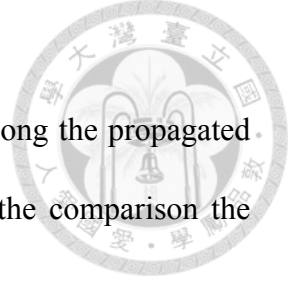
Step 2: Removal of the Artificial Light Source L

They apply the difference between the mean brightness of the foreground and the background to determine whether the artificial light source existence or not.

$$area-type(x) = \begin{cases} foreground & ,if d(x) > \sigma \\ background & ,if d(x) \leq \sigma \end{cases} \quad (6.15)$$

They derive the brightness contribution by artificial light source E_{λ}^L and reflectively $\rho_{\lambda}(x)$, $\lambda \in \{red, green, blue\}$, at point x , the influence caused by the artificial lighting can be removed by subtraction form (6.8) as follows

$$\begin{aligned} \tilde{I}_{\lambda}(x) &= I_{\lambda}(x) - \left(\left(E_{\lambda}^L(x) \cdot \text{Nrer}(\lambda)^{d(x)} \right) \cdot \rho_{\lambda}(x) \right) \cdot \text{Nrer}(\lambda)^{d(x)} \\ &= \left(E_{\lambda}^A(x) \cdot \text{Nrer}(\lambda)^{D(x)} \right) \cdot \rho_{\lambda}(x) \cdot \text{Nrer}(\lambda)^{d(x)} \\ &\quad + \left(1 - \text{Nrer}(\lambda)^{d(x)} \right) \cdot B_{\lambda}, \quad \lambda \in \{red, green, blue\} \end{aligned} \quad (6.16)$$



and then remove the light scattering and color shift that occurred along the propagated distance $d(x)$ from the subjects to the observer. Fig. 6.7 shows the comparison the luminance contributed by an artificial light source.

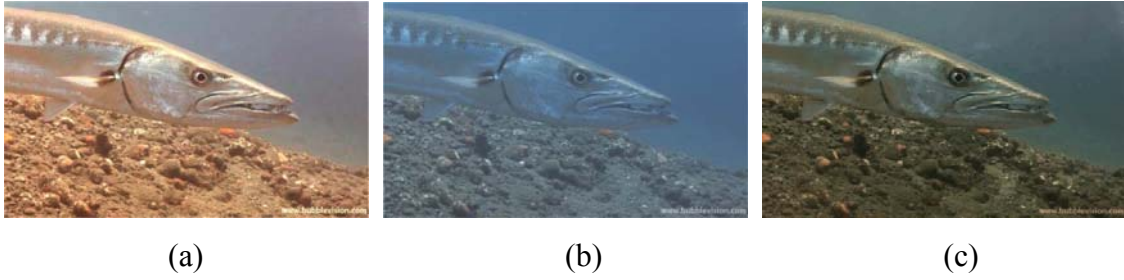


Fig. 6.7 Comparison the luminance contributed by an artificial light source. (a) Illuminated by an artificial light source, the intensity of the foreground appears brighter than that of the background. (b) When the luminance is not be removed first, the overexposed image will be get. (c) Image obtained after processing with WCID [9].

Step 3: Compensate the light scattering and color change along the propagated distance $d(x)$

From (6.3), we know $J_\lambda(x) \cdot t_\lambda(x)$ is the direct attenuation term and $(1-t_\lambda(x)) \cdot B_\lambda$ in the in-scattering term. The haze can be removed by subtracting the in-scattering term. After the dehazing process and color correction introduced through the propagated distance $d(x)$ can be formulated as

$$\begin{aligned}
 J_\lambda(x) &= \frac{I_\lambda(x) - (1 - \text{Nrer}(\lambda)^{d(x)}) \cdot B_\lambda}{\text{Nrer}(\lambda)^{d(x)}} \\
 &= (E_\lambda^A(x) \cdot \text{Nrer}(\lambda)^{d(x)}) \cdot \rho_\lambda(x), \quad \lambda \in \{red, green, blue\}
 \end{aligned}
 \tag{6.17}$$



Step 4: Estimate the scene range from depth D through $D+R$

We should detect the corresponding intensity of the ambient lighting. Hence the underwater depth D is the least square (LS) solution that makes the difference between the attenuation versions of the incident light as follows

$$\min_k \sum_{\lambda} \left\| E_{\lambda}^o - E_{\lambda}^A \cdot (\text{Nrer}(\lambda))^k \right\|^2, \quad \lambda \in \{red, green, blue\} \quad (6.18)$$

Once obtaining the depth D , we can get the restored energy of the image after have removal and color correction.

$$\hat{J}_{\lambda}(x) = \frac{J_{\lambda}(x)}{\text{Nrer}(\lambda)^D}, \quad \lambda \in \{red, green, blue\} \quad (6.19)$$

They assume the pixel x and top and down background pixels are located in scanline a_x , b , and c , respectively. Therefore, the underwater depth $D(x)$ can be express as

$$D(x) = D + R \cdot \frac{a_x - b}{c - b} \quad (6.20)$$

So the restored underwater image can be further modified as

$$\hat{J}_{\lambda}(x) = \frac{J_{\lambda}(x)}{\text{Nrer}(\lambda)^{D(x)}} = E_{\lambda}^A(x) \cdot \rho_{\lambda}(x), \quad \lambda \in \{red, green, blue\} \quad (6.21)$$

6.3.2 Advantage and Disadvantage

The WCID algorithm can effectively restore image color and remove haze. However, the salt ratio and amount of suspended particles in ocean water varies with time, location, and season, making accurate estimation of the rate of energy attenuation problematic. In addition, it is presumed that artificial light sources produce spherically radiating light different to surface light sources generally used in underwater photography; therefore the value of luminance is also difficult to estimate accurately.



6.4 Fusion-Based

C. Ancuto. et al. [10] proposed a fusion-based approach in 2011. They build-up on the fusion strategy that takes a sequence of inputs derived from the initial image.

6.4.1 Basic Concept of Fusion-based

The main idea in this approach is that C. Ancuto. et al. [10] employ several inputs and weight maps that discriminate the regions characterized by poor visibility to overcome the deficiencies existing in the degraded input images. The flow chart of this algorithm [10] is briefly expressed in Fig. 6.8. Firstly, the derived input is represented by the color corrected version of the image. The first one is defined as the white balanced version of the input image. The second input is obtained by applying the classical global min-max windowing method to enhance the image appearance in the selected intensity window. The weights that they used are defined as below:

Weight 1: Laplacian contrast weight W_L

It controls the luminance gain in the final result since the general appearance of the degraded input photo tends to become flat. However, this weight is not sufficient to recover the contrast, mainly because it can not distinguish between a ramp and flat regions. To handle this problem, they searched for an additional contrast measurement that independently assesses the local distribution.

Weight 2: Local contrast weight W_{LC}

It yields high values to image elements such as edges and texture. The local contrast weight is calculated as the standard deviation between the intensity value of the pixel and the local average value of its surrounding region

$$W_{LC}(x, y) = \|I_c - I_c^{ohc}\| \quad (6.22)$$

where I_c is the intensity channel of the input image and I_c^{ohc} is the low pass version



of it.

Weight 3: Saliency contrast weight W_S

It is a quality map that estimates the degree of conspicuousness with respect to the neighborhood regions. This value is effectively computed based on the formulation introduced by Achanta et al. [Achanta et al. 2009].

Weight 4: Exposedness contrast weight W_E

It evaluates how well a pixel is exposed. The exposedness contrast weight W_E is formulated as a Gaussian-modeled distance to the average normalized range value:

$$W_E(x, y) = \exp\left(-\frac{(I^k(x, y) - 0.5)^2}{2\sigma^2}\right) \quad (6.23)$$

where $I^k(x, y)$ is the value of the pixel location (x, y) of the input image, and set the standard deviation as 0.25. This weight can yield a well preserved appearance of the fused image.

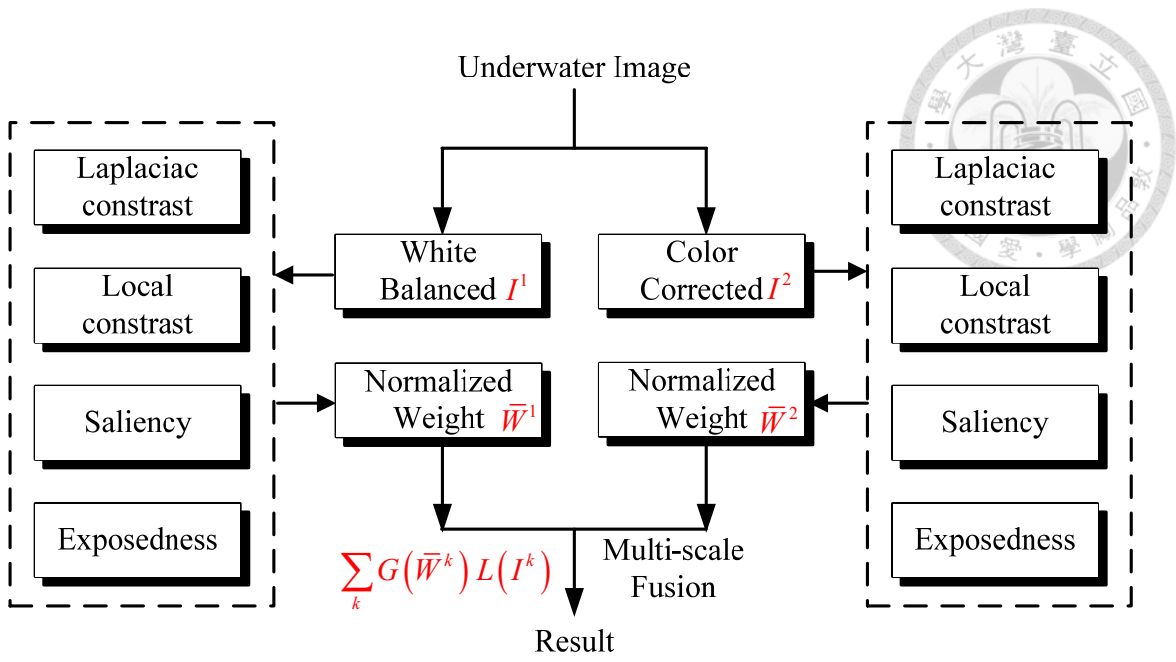
After the weights are obtained as shown in Fig. 6.9, they normalized the values of weight maps by constraining that each pixel of the weight map to equal one. Finally, the inputs and the weights are merged by a multi-scale fusion process as

$$R(x, y) = \sum_{k=1}^K \bar{W}^k(x, y) I^k(x, y) \quad (6.24)$$

where $I^k(x, y)$ symbolized the input that is weighted by the normalized weight maps \bar{W}^k . The final restored image is obtained by mixing between the Laplacian inputs and Gaussian normalized weights at each scale level independently:

$$R^l(x, y) = \sum_{k=1}^K G^l\{\bar{W}^k(x, y)\} L^l\{I^k(x, y)\} \quad (6.25)$$

where l represents the number of the pyramid level.



where $\begin{cases} G(\bar{W}^k): \text{Gaussian of the normalized weights} \\ L(I^k): \text{Laplacian of the inputs} \end{cases}$

Fig. 6.8 Flow chart of the algorithm proposed by C. Ancuto. et al. [10].

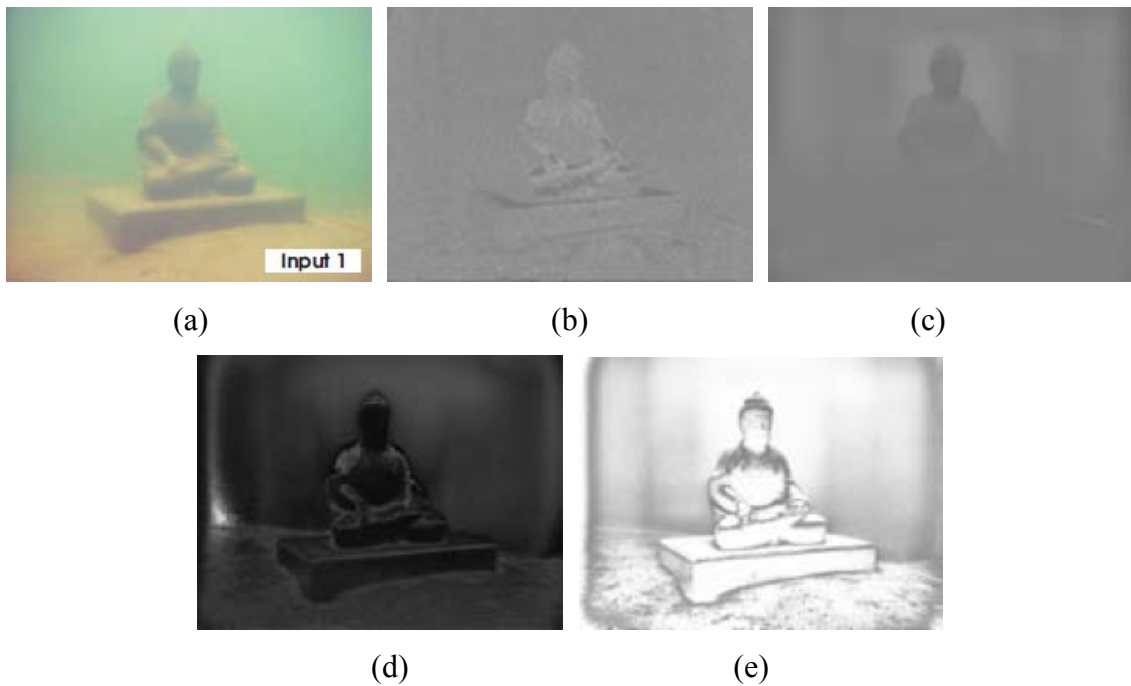
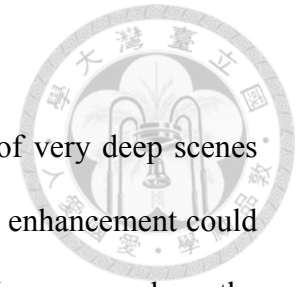


Fig. 6.9 The corresponding normalized weight maps: (a) Laplacian contrast. (b) Local contrast. (c) Saliency. (d) Exposedness.

6.4.2 Advantage and Disadvantage

Their approach shown limitations when dealing with images of very deep scenes taken with poor strobe and artificial light. In such cases, even some enhancement could be obtained, the bluish appearance however still remains. Moreover, when the illumination is poor the very distant parts of the scene cannot be recovered reliably. The restoration of distant objects and regions represents also a general limitation of their approach compared with hardware and polarization-based techniques that in general perform better in such cases due to the additional available information.





Chapter 7 Proposed method of Underwater Image Enhancement



7.1 Introduction

The existing underwater image enhancement methods usually have a trade-off between the computation time and the quality of enhanced results. Thus, we propose an underwater image enhanced method, which not only takes low computation time but also get a high-quality result. We use the contrast stretching in our proposed method to improve the contrast in an image and perform color correction to equalize the means of each color channel. The color of underwater image is rarely balanced correctly, and prominent blue or green color can be suppressed by this step without taking into account absorption phenomena. In order to overwrite the limitations of the underwater medium, we define that two inputs represent the contrast stretched and CLAHE version of the color corrected underwater image. To further enhance the robustness of the proposed underwater enhancement method, we integrate the post-processing mechanism in our system for some underwater images with non-uniform distribution.



7.2 Proposed Method

The flow chart of the proposed enhancing technique in underwater is shown in Fig.

7.1.

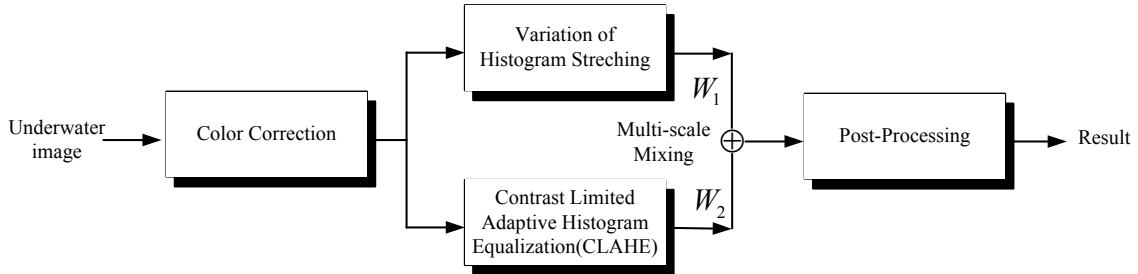


Fig. 7.1 Flow chart of the proposed enhancing technique in underwater.

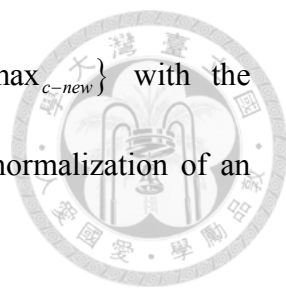
7.2.1 Contrast Stretching and Color Correction

Underwater images present a challenge, when we correct the blue-green monochrome look for bringing out our recognition of marine lives' color. Due to the nature of underwater optics, red light diminishes when the depth increases, thus producing blue to grey like images. For every 10m increase in depth, the brightness of sunlight will drop by half. Almost all red light is gone by 50% from the surface but blue light travels the longest in the water due to its shortest wavelength. That is why most underwater images are dominated by blue-green coloration. Since many above factors are constantly changing, we cannot know the entire effects of water. Thus, we proposed an efficient method to deal with the color shift. There are two steps we designed to solve this problem.

Step 1: Contrast Stretching

Normalization transforms an underwater image in each color channel

$$I_c : \{X_c \subseteq \mathbb{R}^n\} \rightarrow \{\min_c, \dots, \max_c\} \quad \text{with the values of intensity in the range (min, max)}$$



into a new enhanced image $I_{c-new} : \{X_c \subseteq \mathbb{R}^n\} \rightarrow \{\min_{c-new}, \dots, \max_{c-new}\}$ with the values of intensity in the range $(\min_{c-new}, \max_{c-new})$. The linear normalization of an image is performed according to the formula

$$I_{c-new} = (I_c - \min_c) \cdot \frac{\max_{c-new} - \min_{c-new}}{\max - \min} + \min_{c-new} \quad (7.1)$$

The histogram stretching can be used to shift the pixel values to fill the entire brightness range, resulting in high contrast as illustrated in Fig 7.2.

Step 2: Modify the mean value on each color channel

We adjust the mean value on each color channel in I_{c-new} to make they have the same value, and it will make the underwater image look natural. Fig. 7.3 shows the results of traditional enhancing technologies for underwater images.

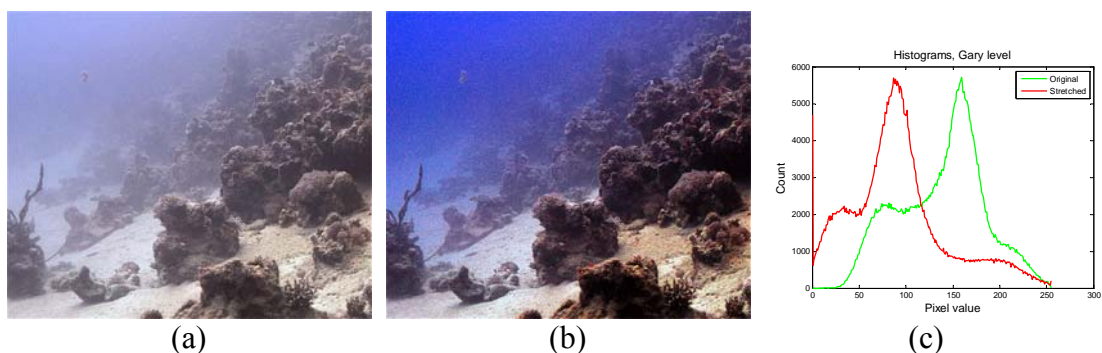


Fig. 7.2 The histogram of contrast stretching. (a) Original underwater image, (b) Result after saturation and intensity stretching on *HSI* colour model, (c) Histogram of original underwater image in gray level and Stretched one in gray level.

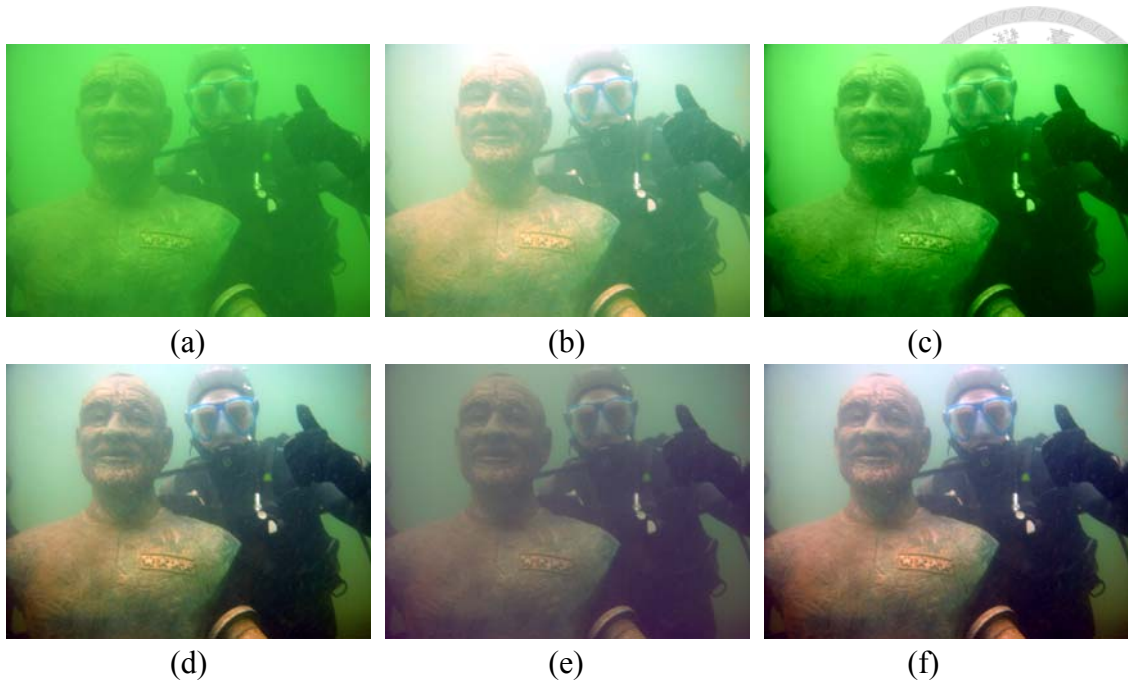


Fig. 7.3 Result of traditional enhancing technologies for underwater images and the color correction process of underwater images by using the proposed method. (a) Original underwater image, (b) White balance image, (c) CLAHE image, (d) Result after contrast stretching (only step 1), (e) Result after modifying the mean value (only step 2), and (f) Our method with color correction (process step1 and step2).

7.2.2 Variation on Histogram Stretching

The *RGB* color space is the de-facto standard for images. However, the best processing are not always be get, especially during the period of the image intended for human viewing. A color space will better represent the human visual system, like $L^*a^*b^*$ or $L'u'v'$ which can provide more natural stretching in some cases. In both of these color spaces, the L channel represents the brightness, while the (a^*, b^*) or (u', v') channels represent the color.

We compare the histogram stretching within a $L^*a^*b^*$ color space and in an *RGB* color space. We can find that the colors are slightly changed by the *RGB* stretching, and the *RGB* stretching also emphasizes reds and blues in the two cases as shown in Fig 7.4.

The colors remain the same because of the adjustment of the L channel, but the brightness is re-mapped. This adjusts the contrast in a way that sometimes can be more visually pleasing without significantly affecting the color balance. In addition, for the purposes of ensuring full color saturation and gaining fill contrast, stretching on HSV is also sometimes done after stretching in the RGB color space. In our experiment, we performs light stretching on $L^*a^*b^*$ color space.

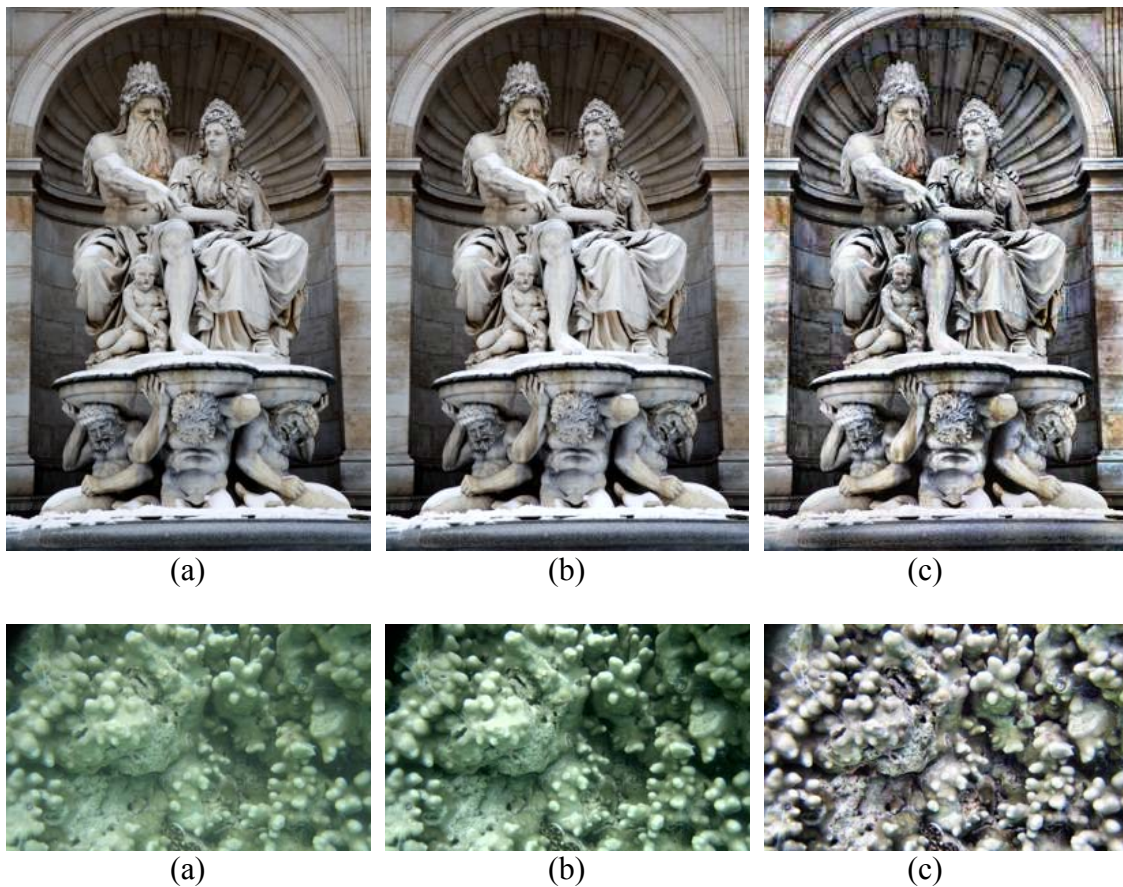


Fig. 7.4 Compare the histogram stretching within a $L^*a^*b^*$ color space and in an RGB color space. (a) Original image. (b) Stretching within a $L^*a^*b^*$ color space. (c) stretching in RGB color space.



7.2.3 Multiscale Mixing Process

The final restored image $R(x, y)$ is obtained by mixing the defined inputs with the weight at every pixel location (x, y) as

$$R(x, y) = \sum_{k=1}^K W^k \cdot J^k(x, y) \quad (7.2)$$

where k is the index of the inputs ($K=2$ in our case). $J^1(x, y)$ and $J^2(x, y)$ is the enhanced result after histogram stretching and contrasted limited adaptive histogram equalization, respectively. The weight W balances the effects of two images and is set as 0.5. Fig 7.5 illustrated that the characteristics of the final restored images are reducing noise level, better exposedness of the dark regions, improved global contrast, and the significant-enhanced details and edges.

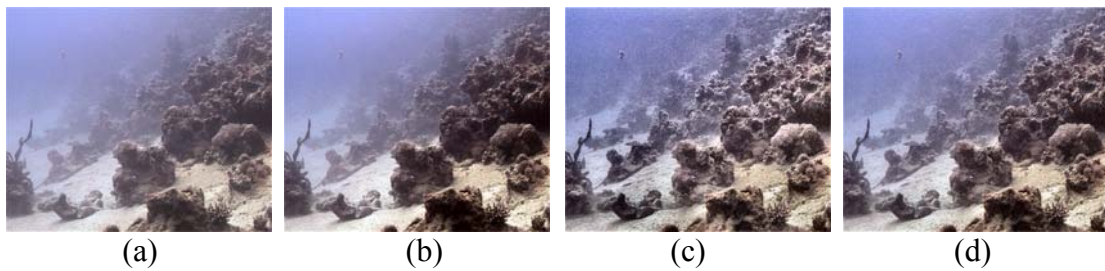


Fig. 7.5 The results of multiscale mixing process. (a) Input underwater image. (b) The enhanced result after contrast stretching. (c) The enhanced result after CLAHE. (d) The final restored image.

7.2.4 Post-Processing

To further enhance the robustness for the proposed underwater enhancement method, we integrate the post-processing mechanism in our system for some underwater images with non-uniform distribution. Thus, the fast haze removal [75] is based on [3], [13] is applied to perform the post-processing. The method is defined as below:

Step 1: Find the dark channel J^{dark} of the haze (underwater) image $J^c(x)$

$$J^{dark} = \min_{c \in \{r, g, b\}} (J^c(x)) \quad (7.3)$$

Step 2: Get the refined dark channel by mean filter

$$J^{ave-dark} = \text{average}_{\Omega(x)}(J^{dark}(x)) \quad (7.4)$$

Step 3: Estimate the airlight A and the atmospheric light $A_r(x) = A \cdot (1 - t(x))$

$$A = \frac{1}{2} \left(\max_{c \in \{r, g, b\}} (J^c(x)) + \max(J^{ave-dark}(x)) \right) [1 \ 1 \ 1]^T \quad (7.5)$$

or

$$A_r(x) = \min(\min(\rho j^{ave}, 0.9) J^{ave-dark}(x), J^{ave-dark}(x)) \quad (7.6)$$

where ρ is a parameter and $0 \leq \rho \leq 1/j^{ave}$, j^{ave} is the mean value of all elements in $J^{dark}(x)$.

Step 4: Output haze-free image

$$I(x) = \frac{J(x) - A_r(x)}{1 - \frac{A_r(x)}{A}} \quad (7.7)$$

The method [75] suits for handling the case that the illumination is poor in the very distant parts of the scene. Fig. 7.6(c) shows that the final enhancing images are transformed from the input underwater images (Fig. 7.6(a)) by applying the post-processing. To quantitatively evaluate our proposed method, we use the blind contrast enhancement assessment metric proposed by Tarel *et al* [13]. Three indicators e , r and σ are computed in the evaluation for comparing the input hazy image and the processed image, where e represents the rate of edges newly visible after enhancement, r estimates the average visibility enhancement obtained by the enhancement algorithm,

and σ is the percentage of pixels that becomes completely black or completely white after dehazing. Generally speaking, there should be higher values of e and r and lower value of σ in a better dehazed image. Table 7.1 shows the quantitative performance for Fig. 7.6. It is observed from e , and there are more visible edges in our result after post-processing. In addition, our method is able to achieve the smaller percentage of pixels which become completely black or completely white.

	Fusion-based [10]			Ours			Ours with post-processing		
	e	σ (%)	r	e	σ (%)	r	e	σ (%)	r
PICT0403	247.6	0.007	4.83	325.8	0	6.27	417.7	0.030	8.17
PICT0422	7.504	0.091	5.39	7.181	0.001	6.33	10.169	0.024	7.72

Table 7.1 Qualitative Comparison of the two images (PICT0403 and PICT0422) show in Fig. 7.6. Based on the indicators of Hautiere et al. [13]

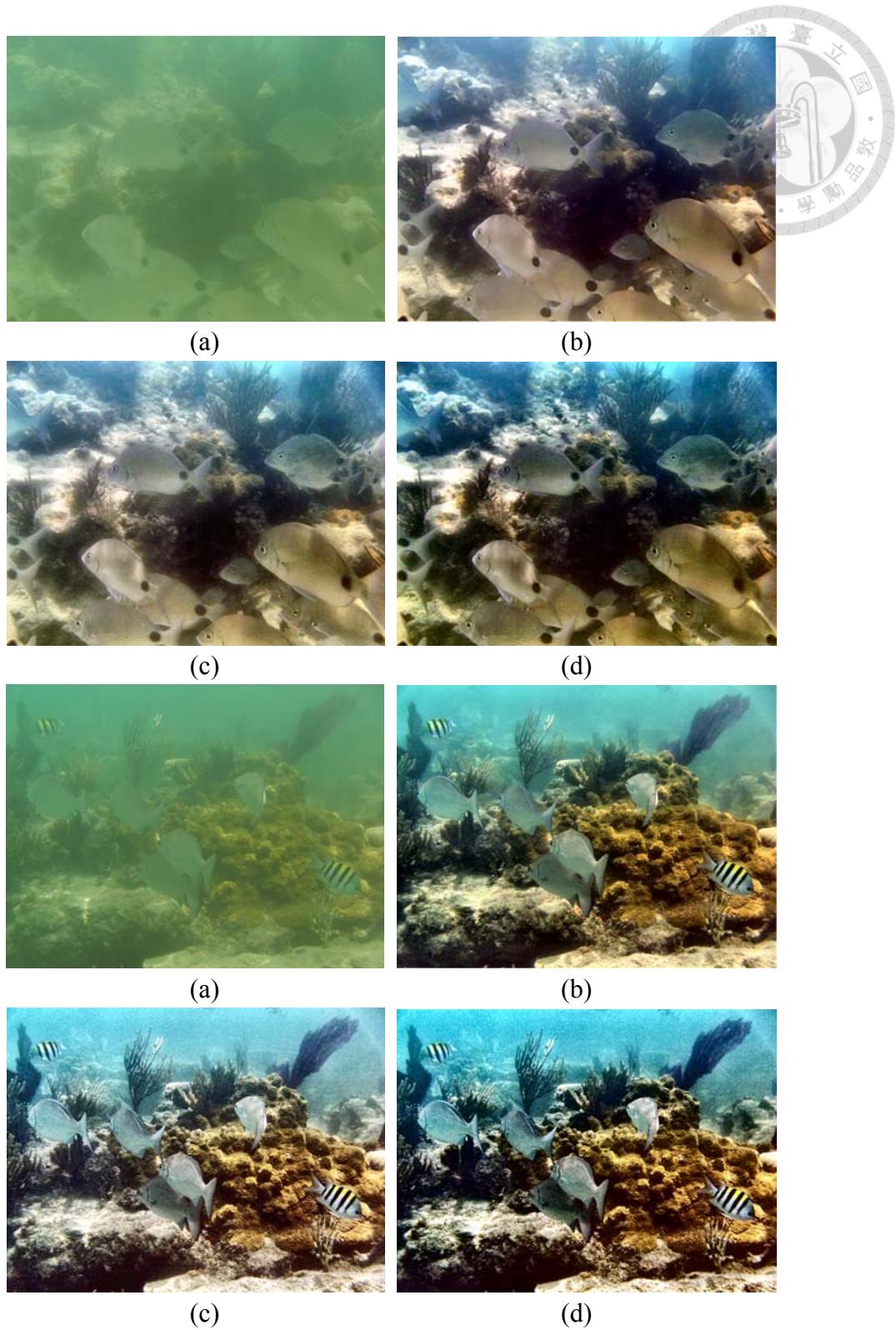


Fig. 7.6 Insufficient brightness and non-uniform distributed haze. (a) Input underwater image. (b) Fusion-based [10]. (c) Final enhancing image. (d) Final enhancing image by post-processing.

7.3 Experimental Results

For comparing the experimental results, the source of the underwater images are from [9], [10] and other underwater images. In Fig. 7.7, we compare our technique with several specialized underwater enhancing techniques [9-10]. In order to visualize how contrast is modified we employed the IQM metric [76] that was originally developed to evaluate tone mapping operators. This metric utilizes a model of the human visual system being sensitive to three types of structural changes: loss of visible contrast (green), amplification of invisible contrast (blue) and reversal of visible contrast (red). As a general remark, compared with the other considered approaches, the most predominant structural change characteristic to our method is the amplification of the contrast (blue) and only very few locations exhibit reverse (red) and loss (green) of the contrast.

Fig. 7.8 is extracted from an underwater video on the Youtube website filmed by the Bubble Vision Company [77]. This AVI-formatted video is 350 s long with a resolution of 720p. Fig. 7.8(b) shows that the image remains the haze effect and color change, after the process of histogram equalization [8]. Compare with Chao et al.'s method [78] as shown in Fig. 7.8(c), although the contrast of the image is increased, the color change appears even more prominent as the attenuated energy is not compensated individually based on different wavelength. Compare with Chiang.et al.'s method [9] as shown in Fig. 7.8(d), our proposed method can acquire color balanced, clearer and brighter enhanced images and preserve the fine transitions in the dark regions. We give the image the original color and clarity that it would have had if it were not taken underwater.

In Fig. 7.9, after we compare our proposed method with the fusion based of C.

Ancuto. et al. [10], there are a more pleasing image version and the sharper detail produced by our method. The difference how colors are restored between the two results can be also observed, especially in the distant regions. By the method of C. Ancuto. et al. [10], the Bluish-green appearance still remains. Moreover, when the illumination is poor, the very distant parts of the scene cannot be recovered effectively.

Fig. 7.10 shows the underwater image captured in different depth and the enhanced result. More results can be found:

https://sites.google.com/site/yutaitaisaithesis/underwater_enhancement

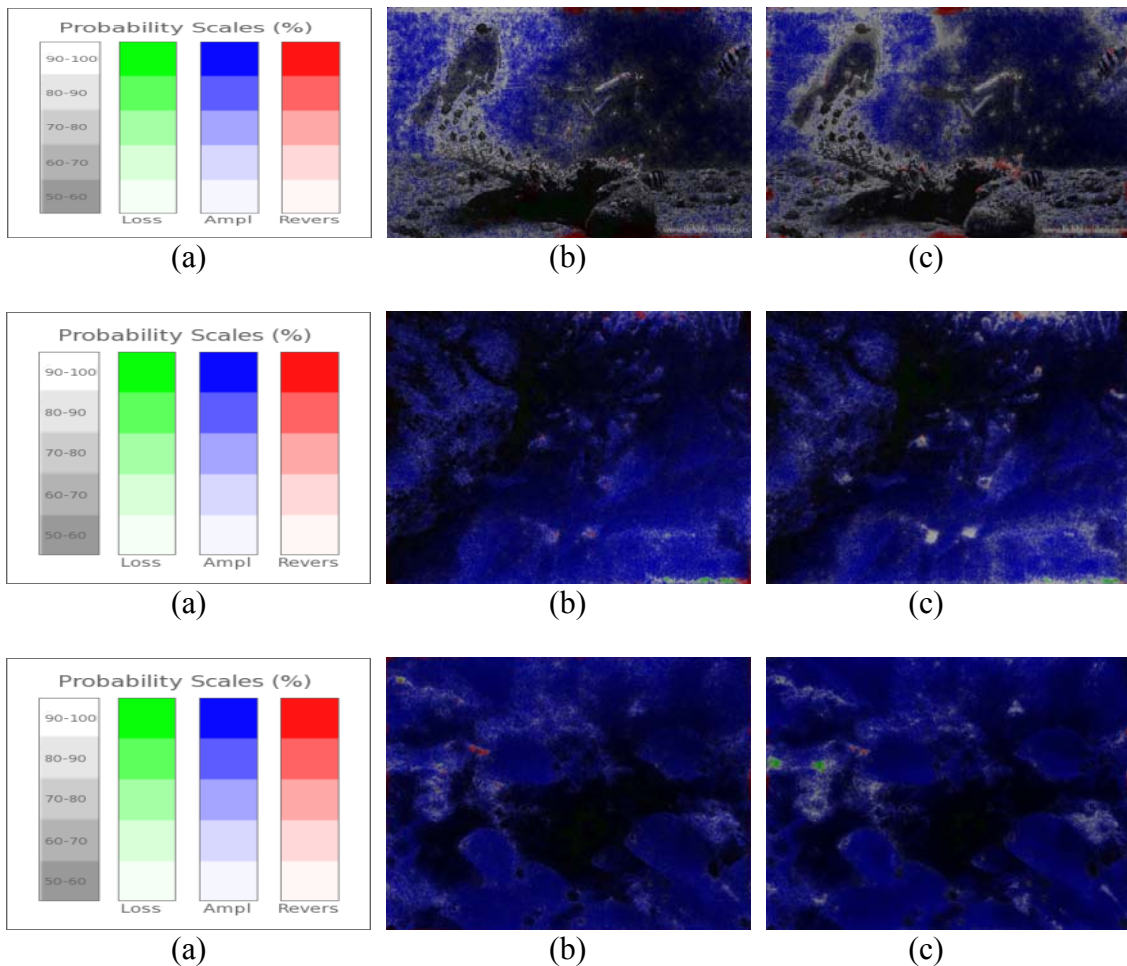


Fig. 7.7 Comparison of underwater enhanced results: (a) Image quality metric. (b) Chiang. et al.'s results [9] (top row) and C. Ancuto. et al.'s results [10] extracted from Fig 7.8 and Fig 7.9 when applied IQM metric [76]. (c) Our results.

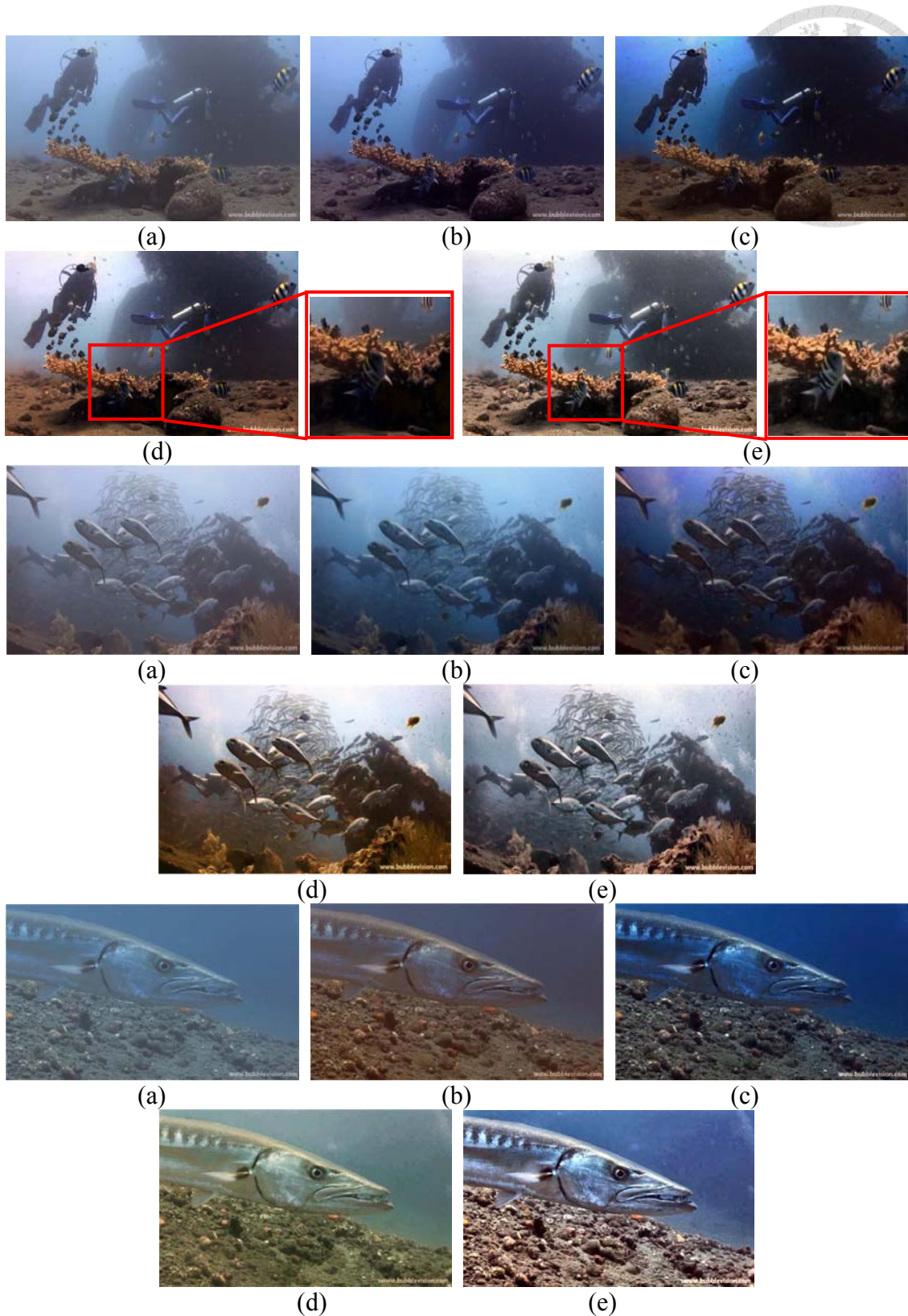


Fig. 7.8 Comparison of underwater enhanced results: (a) Input underwater images, (b) Histogram equalization, (c) Chao. et al.'s method [77], (d) Chiang. et al.'s method [9], and (e) Our proposed method.



(a)



(b)



(c)



(a)



(b)



(c)



(a)



(b)



(c)



(a)



(b)



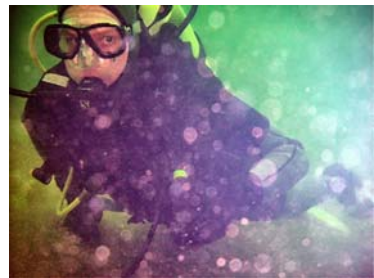
(c)



(a)



(b)



(c)

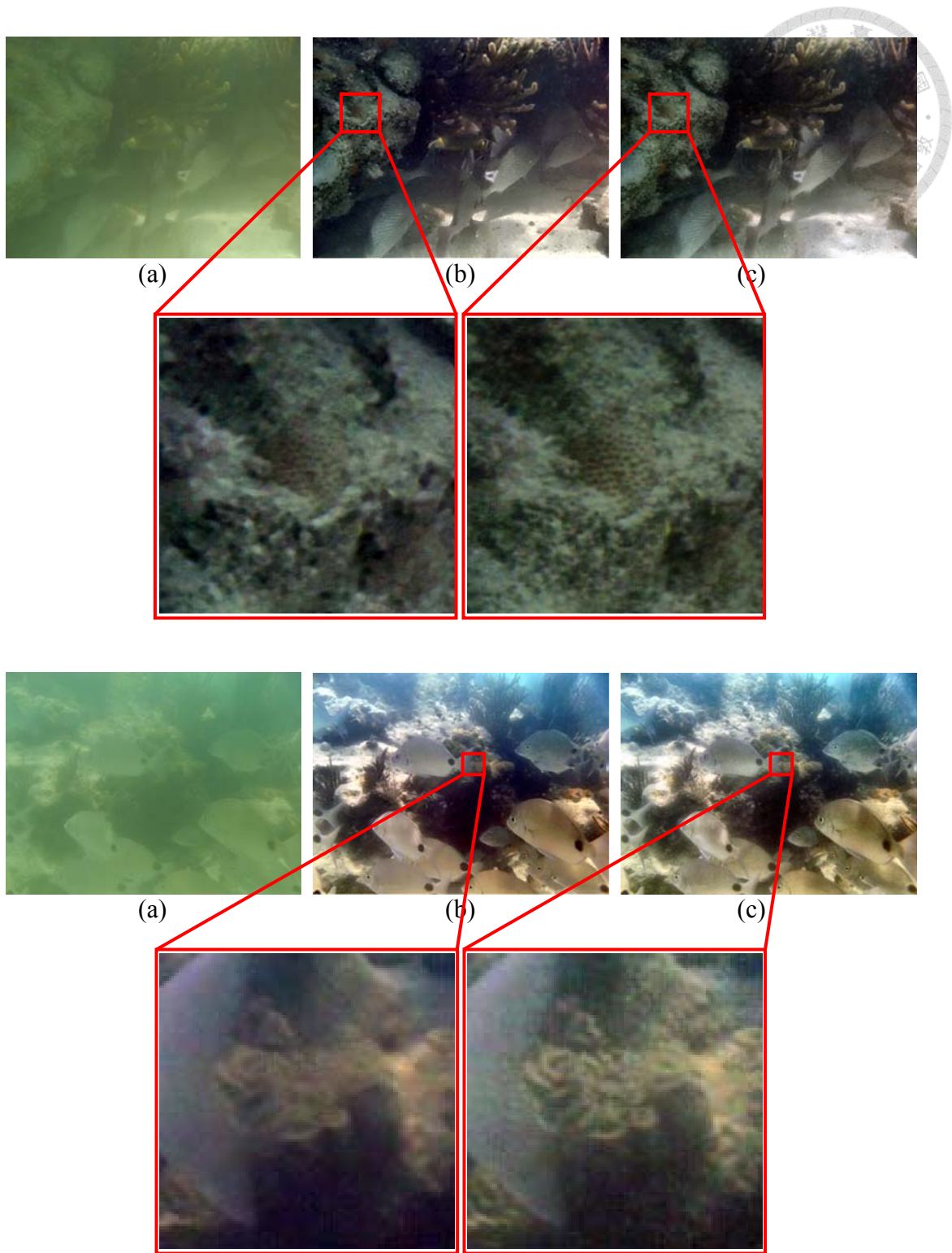


Fig. 7.9 Comparison of underwater enhanced results: (a) Input underwater images. (b) C. Ancuto. et al.'s results [10]. (c) Our results.



(a)



(b)



(a)



(b)



(a)



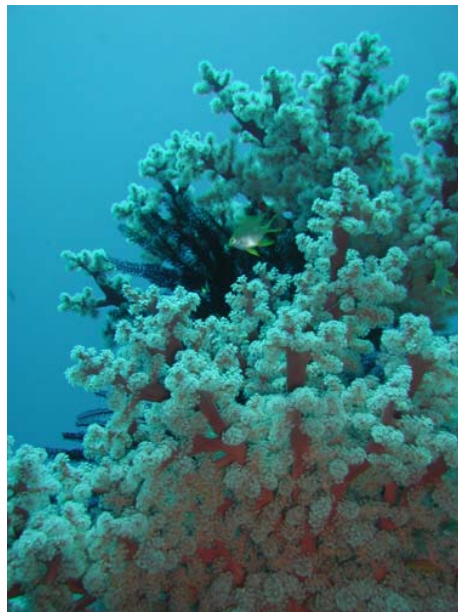
(b)



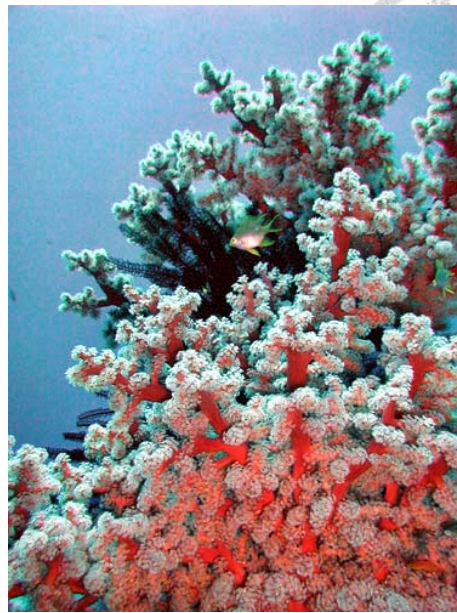
(a)



(b)



(a)



(b)



(a)



(b)



(a)



(b)

Fig. 7.10 Underwater enhanced results: (a) Input underwater images. (b) Our final enhanced results.

7.4 Conclusions

An attractive underwater enhancement method with high quality is proposed in this Chapter. First of all, it perform the color correction. Secondly, it performs light stretching on $l\alpha\beta$ color space and CLAHE on $l\alpha\beta$ color space. The advantage of applying two models is that it helps to equalize the colour contrast in the images and also addresses the problem of lighting. Finally, we perform the multiscale mixing process. To further enhance the robustness of the proposed underwater enhancement method, we integrate the post-processing mechanism in our system for some underwater images with non-uniform distribution. The extensive experiments demonstrate the utility of our solution since the visibility range of the underwater images and images captured from turbid waters are significantly increased by improving the scene contrast, the color appearance, and the visual detail.



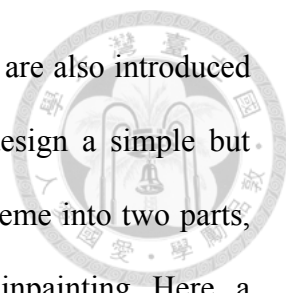


Chapter 8 Conclusion and Future Work



Most outdoor vision systems such as surveillance, tracking, object recognition, remote-sensing, and autonomous vehicles require images with clear visibility for robust features detection. Without clear visibility (for example: bad weather and underwater), these systems need more reliability and stability to maintain the detection quality. Despite their advantages, the performances of existing detection systems are limited in underwater environment and bad weather conditions like haze, rain, and snow. Note that the disturbance weather and environment effects removal is a difficult and challenging problem. The key points of the difficulty are illustrated as follows. First, images are degraded exponentially with the distance between the objective and observer. Second, recovering the scene structure from a single image is an ill-posed problem. Third, the contrast and color fidelity of images are drastically degraded due to atmospheric and water particles. To make outdoor and underwater vision systems more flexible in all environmental conditions, the new image and video processing algorithms are proposed to eliminate or reduce the effect of haze, rain, snow, underwater with high image quality and color naturalness.

In this thesis, we investigate the dehazing, rain removing, snow removing, and underwater enhancing processing in harsh environment. First, we introduce the physical properties and visual effects and then reference the three existing typical single image dehazing methods: contrast-based [1], independent component analysis [2], and dark channel prior-based analysis [3]. A robust, flexible, and effective dehazing method is proposed during daytime and nighttime to further improve the dehazing quality. For presentation completeness, three existing typical rain and snow removal methods in single image, including guidance image based [4], image decomposition analysis [5],



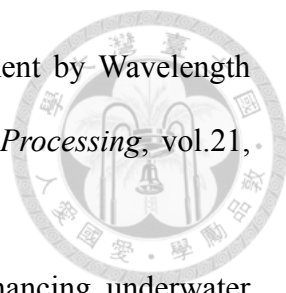
adaptive nonlocal means filter [6], and frequency-based analysis [7] are also introduced in the literature. For rain and snow removing investigation, we design a simple but effective removal method by dividing the rain or snow removal scheme into two parts, the first part is detection of rain or snow and the second part is inpainting. Here, a proper threshold is important. Furthermore, we extend the column into both side columns to produce a block-matrix for rain removal so that it may get more benefits for single image consideration when streak or flake is not obvious. The fuzzy random impulse reduction method is also used for noise removal. Specifically, to obtain vision quality of a resulting image, color transfer is utilized to protect the final snow-free image's color from high dynamic. These steps may be used in many applications for outdoor vision systems. Besides, it shows the worthy and important referencing for image and video processing categories by these steps. Three existing typical underwater enhanced methods: histogram-based equalization [8], wavelength-based compensation [9], and fusion based [10] are also introduced in the literature. To further improve the underwater image and video qualities, we design a simple but effective underwater enhanced method by combining the color correction, contrast stretching, and histogram equalization.

In the future, real-time processing is necessary and mandatory for all system applications. For this sake, our algorithms must be modified with more effective, more adaptive, and less complexity for authentic real-time realization. The preliminary strategy is to combine with the cloud computing. In our opinion, the haze, rain, and snow removal and underwater enhancement techniques will be more practical by the real-time processing.


REFERENCE




- [1] R. Tan., “Visibility in Bad Weather from a Single Image,” in *IEEE Conference on Computer Vision and Pattern Recognition*, June 2008, pp. 1–8.
- [2] R. Fattal, “Single Image Dehazing,” *ACM Transactions on Graphics*, vol. 27, pp. 72:1-72:9, August 2008.
- [3] K. He, J. Sun, and X. Tang, “Single Image Haze Removal Using Dark Channel Prior,” in *IEEE Conference on Computer Vision and Pattern Recognition*, 2009, pp. 1956-1963.
- [4] J. Xu, W. Zhao, P. Liu, and X. Tang, “An Improved Guidance Image Based Method to Remove Rain and Snow in a Single Image,” *CCSE Computer and Information Science Journal* 5(3), 2012, pp. 49-55.
- [5] L.-W. Kang, C.-W. Lin, and Y.-H. Fu, “Automatic single-frame-based rain streak removal via image decomposition,” *IEEE Trans. Image Processing*, vol. 21, no. 4, pp. 1742-1755, Apr. 2012.
- [6] J.-H. Kim, C. Lee, J.-Y. Sim, and C.-S. Kim, “Single-image deraining using an adaptive nonlocal means filter,” *2013 20th IEEE International Conference on Image Processing (ICIP)*, vol., no., pp.914-917, 15-18 Sept. 2013.
- [7] P. Barnum, T. Kanade, and S. Narasimhan, “Spatio-Temporal Frequency Analysis for Removing Rain and Snow from Videos,” in *Conjunction with International Conference on Computer Vision*, 2007, pp. 1-8.
- [8] K. Iqbal, R. Abdul Salam, A. Osman, and A. Zawawi Talib, “Underwater image enhancement using an integrated color model,” *Int. J. Comput. Sci.*, vol. 34, no. 2, pp. 2–12, 2007.


- 
- [9] J.-Y. Chiang and Y.-C. Chen, “Underwater Image Enhancement by Wavelength Compensation and Dehazing,” *IEEE Transactions on Image Processing*, vol.21, no.4, pp.1756-1769, April 2012.
- [10] C. Ancuti, C.O. Ancuti, T. Haber, and P. Bekaert, P., “Enhancing underwater images and videos by fusion,” *Computer Vision and Pattern Recognition (CVPR), 2012 IEEE Conference on* , vol., no., pp.81,88, 16-21 June 2012.
- [11] S. G. Narasimhan and S. K. Nayar, “Vision and the atmosphere,” *International Journal of Computer Vision*, vol. 48, pp. 233-254, July-August 2002.
- [12] L. Kratz, and K. Nishino, “Factorizing scene albedo and depth from a single foggy image,” *IEEE Twelfth International Conference on Computer Vision ICCV’09*, pp. 1701-1708.
- [13] J. P. Tarel and N. Hautière, “Fast visibility restoration from a single color or gray level image,” *IEEE International Conference on Computer Vision (ICCV’09)*, pp. 2201–2208. Kyoto, Japan 2009.
- [14] N. Carlevaris-Bianco, A. Mohan, and R. M. Eustice, “Initial results in underwater single image dehazing,” in *Proc. IEEE OCEANS*, 2010, pp. 1–8.
- [15] Y. Y. Schechner, S. G. Narasimhan, and S. K. Nayar, “Instant Dehazing of Images Using Polarization,” in *IEEE Computer Society Conference on Computer Vision and Pattern Recognition* , 2001, pp. 1:325–332.
- [16] S. Shwartz, E. Namer, and Y. Schechner, “ Blind haze separation,” in *IEEE Computer Society Conference on Computer Vision and Pattern Recognition*, 2006, pp. 1984 - 1991.
- [17] F. Cozman and E. Krotkov, “Depth from scattering,” in *IEEE Computer Society Conference on Computer Vision and Pattern Recognition*, 1997, pp. 801–806.
- [18] S. K. Nayar and S. G. Narasimhan, “Vision in bad weather,” in *IEEE International*

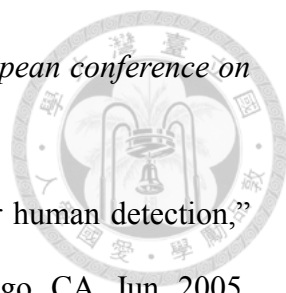
Conference on Computer Vision, 1999, pp. 820–827.

- 
- [19] S. G. Narasimhan and S. K. Nayar, “Contrast restoration of weather degraded images,” *IEEE Transactions on Pattern Analysis and Machine Intelligence*, vol. 25, pp. 713 - 724, June 2003.
- [20] N. Hautiere, J. -P Tarel, and D. Aubert, “Towards Fog-Free In-Vehicle Vision Systems through Contrast Restoration,” *Computer Vision and Pattern Recognition, 2007. CVPR '07. IEEE Conference on*, vol., no., pp.1,8, 17-22 June 2007.
- [21] S. Narasimhan and S. Nayar, “Interactive deweathering of an image using physical models,” in *IEEE Workshop on Color and Photometric Method in Computer Vision*, 2003, pp. 1- 8.
- [22] J. Kopf, B. Neubert, B. Chen, M. Cohen, D. Cohen-Or, O. Deussen, M. Uyttendaele, and D. Lischinski, “Deep photo: Model-based photograph enhancement and viewing,” *ACM Transactions on Graphics*, Vol. 27, pp. 116:1-116:10, December 2008.
- [23] N. Hautiere, J. Tarel, and D. Aubert, “Toward fog-free invehicle vision systems through contrast restoration,” in *IEEE Conference on Computer Vision and Pattern Recognition*, 2007, pp. 1- 8.
- [24] C. Ancuti, C. Hermans, and P. Bekaert, “A fast semi-inverse approach to detect and remove the haze from a single image,” in: *Proc. ACCV*, 2011, pp. 501 - 514.
- [25] J. Yu and Q. Liao, “Fast single image fog removal using edge-preserving smoothing,” in: *Proc. IEEE ICASSP*, 2011, pp. 1245–1248.
- [26] P. Carr and R. Hartley, “Improved single image dehazing using geometry,” in: *Proc. DICTA*, 2009, pp. 103–110.

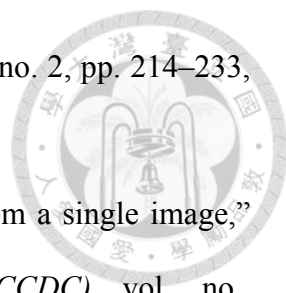
- 
- [27] L. Schaul, C. Fredembach, and S. Süsstrunk, “Color image dehazing using the nearinfrared,” *in: Proc. IEEE ICIP*, 2009, pp. 1629–1632.
- [28] X. Dong, X. Hu, S. Peng, and D. Wang, “Single color image dehazing using sparse priors,” *in: Proc. IEEE ICIP*, 2010, pp. 3593–3596.
- [29] A. Levin, D. Lischinski, and Y. Weiss, “A closed form solution to natural image matting,” *in IEEE Computer Society Conference on Computer Vision and Pattern Recognition*, 2006, pp. 61 - 68.
- [30] W B. Thompson, P. Shirley, and J A. Ferwerda, “A spatial post-processing algorithm for images of night scenes,” *Journal of Graphics Tools*, vol. 7, pp. 1-11, November 2002.
- [31] K. Gibson, T. Nguyen, “On the Effectiveness of the Dark Channel Prior for Single Image Dehazing by Approximating with Minimum Volume Ellipsoids,” *in IEEE International Conference on Acoustics, Speech and Signal Processing*, 2011, pp. 1253-1256.
- [32] S.-C. Pei, T.-Y. Lee, “Nighttime haze removal using color transfer pre-processing and Dark Channel Prior,” *Image Processing (ICIP), 2012 19th IEEE International Conference on* , vol., no., pp.957,960, Sept. 30 2012-Oct. 3 2012.
- [33] E. Reinhard, M. Adhikhmin, B. Gooch, and P. Shirley, “Color Transfer between Images,” *IEEE Trans. on Computer Graphics and Applications*, vol.21, pp. 34–41, Sep/Oct 2001.
- [34] R. Schettini, F. Gasparini, S. Corchs and F. Marini, “Contrast image correction method,” *Journal of Electronic Imaging*, vol.19, no. 2, pp. 023005-1 – 023005-11, April 2010.
- [35] B. Stoppee and Stoppees, *Guide to Photography and Light*, Mar. 2010.
- [36] D. J. Jobson, Z. Rahman, and G. A. Woodell, “A multiscale retinex for bridging

- the gap between color images and the human observation of scenes,,” *IEEE Transactions on Image Processing*, vol. 6, no. 7, pp. 965 –976, July 1997.
- [37] Gaurav Sharma, *Digital Color Imaging Handbook*, CRC Press, 2003.
- [38] C. Tomasi and R. Manduchi, “Bilateral filtering for gray and color images,” *Computer Vision, 1998. Sixth International Conference on*, vol., no., pp.839,846, 4-7 Jan 1998.
- [39] S.-C. Pei, T.-Y. Lee, “Effective image haze removal using dark channel prior and post-processing,” *Circuits and Systems (ISCAS), 2012 IEEE International Symposium on*, vol., no., pp.2777,2780, 20-23 May 2012.
- [40] R. He, Z. Wang, Y. Fan, D.D. Feng, “Multiple scattering model based single image dehazing,” *Industrial Electronics and Applications (ICIEA), 2013 8th IEEE Conference on*, vol., no., pp.733,737, 19-21 June 2013
- [41] C.O. Ancuti and C. Ancuti, “Single Image Dehazing by Multi-Scale Fusion,” *Image Processing, IEEE Transactions on*, vol.22, no.8, pp.3271,3282, Aug. 2013.
- [42] B. Li, S. Wang, and Y. Geng, “Image enhancement based on Retinex and lightness decomposition,” in *IEEE International Conference on Image Processing*, 2011, pp. 3417–3420.
- [43] X. Dong, G. Wang, Y. Pang, W. Li, J. Wen, W. Meng, and Y. Lu, “Fast efficient algorithm for enhancement of low lighting video,” in *Proceedings of International Conference on Multimedia and Expo. IEEE*, 2011, pp. 1–6.
- [44] J.-H. Kim, W.-D. Jang, J.-Y. Sim, and C.-S. Kim, “Optimized contrast enhancement for real-time image and video dehazing,” *Journal of Visual Communication and Image Representation*, Volume 24, Issue 3, April 2013, Pages 410-425.

- 
- [45] K. Nishino, L. Kratz, and S. Lombardi, “Bayesian Defogging,” *Int. J. Comput. Vision* 98, 3 (July 2012), 263-278.
- [46] J. Zhang, L. Li, G. Yang, Y. Nishino, and J. Sun, “Local albedo-insensitive single image dehazing,” *Vis. Comput.*, 2010, 26, (6– 8), pp. 761–768.
- [47] K. Garg, and S. Nayar, “Detection and Removal of Rain from Videos,” in *IEEE Computer Society Conference on Computer Vision and Pattern Recognition*, 2004, pp. I-528 - I-535.
- [48] K. Garg, and S. Nayar, “When does a camera see rain?,” *Computer Vision, 2005. ICCV 2005. Tenth IEEE International Conference on* , vol.2, no., pp.1067,1074 Vol. 2, 17-21 Oct. 2005.
- [49] K. Garg and S. K. Nayar, “Vision and rain,” *Int. J. Comput. Vis.*, vol. 75, no. 1, pp. 3–27, Oct. 2007.
- [50] X. Zhang, H. Li, Y. Qi, W. K. Leow, and T. K. Ng, “Rain Removal in Video by Combining Temporal and Chromatic Properties,” in *IEEE International Conference on Multimedia and Expo*, 2006, pp. 461 - 464.
- [51] J. Bossu, N. Hautière, and J. P. Tarel, “Rain or snow detection in image sequences through use of a histogram of orientation of streaks,” *Int. J. Comput. Vis.*, vol. 93, no. 3, pp. 348–367, July 2011.
- [52] H. Hase, K. Miyake, and M. Yoneda, “Real-time snowfall noise elimination,” in *IEEE International Conference on Image Processing*, 1999, pp. 406 - 409.
- [53] S. Starik and M. Werman, “Simulation of rain in videos,” in *Int’l. Workshop on Texture Analysis and Synthesis*, 2003.
- [54] J. Xu, W. Zhao, P. Liu, and X. Tang, “Removing rain and snow in a single image using guided filter,” *Computer Science and Automation Engineering (CSAE), 2012 IEEE International Conference on* , vol.2, no., pp.304,307, 25-27 May 2012.

- 
- [55] K. He, J. Sun and X. Tang, “Guided Image Filtering,” in *European conference on Computer vision*, 2010, pp. 1-14.
- [56] N. Dalal and B. Triggs, “Histograms of oriented gradients for human detection,” in *Proc. IEEE Conf. Comput. Vis. Pattern Recognit.*, San Diego, CA, Jun. 2005, vol. 1, pp. 886–893.
- [57] S. Mallat and Z. Zhang, “Matching pursuits with time-frequency dictionaries,” *IEEE Trans. Signal Process.*, vol. 41, no. 12, pp. 3397–3415, Dec. 1993.
- [58] H. Takeda, S. Farsiu, and P. Milanfar, “Kernel regression for image processing and reconstruction,” *IEEE Trans. Image Process.*, vol. 16, no. 2, pp. 349–366, Feb. 2007.
- [59] L. Vincent, “Morphological grayscale reconstruction in image analysis: Applications and efficient algorithms,” *IEEE Trans. Image Process.*, vol. 2, no. 2, pp. 176–201, 1993.
- [60] N. Otsu, “A threshold selection method from gray-level histograms,” *Automatica*, vol. 11, nos. 285–296, pp. 23–27, 1975.
- [61] D. Eigen, D. Krishnan, and R. Fergus, “Restoring an Image Taken through a Window Covered with Dirt or Rain,” *2013 IEEE International Conference on Computer Vision (ICCV)*, vol., no., pp.633,640, 1-8 Dec. 2013.
- [62] A. Cord and D. Aubert, “Towards rain detection through use of in-vehicle multipurpose cameras,” *2011 IEEE Intelligent Vehicles Symposium (IV)*, vol., no., pp.833,838, 5-9 June 2011.
- [63] A. Cord and N. Gimonet, “Detecting Unfocused Raindrops: In-Vehicle Multipurpose Cameras,” *IEEE Robotics & Automation Magazine*, vol.21, no.1, pp.49-56, March 2014.
- [64] S. You, R. T. Tan, R. Kawakami, and K. Ikeuchi, “Adherent Raindrop Detection

- and Removal in Video,” *2013 IEEE Conference on Computer Vision and Pattern Recognition (CVPR)*, vol., no., pp.1035,1042, 23-28 June 2013.
- [65] O. Le Meur, M. Ebdelli, and C. Guillemot, “Hierarchical Super-Resolution-Based Inpainting,” *IEEE Transactions on Image Processing*, vol.22, no.10, pp.3779-3790, Oct. 2013.
- [66] Z. Xu and J. Sun, “Image Inpainting by Patch Propagation Using Patch Sparsity,” *IEEE Transactions on Image Processing*, vol.19, no.5, pp.1153,1165, May 2010
- [67] S. Schulte, M. Nachtgael, V. D. Witte, D. V. der Weken and E. E. Kerre, “A fuzzy impulse noise detection and reduction method,” *IEEE Transactions on Image Processing*, vol. 15, pp. 1153-1162, 2006.
- [68] E. E. Kerre, *Fuzzy Sets and Approximate Reasoning*, Xian Jiaotong University Press, 1998.
- [69] P. Sand and S. Teller, “Particle video: long-range motion estimation using point trajectories,” *In CVPR*, 2006.
- [70] S.-C. Pei, Y.-T. Tsai and C.-Y. Lee, “Removing Rain and Snow in a Single Image Using Saturation and Visibility Features,” *2014 IEEE International Conference on Multimedia & Expo Workshop*, Chengdu, China, July 14-18, 2014.
- [71] Y. Schechner and Y. Averbuch, “Regularized image recovery in scattering media,” *IEEE Trans Pattern Anal Mach Intell.*, 2007.
- [72] Zuiderveld, Karel, “Contrast Limited Adaptive Histogram Equalization,” *Graphic Gems IV*. San Diego: Academic Press Professional, 1994. 474–485.
- [73] M. S. Hitam, W. N. J. H. W. Yussof, E. A. Awalludin, and achok, “Mixture contrast limited adaptive histogram equalization for underwater image enhancement,” *2013 International Conference on Computer Applications Technology (ICCAT)*, vol., no., pp.1-5, 20-22 Jan. 2013.

- 
- [74] S. Q. Duntley, "Light in the sea," *J. Opt. Soc. Amer.*, vol. 53, no. 2, pp. 214–233, 1963.
- [75] Q. Liu, M. Y. Chen, and D. H. Zhou, "Fast haze removal from a single image," *2013 25th Chinese Control and Decision Conference (CCDC)*, vol., no., pp.3780-3785, 25-27 May 2013.
- [76] T. O. Aydin, R. Mantiuk, K. Myszkowski, and H.-S. Seidel, "Dynamic range independent image quality assessment," *In SIGGRAPH*, 2008.
- [77] [Online]. Available: <http://www.youtube.com/user/bubblevision>.
- [78] L. Chao and M. Wang, "Removal of water scattering," *2010 2nd International Conference on Computer Engineering and Technology (ICCET)*, vol.2, no., pp.V2-35,V2-39, 16-18 April 2010.